

SOLID STATE SYNTHESIS OF NICKEL BORIDES AS CATALYSTS FOR HYDROGEN  
EVOLUTION

By

FABRIZIO GUZZETTA

A THESIS PRESENTED TO THE GRADUATE SCHOOL  
OF THE UNIVERSITY OF FLORIDA IN PARTIAL FULFILLMENT  
OF THE REQUIREMENTS FOR THE DEGREE OF  
MASTER IN SCIENCE

UNIVERSITY OF FLORIDA

2013

© 2013 Fabrizio Guzzetta

To my family, my friends, my wife

## ACKNOWLEDGMENTS

I want to thank my family for continuous support and inspiration, even and especially in the hardest moments. I want to thank my wife, Ana Cecilia for the understanding shown in these years that she had to wait with me here, under an F-2 visa to finish her career, and for continuous love and appreciation. I also thank my friends here in Gainesville and the ones I have in Italy for continuous friendship and help in the moments of solitude or just being homesick. I want to thank the University of Florida and the College of Liberal Arts and Sciences and the Department of Chemistry at UF for granting me the opportunity to carry on my Ph.D. and boosting my academic career. I want to thank Dr. Witcha Imaram from Dr. Angerhofer's group, my advisor, for all the help and fruitful advice and improving my skills, and all the committee members for always being available with useful and helpful advice. Along with them I want to thank the undergraduate students Amer A. Belal and Nick Paganella for the precious friendship and wonderful experimental work. Their support, in achieving the goals that this project required, was immensely precious and for that I am really grateful. I want to thank my cooperators, in primis Dr. Riccarda Caputo at the ETH for all the numerous calculations, Dr. Sebastiano Garroni for the nuclear magnetic resonance and magic angle spinning studies, Dr. Antonio Masello, and Prof. George Christou for the access to the Fourier transform – infra red instrument and – at large – the Department of Chemistry at the University of Florida, for all of them being helpful with my experiments. I want to thank Dr. Juan Nino and Dr. Jacob Jones and their groups for the availability in offering me their instrumentation to better understand the system under study and their efforts, and precious advice to get better data in a field that was not properly in their research interests.

I want to thank Dr. Craciun, Dr. Acree, and Dr. Lambers, at the Major Analytical Instrumentation Center at the University of Florida, for access and use of the powder X-ray diffraction instrument, for the scanning electron microscopy and XPS measurements on the systems under study. I want to thank all of the people who helped me, in becoming a better scientist during this multiple-year endeavor that I forgot to mention above, but, nonetheless, have a special place in my heart.

## TABLE OF CONTENTS

	<u>page</u>
ACKNOWLEDGMENTS.....	4
LIST OF TABLES.....	8
LIST OF FIGURES.....	9
LIST OF ABBREVIATIONS.....	13
ABSTRACT.....	15
CHAPTER	
1 TRANSITION METAL BORIDES AS HYDROGENATION CATALYSTS.....	17
1.1 Introduction.....	17
1.1.1 Compressed Hydrogen.....	18
1.1.2 Liquid Hydrogen.....	20
1.1.3 Solid Hydrogen storage.....	21
1.1.4 Hydrolysis of Sodium Borohydride.....	25
1.2 History of TMB and their Classification.....	29
1.3 Metal Borides as Hydrogenation Catalysts.....	32
2 SYNTHESIS AND CHARACTERIZATION OF NiB <sub>x</sub> .....	39
2.1 Synthesis of NiB <sub>x</sub> .....	39
2.2 Theoretical calculations.....	43
2.3 Experimental Characterization.....	49
2.3.1 Density.....	49
2.3.2 Thermal Analysis.....	50
2.3.3 FTIR.....	56
2.3.4 Powder XRD.....	63
2.3.4.1 Powders as Synthesized (Under Normal Laboratory Conditions) ..	70
2.3.4.2 Annealing the Powders under Ar(g).....	70
2.3.4.3 $\gamma$ -Irradiation of the Powders.....	75
2.3.5 Quantitative Elemental Analysis: ICP-AES.....	76
2.3.5.1 Determination of the Nickel Amount in the Unknown.....	77
2.3.5.2 Determination of the Boron Amount in the Unknown.....	79
2.3.6 Quantitative Analysis: XRD Refinement.....	81
2.3.7 XPS.....	82
2.3.7.1 Determination of Nickel through XPS.....	85
2.3.7.2 Determination of Boron through XPS.....	86
2.3.8 Morphology of NiB <sub>x</sub> .....	88
2.3.8.1 TEM and EDXS.....	88
2.3.8.2 SEM Microscopy and EDS.....	91

2.4 Discussion of the Results.....	94
2.4.1 Thermal Analysis .....	94
2.4.2 FTIR .....	96
2.4.3 XRD .....	100
2.4.4 XPS.....	101
2.4.5 Quantitative Elemental Analysis.....	107
2.4.6 Morphology of NiB <sub>x</sub> .....	108
3 CATALYSIS OF NICKEL BORIDES .....	111
3.1 Experimental Results .....	111
3.2 Energetics of the Reactions .....	117
3.3 Identification of Reaction Products.....	124
3.4 Discussion of the Results.....	131
4 CONCLUSIONS AND FUTURE WORK .....	134
4.1 Conclusion and Remarks.....	134
4.2 Outlook .....	135
APPENDIX MAGNETIC TECHNIQUES.....	137
A.1 NMR.....	140
A.2 EPR.....	145
A.3 SQUID.....	147
LIST OF REFERENCES .....	150
BIOGRAPHICAL SKETCH.....	157

## LIST OF TABLES

<u>Table</u>	<u>page</u>
1-1 Comparison of the key properties of the main (condensed-phase) hydrogen storage materials.....	22
1-2 Hydrogen storage properties of selected high capacity hydrides .....	24
2-1 Atom site occupancies for the monoclinic and orthorhombic NiB <sub>3</sub> structures.....	44
2-2 Calculated Thermodynamic and Structural Data of the Compounds. ....	47
2-3 Calculated energies, zero point energies and entropic contributions of the o - NiB and the o – and m – NiB <sub>3</sub> .....	49
2-4 Calculated molecular weights, molar volumes and for different nickel borides...	50
2-5 Literature reported XPS B 1s and Ni 2p <sub>3/2</sub> line positions .....	103
3-1 %-yield of hydrogen evolution from catalyzed hydrolysis of sodium borohydride: NC stands for Non-Catalyzed, UP stands for Unsupported Powder and SC stands for Supported Powder (mediated reactions).....	113
3-2 Temperatures and constants for the three sets of reactions.....	119

## LIST OF FIGURES

<u>Figure</u>	<u>page</u>
1-1 Device for compressed hydrogen gas storage from Quantum Technologies. ....	19
1-2 Liquid H <sub>2</sub> (LH <sub>2</sub> ) tank system.....	20
1-3 Activated complexes in acidic hydrolysis of sodium borohydride.....	26
1-4 Log(k) versus pH plot for the hydrolysis of sodium borohydride. ....	27
1-5 Comparison of the catalytic activity of amorphous Ni <sub>2</sub> B and Raney nickel in the hydrogenation of acetonitrile.....	35
1-6 Hydrogen evolution kinetics as a function of the wt-% of sodium hydroxide.....	36
2-1 Schematic of the gas collection system.....	40
2-2 <i>Pnma</i> crystal structure of NiB <sub>3</sub> .....	45
2-3 <i>P2<sub>1</sub>/c</i> monoclinic crystal structure of NiB <sub>3</sub> .....	46
2-4 TGA/DSC graph of the 5 mol-% Nickel Bromide in NaBH <sub>4</sub> after hydrolysis 1) Water loss; 2) the broad peak position and 3) unexplained feature.....	53
2-5 SiO <sub>2</sub> gel thermogram: 1) water loss peak. 2) and 3) unassigned transformation(s). ....	54
2-6 NiB <sub>x</sub> :SiO <sub>2</sub> (1:10 wt) supported catalyst thermogram.....	55
2-7 Calculated FT-IR spectra of the most stable NiB <sub>3</sub> structures. In blue the orthorhombic <i>Pnma</i> structure, in black the <i>P2<sub>1</sub>/c</i> structure. ....	56
2-8 FT-IR spectra of the non-hydrolyzed powders.....	58
2-9 MgB <sub>2</sub> crystal structure. <sup>91,92</sup> Dashed lines show the cubic structure of Mg. ....	59
2-10 IR spectra of MgB <sub>2</sub> . ....	60
2-11 FTIR spectra : a) MgB <sub>2</sub> , b) the powder annealed 5 h at 500°C, c) the powder annealed 5 h at 830°C, d) KBr.....	61
2-12 FTIR in the mid IR of the commercial SiO <sub>2</sub> gel (in black) and the supported nickel boride (in red). ....	62
2-13 Schematic used in the derivation of Bragg's Law for X-ray diffraction.....	65
2-14 Miller planes and indexing in a simple unit cell.....	66

2-15	XRD pattern of the freshly prepared powders. Blue: Experimental pattern. Red: NaBr. Green: NaBH <sub>4</sub> . Grey:Residuals.....	71
2-16	XRD pattern obtained on the hydrolyzed powders. ....	71
2-17	Annealing patterns. Blue: Hydrolyzed powder not annealed (298 K).....	72
2-18	Blue: RTP hydrolyzed powder pattern. Green: Annealed for 1 h under Ar(g) at 1100 K. Red: Annealed for 5 h under Ar(g) at 1100. ....	73
2-19	XRD patterns obtained at the 11BM beamline of the APS in Argonne. ....	74
2-20	$\gamma$ -irradiated NiB <sub>x</sub> samples after 10 mins (blue), 1 h (red), 1 day (green) and 1 week (magenta). Patterns were collected at the APD 3720 (UF). ....	76
2-21	Correlation plots for the nickel standard observed at 231.604 nm, and at 232.138 nm.....	79
2-22	Correlation plots for the boron standard observed at 249.678 nm and at 249.772 nm.....	80
2-23	Quantitative results from the XRD refinement shown in figure 2-15. ....	82
2-24	Room temperature C 1s peak. The black line represents the as-determined peak, the red one is the peak as expected for the default C 1s position.....	84
2-25	Ni XPS spectra. ....	85
2-26	High resolution spectrum of commercial MgB <sub>2</sub> . ....	86
2-27	Comparison of the B 1s peaks.....	87
2-28	XPS HR spectra of the B 1s peak. Intensities ratio are 3:1 for oxidized boron. Al anode in black; Mg anode in red .....	88
2-29	From a) to d), respectively: a STEM image and increasingly resolved TEM images of the powders. ....	89
2-30	TEM images of a grain of material. a) and b) show images of the same grain of powder with the magnification doubled.....	90
2-31	EDXS of NiB <sub>x</sub> unsupported sample showing a boron peak which is more intense than the carbon peak. Nickel peaks are also clearly visible. ....	91
2-32	EDXS of the supported powders. The low energy peaks containing contributions from C and B are framed in red and zoomed in. ....	91
2-33	SEM images of the various powders. ....	93

2-34	EDS spectroscopy of SiO <sub>2</sub> supported NiB <sub>x</sub> .....	93
2-35	Literature reported DSC thermogram of Ni <sub>3</sub> B .....	95
2-36	IR spectra of NbB <sub>2</sub> and CaB <sub>6</sub> microcrystalline borides.. .....	97
2-37	Experimental IR from Molvinger et al.....	97
2-38	Mononuclear bidentate M-BH <sub>4</sub> complex. ....	98
2-39	FTIR spectra of SiO <sub>2</sub> supported NbB <sub>2</sub> at room temperature and after annealing under Ar for 12 h.. .....	99
2-40	XRD patterns of nickel borides .....	100
2-41	XPS spectra of Ni 2p <sub>3/2</sub> and B 1s for the nickel borides.....	102
2-42	Literature reported XPS spectra .....	104
2-43	Electron density difference of Ni <sub>2</sub> B, Ni <sub>3</sub> B, and NiB <sub>3</sub> .. .....	106
2-44	SEM image and relative EDXS for MgB <sub>2</sub> .....	109
2-45	Literature reported EDXS spectra.....	109
3-1	Kinetics of hydrogen evolution for various reactions.....	112
3-2	Kinetics of hydrogen evolution during different catalytic cycles. ....	114
3-3	Surface area versus number of cycles of the supported material.....	115
3-4	Kinetics of the unsupported catalyst during successive cycles.....	116
3-5	Decay of the surface area for the unsupported catalyst after successive cycles. ....	116
3-6	Kinetics of the reactions at 30°C, 40°C, 60°C, and 85°C. ....	118
3-7	Arrhenius plots for the non-catalyzed (circles), for the unsupported powder (triangles), and for the supported powder reactions (squares). ....	121
3-8	FTIR spectrum of the reaction products using the unsupported catalyst. ....	125
3-9	FTIR spectrum of the reaction products using the supported catalyst. ....	126
3-10	XRD patterns of the products from the catalyzed reactions.....	126
3-11	Predicted composition of the reaction products from the reaction conducted with unsupported catalyst. Results are given in wt-%.....	128

3-12	Predicted composition of the reaction products from the reaction conducted with supported catalyst. Results are given in wt-%. ....	128
3-13	Rietveld refinement of the products of the reaction performed with unsupported catalyst. ....	129
3-14	Rietveld refinement of the powders from the reaction performed with the supported catalyst. ....	130
A-1	Nickel boron metallic glasses. ....	139
A-2	Nickel boron metallic glasses with cubic symmetries. ....	139
A-3	Calculated isotropic shielding for the orthorhombic structure of NiB <sub>3</sub> .....	141
A-4	Calculated isotropic shielding constants of the monoclinic structure of NiB <sub>3</sub> . ...	142
A-5	Experimental NMR spectrum of hydrolyzed (room temperature) NiB <sub>x</sub> (black) and simulation (red). ....	143
A-6	Literature reported <sup>11</sup> B NMR spectra: a) NbB <sub>2</sub> , b) amorphous boron, and c) LiBO <sub>2</sub> . ....	143
A-7	The TPPM pulse sequence. ....	144
A-8	NMR MAS spectrum of the non-hydrolyzed powders. ....	145
A-9	Temperature dependent EPR spectra of the non-hydrolyzed powders. ....	147
A-10	Hysteresis cycles at temperatures between 1.8 and 10 K. The inset shows the coercivity curve. ....	148
A-11	Hysteresis of nanoparticles stored in open air (A) and under nitrogen (B). .....	149

## LIST OF ABBREVIATIONS

APS	Advanced Photon Source, Argonne, IL
BET	Brunauer-Emmett-Teller isotherm analysis for surface area determination
$Cmcm$	Centered – orthorhombic cell
$\delta_{iso}$	calculated isotropic chemical shift based on the average $\alpha$ -boron shielding
$\Delta_f \bar{H}_0$	Molar enthalpy of formation, calculated at 0 K
DoE	Department of Energy
$E_a$	Activation Energy-Energy barrier that the system has to overcome for the chemical reaction to occur
EDXS	Energy dispersion x-ray spectroscopy
EFG	Electric field gradient
FCC	Face centered cubic lattice
FFT	Fast Fourier Transform
FT-IR	Infra – Red Spectroscopy with Fourier Transform
$F4\bar{3}m$	Cubic cell
HSM	Hydrogen storage materials
HT – XRD	High Temperature XRD
ICP-AES	Induced coupled plasma-Atomic Emission Spectroscopy
$I4/mcm$	Tetragonal cell
MAIC	Major Analytical Instrumentation Center
MAUD	Materials Analysis Using Diffraction
MSE	Material Science Engineering
NMR	Nuclear Magnetic Resonance

PEMFC	Polymer Electrolyte membrane Fuel Cell
<i>Pnma</i>	Primitive orthorhombic cell
<i>P2<sub>1</sub>/c</i>	Monoclinic cell
<i>P<math>\bar{4}</math>2<sub>1</sub>/c</i>	Primitive tetragonal cell
<i>P6/mmm</i>	hexagonal close packed structure
RC-SS	Room Conditions – Solid State
SEM	Scanning electron microscopy
$\sigma_{iso}$	calculated isotropic chemical shielding
TEM	Transmission Electron Microscopy
TMB	Transition metal borides
XRD	X-ray diffraction (on powdered materials)

Abstract of Thesis Presented to the Graduate School  
of the University of Florida in Partial Fulfillment of the  
Requirements for the Degree of Master in Science

SOLID STATE SYNTHESIS OF NICKEL BORIDES AS CATALYSTS FOR HYDROGEN  
EVOLUTION

By

Fabrizio Guzzetta

August 2013

Chair: Alexander Angerhofer  
Major: Chemistry

Nickel borides have recently drawn attention for the mild conditions needed in catalyzing the hydrolysis of alkaline  $BH_4^-$  solutions, with consequent hydrogen evolution.

We report a new solid state procedure, under normal laboratory conditions, which produces amorphous nickel borides. Silica supported catalysts were also prepared, through slight variation of such method, in an attempt to increase catalyst surface area.

Experimental techniques and theoretical predictions were performed to characterize the products. Theoretical calculations were based on  $NiB_3$  stoichiometry. However, to date, no experimental results confirmed the calculated structures. Thermal analysis revealed no evidence for crystallization of the powders in the range of temperatures surveyed (298 – 1300 K). IR spectra on the non-hydrolyzed powders revealed few extra vibrations not seen in neat borohydride. Annealed powders exhibited spectra that were similar to those of neat  $MgB_2$  and  $KBr$ , making assignment of vibrational frequencies difficult.

XRD on the as-prepared powders confirmed  $NaBH_4$  and  $NaBr$  as main phases. A crystalline pattern has been observed after annealing at 1100 K. The formation of

metallic Ni and NiO was also revealed, because of aging and air-exposure of the powder.

XPS showed two B 1s peaks at ~182 and ~192 eV. The B 1s peak with a binding energy of 182 eV and the 10 eV difference between the two peaks have not been reported before. Nickel 2p<sub>3/2</sub> peaks fall in the range of NiO peaks. However, XRD revealed a predominance of Ni over NiO, complicating the explanation of the XPS results.

Elemental analysis (ICP-AES) resulted in molar B:Ni ratio of 2.1, confirming a boron-rich phase of these nickel borides.

TEM images revealed a regular patterning in terms of linear ridges in the material, which may be due to residual crystallinity of the material, despite of the appearance of an amorphous overall structure.

Catalyzed hydrolysis of sodium borohydride in alkaline solutions (pH ~14) were performed at 30°, 40°, 60°, and 85° C. Cycling of the active materials, surface analysis and chemical composition of the hydrolysis products were also studied. Analysis of kinetic data yielded 88% and 77% hydrogen evolution for non-supported and supported materials, respectively, within 20 minutes.

# CHAPTER 1

## TRANSITION METAL BORIDES AS HYDROGENATION CATALYSTS

### 1.1 Introduction

One of the biggest challenges encountered today in researching feasible solutions to use hydrogen as an energy carrier is its efficient storage and release. Grochala and Edwards pointed this out in the following terms:

The hydrogen storage and hydrogen energy challenge meets all the characteristics of the demanding 21<sup>st</sup> century: a stressfully short deadline, an incredible acceleration (there is an exponential shortening line between yesterday, today, and tomorrow), globalization: from the fuel crisis to the emergence of hydrogen consortia, and – nowadays – so much funding is provided by national research funds and private investments.

Presumably, those who do not attempt to solve the hydrogen storage problem right away will not even have chance to do it “tomorrow”.<sup>1</sup>

In the future Hydrogen energy may have a much larger impact on society compared to other renewable energies: differently from other sources of energy, hydrogen, the most abundant element in the entire Universe (88.6 wt%),<sup>1</sup> is an energy carrier. Therefore it can be stored, distributed and used when and where it is necessary. Energy production, by its combustion, is clean and eco-friendly because the only product is water.

Production of hydrogen<sup>2</sup> relies on several processes: 1) the natural gas reforming process which uses high temperature steam to burn natural gas, which has the disadvantage of producing non-negligible quantities of greenhouse gases. 95% of hydrogen produced in USA is still produced by this method. 2) Renewable electrolysis which takes advantage of electricity produced by other renewable energies such as solar, wind, hydroelectric, tidal, etc. to split water into its components hydrogen and oxygen. 3) Gasification of coals which involves burning of coal to produce hydrogen.

This is more efficient than burning coal to produce electricity, but at the same time, produces large quantities of CO<sub>2</sub>. 4) Renewable liquid reforming processes which starts with biomass after its conversion into bio-diesel or bio-ethanol, and uses high temperature steam. 5) High temperature electrolysis using nuclear plants to split water into its components. This still remains a costly and dangerous process for the production of hydrogen. 6) High temperature thermochemical water splitting which still is expensive, and 7) photoelectrochemical and photobiological water splitting which with the promise of clean H<sub>2</sub> production and greatly diminished cost.

In the near future, the main goal is to use hydrogen as a fuel in the transportation industry. In spite of the economic and ecological advantages offered by hydrogen use for transportation, there are several bottlenecks that hinder its widespread use. Compressed hydrogen gas, and liquid hydrogen (LH<sub>2</sub>) devices are currently under study,<sup>3</sup> but the production of highly pure hydrogen is really expensive and not practical from an economical point of view.

The safety of these devices<sup>3</sup> has been improved over the years. Yet, issues still remain which need to be addressed soon to facilitate the use of gaseous or liquid hydrogen for use in transportation.

### **1.1.1 Compressed Hydrogen**

Compressed hydrogen gas storage devices have been recently developed by Quantum Technologies (Figure 1-1).<sup>3</sup>

These devices are reinforced with carbon fiber to eliminate structural safety issues such as hydrogen leaking out from the device through microscopic cracks. Some of these devices have already been placed into service in hydrogen fueled vehicles.<sup>3</sup> However, other issues need to be resolved. Since hydrogen is very reactive storage

under high pressures raises important safety concerns. Moreover, the weight of the storage device limits its use in the automotive industry because of the need for increased engine performance. Conformability and size of the device is another issue. In fact, due to the stiffness of the materials used and the need for sufficient storage capacity which increases size there are few possibilities of placing the device inside vehicles which in turn limits the realization of prototypes. The cost of production of these devices is also still prohibitive.<sup>3</sup>

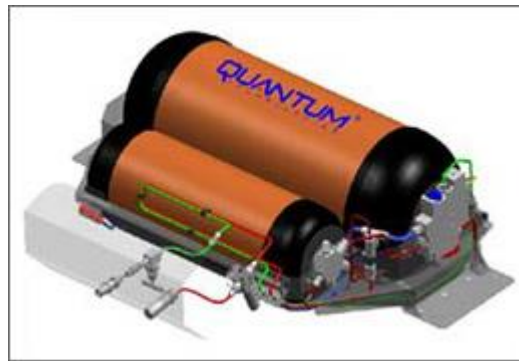


Figure 1-1. Device for compressed hydrogen gas storage from Quantum Technologies. Reprinted from [http://www1.eere.energy.gov/hydrogenandfuelcells/storage/hydrogen\\_storage.html](http://www1.eere.energy.gov/hydrogenandfuelcells/storage/hydrogen_storage.html)

The cost of production depends mainly on the structural reinforcement carbon fiber used in the manufacture of such light-weight devices. To overcome these issues, the E.E.R.E. agency of the D.O.E. reports:

Two approaches are being pursued to increase the gravimetric and volumetric storage capacities of compressed gas tanks from their current levels. The first approach involves cryo-compressed tanks. This is based on the fact that, at fixed pressure and volume, gas tank volumetric capacity increases as the tank temperature decreases. Thus, by cooling a tank from room temperature to liquid nitrogen temperature (77°K), its volumetric capacity will increase by a factor of four, although system volumetric capacity will be less than this due to the increased volume required for the cooling system.

The second approach involves the development of conformable tanks. Present liquid gasoline tanks in vehicles are highly conformable in order to take maximum advantage of available vehicle space. Concepts for conformable tank structures are based on the location of structural supporting walls. Internal cellular-type load bearing structures may also be a possibility for greater degrees of conformability.<sup>3</sup>

### 1.1.2 Liquid Hydrogen

Due to the difficulties in overcoming the issues related to gaseous hydrogen storage, alternatively liquid hydrogen storage (LH<sub>2</sub>) devices are also studied. Storage of hydrogen in liquid form enhances the energy density of hydrogen. However, issues with LH<sub>2</sub> include the energy used for liquefaction of hydrogen; volume, weight and tank cost, and the tendency of the fuel to boil off.<sup>3</sup> Cryogenic temperatures required for liquefaction of hydrogen, are an important issue in the use of LH<sub>2</sub> devices (Figure 1-2) since 30% of the heating value of hydrogen is required to liquefy it.

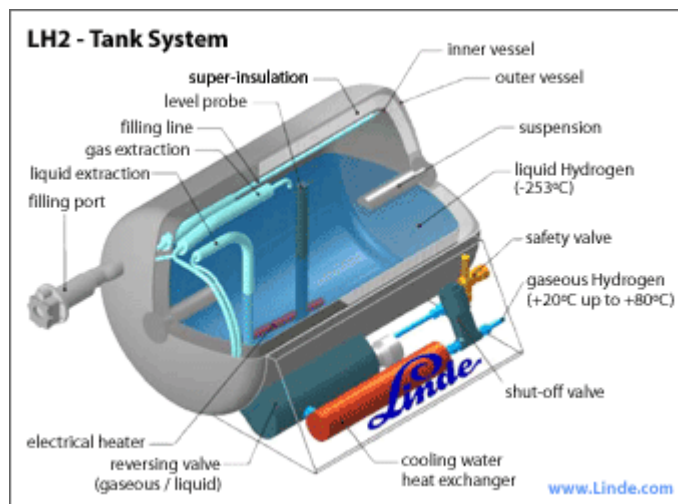


Figure 1-2. Liquid H<sub>2</sub> (LH<sub>2</sub>) tank system. Reprinted from [http://www1.eere.energy.gov/hydrogenandfuelcells/storage/hydrogen\\_storage.html](http://www1.eere.energy.gov/hydrogenandfuelcells/storage/hydrogen_storage.html)

LH<sub>2</sub> devices can store more hydrogen *per volume* than gaseous compressed hydrogen tanks.<sup>3</sup> Currently compressed hydrogen tanks are used in certain types of

vehicles. Hybrid tanks which couple compressed and liquid H<sub>2</sub> are also being studied.<sup>3</sup> However, the cryogenic temperatures needed are still a limiting factor. For this reason, new approaches for the liquefaction of the gas with lower energy requirements are needed.

All these difficulties combine to limit the use of gaseous and liquid hydrogen as of now. Yet, a third and more viable way to store hydrogen is through the solid state.

### 1.1.3 Solid Hydrogen storage

Solid state storage is currently safer and appears technologically more achievable.<sup>1</sup> In this case hydrogen atoms are chemically bound in solid materials. These materials, in principle, should reversibly desorb and absorb hydrogen gas. The *exhaust* solid (i.e., the fully dehydrogenated material) must be capable of absorbing relatively high quantities of H<sub>2</sub> gas, in order to fully (or nearly fully) restore the original material. Unfortunately, the lack of a universal storage/release material currently hinders the technological development of solid hydrogen storage/release presenting a challenge to the research community. Guidelines for solid hydrogen storage materials (HSM) have been delineated by the Department of Energy of the US government.<sup>1</sup> An ideal HSM candidate must achieve the following requirements listed below:

1. High storage capacity: minimum 6.5% wt% of hydrogen abundance is required from the material.
2. Temperature of decomposition (H<sub>2</sub> gas release) of  $T_{\text{dec}} = 60^{\circ} - 120^{\circ} \text{C}$ .
3. Reversibility of thermal adsorption/desorption cycles: low temperature of hydrogen desorption and low pressure of hydrogen adsorption are required.
4. Low cost.
5. Low toxicity and if possible a non-explosive storage medium.

Modern research in Chemistry and Chemical Engineering has helped push the material limits through the synthesis of new materials<sup>4</sup> and through the improvement of existing ones.<sup>5</sup> These new materials are starting to approach the minimum requirements established by DOE, although no single material tested up to now fulfills all required minimum limits specified by DOE. Figure 1-3 lists some of the most common hydrogen storage materials studied and their limitations. The limits set by DOE are listed as well.

Table 1-1. Comparison of the key properties of the main (condensed-phase) hydrogen storage materials. Adapted by permission from Edwards and Grochala, *Chem. Rev.*, 2004, 104, 1281 – 1305. Copyright (2004) ACS Journals.

Material	Practical H wt%	Kinetic reversibility	T <sub>dec</sub> /°C	Notes	Criteria met
PdH <sub>0.6</sub>	0.6	Excellent	Ambient	1000\$/oz	2, 3, 4
Mg <sub>2</sub> NiH <sub>4</sub>	3.6	Very good	Ambient	Fails to meet criterion 1	2, 3, 4, 5
NaAlH <sub>4</sub> :TiO <sub>2</sub>	5.5	Very good	125	Fails to meet criterion 1	2, 3, 4, 5
MgH <sub>2</sub>	7.6	Very poor	330	Cheap Mg metal	1, 4, 5
LiBH <sub>4</sub> :SiO <sub>2</sub>	9.0	So far irreversible	200-400	LiBH <sub>4</sub> high cost	5
NaBH <sub>4</sub> /H <sub>2</sub> O	9.2	Irreversible	Ambient	Expensive Ru catalyst	2, 3, 4, 5
MeOH	12.5	Irreversible	Thermal activation is difficult	Toxic liquid	1, 4
CH <sub>4</sub>	25	Irreversible	Thermal activation is difficult	Gas difficult to liquefy	1, 4
DoE limit	≥6.5	Excellent	Max 120	Safe, handy material	All

The main class of chemicals studied in this field is the hydride family. They are further subdivided into two main categories: The first category comprises the materials that are *too stable*, for which the adsorption of hydrogen is facile (requiring low or moderate hydrogen pressures), but desorption is difficult (requiring higher energies).

The second class comprises hydrides which are *too unstable* and in which desorption happens even at room (or below room) temperature and requires very high H<sub>2</sub> gas pressures to restore the parent hydride.<sup>1</sup>

Reversibility of hydrogenation/dehydrogenation cycles and extending the time of turnover of such materials are the key for the development of suitable hydrogen storage materials.<sup>1</sup>

Unfortunately, direct hydrogenation usually does not fully restore the parent HSM, therefore the reaction products have to be “*recycled*.”<sup>1</sup>

A new direction in solid hydrogen storage research addresses two important targets: 1) to lower the energy barrier of hydrogen absorption and desorption, and 2) to extend the lifetime of the parent hydride. Today, research is focused on heterogeneous catalysis and trying to individuate catalyzed reactions for hydrogen evolution,<sup>6-10</sup> or, alternatively, catalyzing the hydrogenation of inorganic materials which can either absorb or chemically react with intake hydrogen and to form the parent hydride to be used as hydrogen storage material.<sup>11,12</sup>

Metal-doped sodium and lithium alanates (Na/LiALH<sub>4</sub>) were first identified by Bogdanovic and Schwickardi as promising hydrogen storage materials.<sup>5</sup> However, they have lost some of their appeal in favor of borohydrides which appear to have more potential to attain the DoE limits.<sup>6,7,10,13-20</sup>

In fact, metal borohydrides are very well known chemicals with an important role in the chemicals market and in industry.<sup>21</sup> The first metal borohydride to be synthesized was LiBH<sub>4</sub> from the reaction of ethyllithium with diborane.<sup>22</sup>

The most widely synthetic route to metal borohydrides is the direct combination of the elements under high hydrogen pressure. Metal borohydrides such as  $\text{LiBH}_4$ ,  $\text{NaBH}_4$ ,  $\text{Mg}(\text{BH}_4)_2$  and  $\text{Ba}(\text{BH}_4)_2$  were synthesized this way and reported in a patent by Goerrig.<sup>23</sup> Alternatively, metathesis reactions between lithium or sodium borohydrides and metal salts are also widely used, especially in the synthesis of complex borohydrides, according to the following schemes:



The attractiveness of metal borohydrides as hydrogen storage materials stems from their high hydrogen content as seen in Table 1-2.<sup>21</sup>

Table 1-2 Hydrogen storage properties of selected high capacity hydrides, adapted from R. A. Varin, T. Czujko, Z. S. Wronski, "Nanomaterials for Solid State Hydrogen Storage," Springer 2008. Copyright Springer (2008)

Metal	Hydride	Theoretical maximum gravimetric H <sub>2</sub> capacity (wt%)	Theoretical reversible gravimetric capacity (wt%)	Approx. desorption temperature range (°C)
Li	$\text{LiBH}_4$	18.4	~13.8	~470
Mg	$\text{Mg}(\text{BH}_4)_2$	14.9	~11.2	~300
Fe	$\text{Fe}(\text{BH}_4)_3$	12.1	Unknown	Unknown
Ca	$\text{Ca}(\text{BH}_4)_2$	11.6	Unknown	~320 (?)
Na	$\text{NaBH}_4$	10.6	10.6	400 – 600
Zn	$\text{Zn}(\text{BH}_4)_2$	8.5	8.5 (?)	85 – 140

As a category, metal borohydrides constitute the storage materials with the highest gravimetric hydrogen content.

Unfortunately, one of the main issues for engineering devices which use them as hydrogen storage solids, arise from the difficulty of recovering the parent hydride once the hydrogen has fully desorbed. In fact, reversible thermal hydrogenation/dehydrogenation cycling in solid state metal borohydrides is not feasible

due to the formation of stable structures with the general formula  $M_2B_{12}H_{12}$  ( $M = Li, Na, K$ ).<sup>24,25</sup> In fact, due to the formation of these stable compounds, the process will not regenerate the initial reactants, blocking the reversibility of hydrogen cycling.

Chemical manipulation or modification of the metal borohydrides (in order to achieve suitable implementation for hydrogen storage, as required by DOE) is complex. Inert atmospheres are sometimes required for suitable chemical manipulation, due to their reactivity towards oxygen and due to their hygroscopic nature.

As a result of these difficulties the hydrolysis of sodium borohydride for hydrogen generation is currently seen as more technologically achievable,<sup>6-8,10,15,17-20,26</sup> because that the reaction happens in solution which makes the system easier to handle, 2) the reaction products are non-toxic (the literature implies that the only product from the reaction of hydrolysis is just sodium metaborate), and 3) the mild conditions used for the reaction (generally room temperature and pressure). These benefits have led researchers to focus on optimization of the reaction conditions for hydrogen production. Generally, the reactions between the parent hydrides and water are exothermic, and release very pure hydrogen gas.<sup>1</sup> However, return of the “*products*” into “*reactants*” is difficult and requires high energies, potentially canceling out the economic advantage of using hydrogen as a fuel.<sup>1</sup> Nonetheless, much research is focused on this area due to the low cost of the starting materials, the mild reaction conditions, and the lack of toxic byproducts.

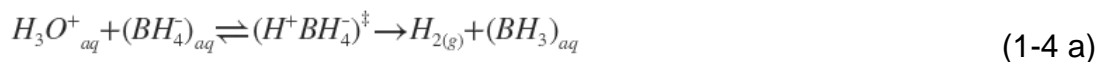
#### **1.1.4 Hydrolysis of Sodium Borohydride**

The reaction of the hydrolysis of sodium borohydride is very well known in the literature.

It proceeds according to Eqn. 1-3:



The reaction mechanism is pH sensitive, and the whole reaction is acid-catalyzed, as demonstrated by Davis and coworkers:<sup>27,28</sup>



In an attempt to identify the possible activated complexes of the reaction, Davis and coworkers performed experiments with heavy water and deuterated acids. Under these conditions, they identified two transition states, shown in Figure 1-3.

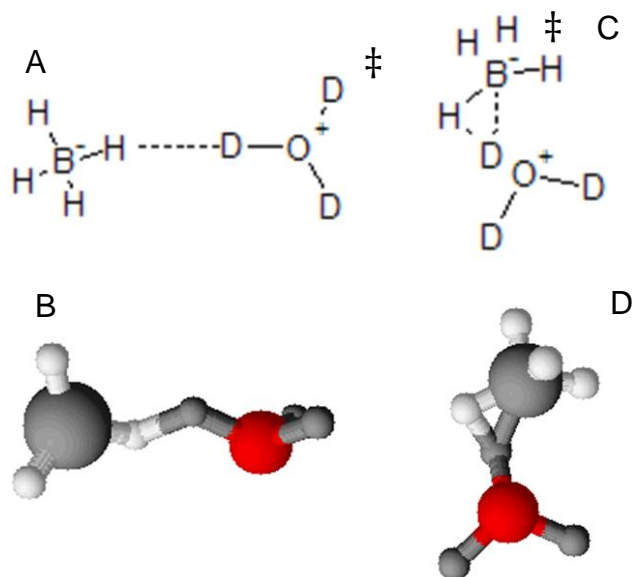


Figure 1-3. Activated complexes in acidic hydrolysis of sodium borohydride. Reprinted by permission from Davis et al., JACS, 1961, 84, 6, 885 – 892. Copyright 1962, American Chemical Society. A and C 2-D structures; B and D 3-D structures which clarify the open and ring structures of the intermediates. Color codes: hydrogen in white; oxygen in red; Boron and Deuterium in black

In each of these experiments, pH was maintained constant at a specified level.

Davis and coworkers performed the reactions in the whole range of pH values between 0 and 14, demonstrating pH dependency of the reaction rate. The logarithm of

k versus pH is linear for a large pH range between 7.5 and 12 but becomes non-linear for very high values of pH above 12, with k showing very small values. This relationship is presented in figure 1-4.

However, in 2009 Liu and coworkers published an extensive review in which they pointed out the advantages and limitations of this reaction in producing hydrogen.<sup>8</sup> The work was intended to emphasize the engineering challenges encountered when designing fuel cell devices based on this reaction.

In recent years most studies have focused on facilitating improvements in hydrogen evolution.<sup>15,16,18,20,29</sup>

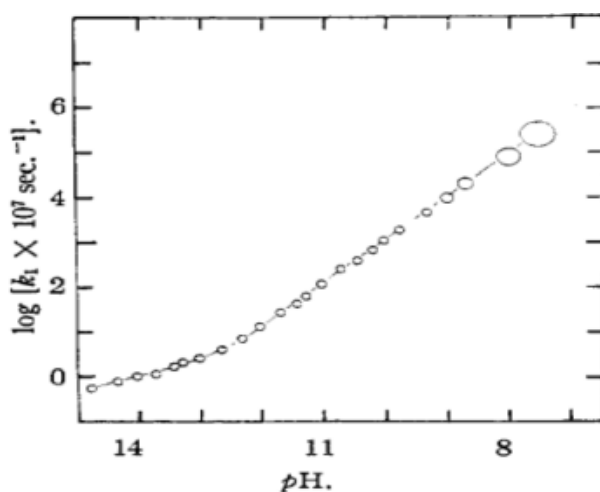


Figure 1-4. Log(k) versus pH plot for the hydrolysis of sodium borohydride, reprinted by permission from Davis, R. E., Kibby, C. L., and Swain, C. G., JACS Communications to the Editor, 82 (1960) 5949 – 5950. Copyright JACS (1960).

Recently, Demirci et al. summarized the state-of-the-art in this area in an extensive review.<sup>18</sup> Churikov et al. investigated the effect of temperature and solution alkalinity on the rates of sodium borohydride hydrolysis.<sup>15</sup> Matthews and Yu studied the reaction of hydrolysis in concentrated aqueous solutions.<sup>17</sup> Retnamma, Novais and

Rangel conducted a review of all available kinetic data collected for this reaction under different reaction conditions.<sup>20</sup> Sahin et al. studied the reaction of hydrogen production from sodium borohydride in the presence of electric fields.<sup>16</sup>

Catalyzed reactions (in the hydrolysis of stabilized solutions of metal borohydrides) for hydrogen evolution have also attracted interest in lowering the energy barrier for hydrogen evolution. However, Retnamma, Novais, and Rangel pointed out that in order to engineer suitable systems based on this reactions the catalyzed hydrolysis of sodium borohydride is highly exothermic and therefore heat needs to be removed through an efficient control system.<sup>20</sup>

The synthesis of the catalysts may require refluxed reaction<sup>30</sup> (long reaction time and many steps) before their isolation and characterization. Sometimes the synthesis requires an inert atmosphere.<sup>31</sup> For this reason, transition metal borides are currently drawing more attention, since they do not require complicated, long synthetic steps. Numerous papers<sup>6-10,26,32-41</sup> have shown them to be efficient in the hydrogenation of various organic molecules,<sup>9,32-36</sup> or the dehydrogenation of sodium borohydride at very alkaline pH (pH $\geq$ 13.00).<sup>6-8,10,26,37,39-44</sup> Nickel and cobalt, in particular, seem to show the highest catalytic power.<sup>6,10,26,39-41</sup>

Catalyzed sodium borohydride hydrolyses have been widely studied from a kinetic point of view. The main factors affecting the rate of the reaction are: 1) the amount of catalyst, 2) the concentration of the sodium borohydride and ionic strength effects, 3) the acid-base equilibrium between borate and boric acid, and 4) pH.

However, the *metal* catalyzed reactions are independent of the pH.<sup>20</sup> As reported by Retnamma, Novais, and Rangel the kinetics of this reaction has been described

using zero, first, and second order rate laws, other power laws, and the Langmuir-Hinshelwood and Michaelis-Menten mechanisms as well as semi-empirical models have been invoked to explain the behavior of the *metal* catalyzed sodium borohydride hydrolysis.<sup>20</sup>

To date there is little agreement in the literature on the kinetic model for this reaction. It is therefore difficult to determine the activation energies of the catalyzed reactions since theoretical energies differ depending on the model used to simulate the kinetic constants.

## 1.2 History of TMB and their Classification.

Metal borides have been employed in several technological applications due to their covalent boron framework which provides them higher chemical, thermal, and mechanical stability.<sup>45</sup> A tentative classification of the various structures was given in 1987 by Ganem and Osby,<sup>36</sup> which used, as classification parameters, boron content and the presence of a boron–boron bonding framework:

Historically, borides were first produced by the combination of boron with metallic or metalloidal elements less electronegative than itself. For the most part, borides are very hard, high-melting, refractory substances whose structures and stoichiometries do not conform to the ordinary concepts of valence. Borides with low boron-to-metal ratios ( $M_4B$ ,  $M_3B$ ,  $M_2B$ ) contain isolated boron atoms, however as the proportion of boron increases ( $M_3B_2$ ,  $M_4B_3$ ,  $M_3B_4$ ), borides with single and double chains of borons appear. Borides with formulae like  $MB_4$ ,  $MB_6$ , and  $MB_{12}$  exist in three-dimensional arrays with open networks of boron atoms interpenetrating a regular metal atom lattice.

The history of metal borides is quite long since they were discovered more than a century ago.<sup>46,47</sup> The first experiments were performed to understand boron solubility in metals or alloys. Clearly, at that time the goal was to obtain information for metallurgical applications in hardening of alloys or making them more rust–resistant.

Nickel borides exist in a variety of stoichiometries and molar ratios such as  $\text{Ni}_x\text{B}$ , where  $x = 1, 2, 3$ .<sup>48-50</sup>  $\text{Ni}_4\text{B}_3$ , shows boron–boron chains.<sup>51,52</sup> Species with a higher content of boron versus metal are not known to form under mild external conditions, and very few are reported under any condition. The only ones reported are  $\text{NiB}_2$ ,<sup>46,47</sup> but only at  $1590^\circ\text{C}$ ,<sup>53,54</sup> and  $\text{Ni}_2\text{B}_3$ , as reported by Rundqvist.<sup>52</sup>  $\text{NiB}_{12}$  is reported as nickel intercalation into a boron lattice (Portnoi *et al.*<sup>55,56</sup>) and  $\text{NiB}_{-24}$  has also been reported using thermal high temperature annealing of nickel and boron as nickel intercalation in a boron lattice which remains very close to the boron lattice.<sup>57</sup>

Clearly, the stoichiometry as well as the properties of the nickel borides depends on the synthetic method used.<sup>58</sup>

There is still a vigorous debate about the existence of  $\text{NiB}_2$  with numerous proposed phase diagrams.<sup>53-56,59-65</sup> However, there is no definitive proof for this stoichiometry.

Early syntheses were performed by annealing metal salts (or oxides or simply the element) in furnaces, with boron, above  $1000^\circ\text{C}$ .<sup>46,47,51,52,66,67</sup> Often during the synthesis a carrier gas was used to remove gaseous byproducts or prevent oxidation in air. Rundqvist writes about this process:

However, the composition of the boron–rich alloys did not correspond to the weighed amounts of the starting materials since varying amounts of boron were unavoidably lost during the reactions.<sup>52</sup>

In 1933 Alfred Stock from Cornell University was the first to report a wet chemistry synthesis through the reaction of sodium borohydride and metal salts in solution. He found a black precipitate generally called *metal boride* combined with the evolution of hydrogen.<sup>13</sup> This synthetic procedure is still the most commonly used process in the preparation of nickel and cobalt borides. In 1953 H. Schlesinger and

coworkers noticed that embedding 5 wt% of Co(II) salt in a matrix of borohydride and pressing the mixture into a pellet facilitated the evolution of hydrogen under application of an external electric field.<sup>14</sup> In the 1990s an Italian group at the University of Cagliari discovered that the milling of elemental nickel and boron formed big clusters of nickel borides whose stoichiometry was determined in atom-% as Ni<sub>80</sub>B<sub>20</sub> or Ni<sub>60</sub>B<sub>40</sub>.<sup>68</sup> In 2011 an Iranian group followed up on this study, establishing milling time–dependent phase transitions and discovering that annealing these clusters to a predetermined temperature transformed them into Ni<sub>3</sub>B (at 350°C) or Ni<sub>2</sub>B (at 700°C).<sup>69</sup> Portehault *et al.* recently reported a synthesis under moderate conditions in a crucible heated between 500° and 900°C using an eutectic molten LiCl:KCl mixture as the solvent. Calcium and niobium salts were co-dissolved with sodium borohydride and reduced to form nanocrystalline high–boron content metal borides.<sup>45</sup> The main disadvantage of this method is the isolation of the powders, because an excess of sodium borohydride, after hydrolysis, form a coating composed of amorphous boron oxide which makes difficult the isolation of the nickel borides alone. Chemical characterization has been complicated by the fact that mild synthetic conditions coupled with a wet chemistry approach normally give amorphous products that are difficult to characterize. However, Albert and coworkers were able to form crystalline Ni<sub>2</sub>B using wet chemistry.<sup>49</sup> In many cases a deeper understanding of these structures is only possible when referenced to similar crystalline materials, or through calculations.<sup>70-73</sup> High temperature synthetic approaches normally form crystalline compounds aiding structure determination. Kiessling synthesized a massive number of crystalline metal borides and used X-ray crystallography to characterize the products;<sup>66,67</sup> Rundqvist focused on the synthesis

and X-ray characterization of orthorhombic and monoclinic  $\text{Ni}_4\text{B}_3$ .<sup>51,52</sup> However, these syntheses usually produce nickel-rich phases, even though  $\text{NiB}_2$  has been reported. (ref. Howe). Physico-chemical properties of many of these crystalline materials have also been determined.<sup>63,74</sup> Molvinger and coworkers, instead, reported the synthesis of  $\text{NiB}_2$  from dry THF solutions and its use as hydrogenation catalyst of organic molecules.<sup>75-77</sup> In 2001, they reported the synthesis of various metal boride catalysts with a 1:2 metal to boron composition, except for Fe/B which resulted in a 1:1.8 stoichiometry. The synthesis of boron-rich phases, with boron to nickel ratio  $>2$ , under mild to medium external conditions is still untested territory.

### **1.3 Metal Borides as Hydrogenation Catalysts**

Research on the catalytic properties of metal borides has matured in the last 60 years. Buisson, Paul, and Joseph were among the first to report kinetic studies of hydrogen evolution from nickel boride, i.e., catalyzed reactions from stabilized sodium borohydride solutions.<sup>34</sup> They compared the results coming from these compounds to various other nickel-based catalysts. The results showed that nickel borides presented almost the same activation energies as Raney nickel.<sup>34</sup>

In 1970, Brown<sup>33</sup> reported the activity of nickel boride catalysts prepared with wet chemistry procedures, called P-1 and P-2. P-1 refers to the product coming from the reaction performed in water solutions, while P-2 refers to the same product coming from the reaction performed in ethanol solutions. Generally speaking, the notation P-1 (water) and P-2 (ethanol) has been maintained for all the reaction performed under wet chemistry. Sometimes non-integer numbers were used to index mixtures of water and ethanol (with different compositions) that were used as solvents.<sup>50</sup> Reaction products looked very different depending on the procedure used. Water-based reactions gave a

finely grained black precipitate, while ethanol solutions yielded colloidal black suspensions. These compounds, once isolated and properly characterized, were used to hydrogenate unsaturated organic molecules. The ethanol-prepared catalyst turned out to be more sensitive to double bonds than the one prepared in water. In 1982, Collins and coworkers described the hydrogenation of nitrobenzene over a nickel boride catalyst, claiming that the reaction “*does not produce appreciable concentration of reaction intermediates during the liquid phase hydrogenation of nitrobenzene.*”<sup>35</sup>

Ganem and Osby extensively studied several metal borides and aluminides, as catalysts for a variety of organic hydrogenations. They described various syntheses of TMB and transition metal aluminides, which were used successively as catalysts for hydrogenation of organic compounds, namely unsaturated compounds.<sup>36</sup>

Skrabalak and coworkers, in 2006, explored the possibility of metal boride intervention in catalyzing contemporarily hydrogenation and desulphurization reactions, using thiophene as substrate, comparing the final products with standard polysulfides of nickel and cobalt and proving the formation of organic residues with four carbon atoms.<sup>38</sup>

Li and coworkers used nickel borides to hydrogenate acetonitrile to ethylamine. Nickel borides led to the formation of several polyamines with a predominant formation of primary amines. However, due to poor selectivity of the catalysts, the formation of secondary amines could not be avoided.<sup>39,40</sup>

The reactivity and selectivity of the nickel boride yields primarily diethylamine, while the Raney nickel shows comparable quantities of both of the ethylamine and diethylamine, as shown in figure 1-5.

The catalytic activity of nickel borides with higher boron content has not been reported yet. However, in 2002 Hanxi<sup>6</sup> described the use of a  $Ni_xB$  catalyst that was formed when nickel salts were mixed with an alkaline solution of sodium borohydride. The content of nickel was 4 to 5 times that of boron. Hydrogen evolution kinetics were measured under various conditions, and the effect of sodium hydroxide concentration was examined.

Liu<sup>7</sup> studied the kinetics of hydrogen evolution from alkaline solutions of sodium borohydride in the presence of metallic salts, namely  $Ni^{2+}$  and  $Co^{2+}$  ions, at various temperatures. The investigation included the role of the salts as well as  $Ni_2B$  and  $Co_2B$ , Raney Ni and Co, and a Raney mixtures of Ni and Co. Kinetic experiments showed the rates depended among other factors on catalyst performance, the concentration of  $NaBH_4$ , (which slightly affected the hydrogen generation rate), and the concentration of NaOH. Increasing the concentration of NaOH beyond a threshold of 20 wt% decreased the production of hydrogen.

In Figure 1-6 the kinetics of hydrogen evolution as a function of NaOH wt-% is shown.

Studies showed nickel nanopowder is able to strongly diminish diborane evolution and to promote hydrogen evolution from  $Zn(BH_4)_2$ .<sup>43,44</sup> In 2006, a Korean group was able to synthesize  $Zn(BH_4)_2$  through ball milling and used thermal analysis to decompose the compound.<sup>42</sup> The study revealed high quantities of  $B_2H_6$  in the decomposition products, making them unsuitable for HSM.<sup>42</sup> Since  $Zn^{2+}$  is a closed shell  $d^{10}$  ion, and  $BH_4^-$  a reductant, upon thermal decomposition, the system responded by producing diborane gas rather than hydrogen, and failed to reduce the metal centers.

In 2007 Yogi Goswami and coworkers<sup>43,44</sup> used different compounds to dope Zn(BH<sub>4</sub>)<sub>2</sub> in an effort to eliminate, or strongly reduce, diborane gas evolution by thermal decomposition of zinc borohydride. Several inorganic candidates were chosen: TiCl<sub>3</sub>, metallic nano Ni, metallic nano Fe, TiF<sub>3</sub>, metallic Ti, and metallic nano Ti and Zn.

The intent, apart from preventing the production of diborane, was to also lower the decomposition/gas desorption temperatures into the range of 50-100°C without drastically affecting hydrogen content per weight of the sample. Adding 1.5 mol-% of nickel nanopowder to freshly milled Zn(BH<sub>4</sub>)<sub>2</sub> decreased diborane evolution by a factor of 20, and simultaneously promoted hydrogen evolution at lower decomposition temperatures (about 120°C) of the sample.

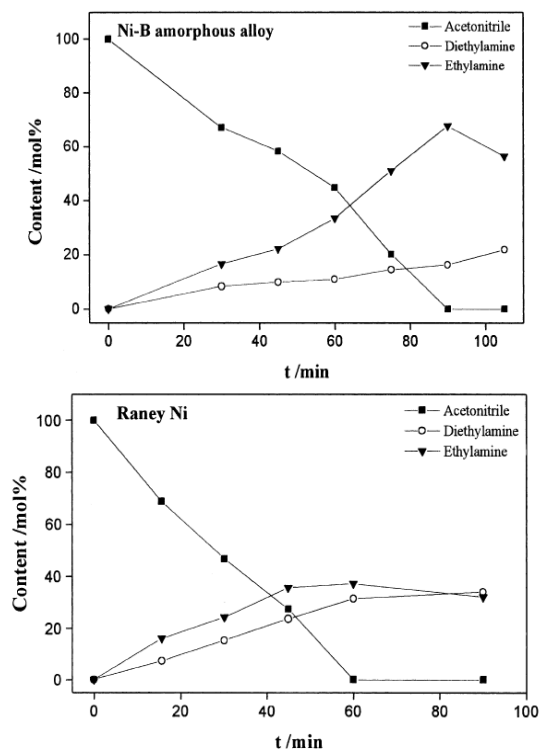


Figure 1-5. Comparison of the catalytic activity of amorphous Ni<sub>2</sub>B and Raney nickel in the hydrogenation of acetonitrile. Reprinted by permission from by Li et al.<sup>39</sup> Copyright Elsevier (2003)

In 2008 an Argentinian group<sup>9</sup> reported the doping of nickel boride with 4 wt-% of several transition metal ions, and evaluated the effects on its catalytic properties.

Samples were prepared by reacting  $\text{BH}_3\text{-THF}$  complex, in anhydrous THF, with metal salts solutions.

The magnetism of the various metal borides synthesized was also investigated.

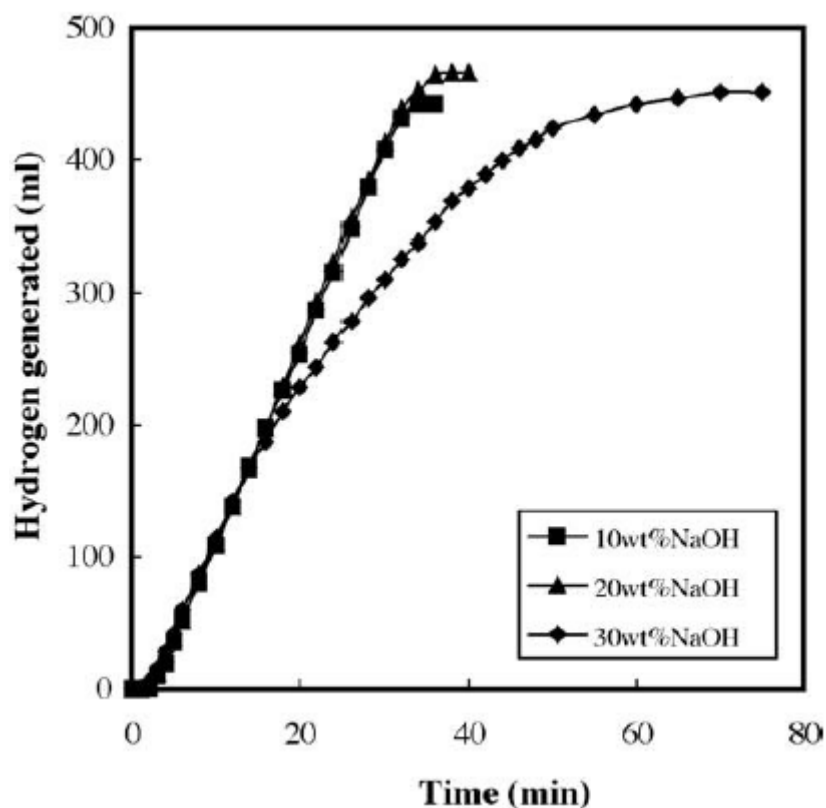


Figure 1-6. Hydrogen evolution kinetics as a function of the wt-% of sodium hydroxide. Reprinted by permission from Liu *et al.*<sup>7</sup> Copyrights (2006) Elsevier.

The synthesis formed amorphous structures which crystallized upon annealing, as confirmed by thermal analysis and XRD.

These compounds were used in the investigation of the hydrogenation of nitrobenzene, which (as reported by Chen and Chen<sup>78</sup>) has a low kinetic rate which is

1<sup>st</sup> order in nickel boride and 0<sup>th</sup> order in nitrobenzene. Acosta et al described that “*the metal dopants act as ions which improve the polarization of the group that needs to be reduced*” (which in this case was the nitro group in nitrobenzene).<sup>9</sup>

In 2005, Liaw *et al.*<sup>37</sup> used polymer stabilized nickel boride as a catalyst. Hung *et al.*<sup>10</sup> used Ru-based catalysts and investigated the kinetics of hydrogen evolution from sodium borohydride.

In view of these reports, there are several questions that need to be addressed:

1. *Are nickel borides true catalysts?* This does not seem to be the case. In fact, alkaline solutions of sodium borohydride will not release hydrogen without *reacting* with the ion salts in solution, reducing the metals, and forming nickel borides. Nickel borides as catalysts are not usually analyzed *after* the reaction to determine if the molar ratio of the elements is unchanged. Li and coworkers<sup>39</sup> also showed that the catalyst, upon thermal annealing, crystallizes out metallic nickel clusters, showing that boron was oxidized even in inert N<sub>2</sub> atmosphere.
2. *What are the reaction products from the hydrolysis?* The literature is silent on the analysis of the products from catalyzed reactions: it implies that the products of reaction are NaBO<sub>2</sub> and H<sub>2</sub>. However, a rigorous chemical and elemental analysis still has to be performed.
3. *What is the mechanism of the reaction?* A mechanism for the reaction still has to be described.
4. *How much does the surface of the supported catalysts change upon cycling?* Surface degradation is one of the issues that need to be solved especially since the shock provoked by the hydrogen evolution may degrade the surface so quickly that the recovery of the whole catalyst is impossible (Li et al.<sup>40</sup>)

The aim of this thesis, besides the synthesis of boron-rich metal borides under mild conditions, is to address some of the open questions.

However, independently from the synthetic method chosen for these materials, it is very difficult to obtain nickel borides with high purity. In fact, the most common methods of synthesis form products which are completely covered by an amorphous boron oxide layer. The literature is silent on the effects that sodium borates or boron oxides might

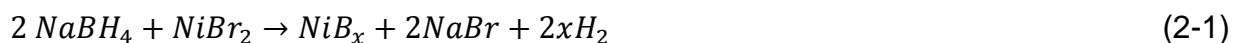
have on hydrogen evolution from alkaline sodium borohydride solutions. Therefore, the role of the boron oxide matrix in such reactions is still uncertain. However, despite all of this, kinetic tests have already been performed using various catalysts in catalyzing hydrogen evolution from highly alkaline solution of sodium borohydride.<sup>6,10,20,79</sup> A reaction mechanism for the catalyzed hydrogen evolution from sodium borohydride has not yet been proposed and goes beyond the scope of this work. However, catalytic cycles and kinetic studies are still missing on boron-rich nickel borides. They are needed in order to understand the reactivity and/or catalytic activity of the synthesized compounds, to establish reaction rates and to determine activation energies. In fact, the literature reports only on nickel-rich phases for the nickel borides used in catalysis.<sup>6,33-35,39,40,50,80</sup> There are a few reports on the use of NiB<sub>2</sub> as a hydrogenation catalyst.<sup>75-77</sup> However, it is important to understand if nickel borides with boron rich phases are equally capable to catalyze the hydrogenation of reducible organic groups, or, alternatively, when alkaline solutions of sodium borohydride are used for hydrogen evolution.

CHAPTER 2  
SYNTHESIS AND CHARACTERIZATION OF NiB<sub>x</sub>

**2.1 Synthesis of NiB<sub>x</sub>**

Sample preparation was performed with solid state reactions between NiBr<sub>2</sub> and NaBH<sub>4</sub> under laboratory conditions.

The chemical equation governing these reaction is:<sup>81</sup>



According to this equation the stoichiometric content of boron versus nickel must be B/Ni ≥ 2 in order to obtain boron-rich nickel borides.

According to Varin, et al. the milling of ions such as Mg(II) or Zn(II) with sodium borohydride leads to the formation of complex borohydrides through a metathesis reaction, since the reducing BH<sub>4</sub> units are not strong enough to reduce Mg(II) and Zn(II) to the respective metal (or metal borides) forms.<sup>21</sup>



We assume that the formation of NiB<sub>x</sub> passes through an initial, relatively slow formation of complex borohydrides, such as Ni(BH<sub>4</sub>)<sub>x</sub>, which successively decays into NiB<sub>x</sub> and H<sub>2</sub>, according to the general chemical equation:



Since Ni is often found in its +2 oxidation state, our initial hypothesis was that the reaction would proceed as follows yielding a 2:1 ratio of B:Ni in the final product:



We chose this synthetic procedure because: 1) it is inexpensive, 2) we expect higher boron content at room or slightly elevated temperatures (due to higher local availability of boron than in solution) and 3) ease of handling (it does not require

manipulation of the reactants, a lot of time, and/or sophisticated equipment for the synthesis or synthetic skills because the powders are used as received). This procedure involves only a few simple steps: *milling* of the reactants and isolation of the product through washing out the water-soluble by-products and hydrolysis of excess  $\text{NaBH}_4$ .

Initially we tested the reaction by varying the relative nickel concentration. 2.5, 5, 7.5 and 10 mol-% nickel in the form of  $\text{NiBr}_2$  was added to a constant amount of  $\text{NaBH}_4$  (10 mmol). The reactants come in powdered form and were purchased from Acros Organics and used as received. The powders were quickly weighed on a micro-g scale under normal atmospheric conditions and put in a clean 25 mL 3-neck round bottom flask and a magnetic stir bar added. The experimental apparatus is shown in figure 2-1.

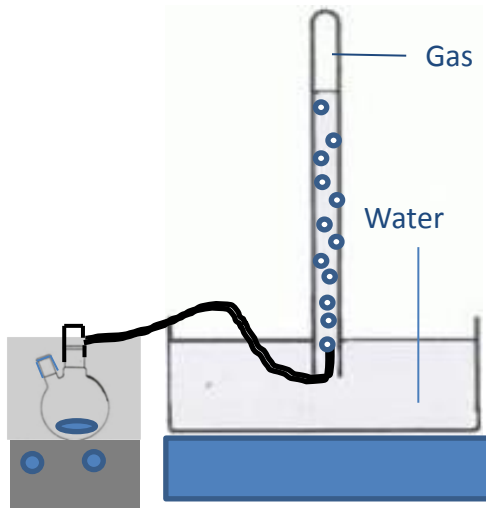


Figure 2-1. Schematic of the gas collection system. A neck of the flask is connected with the gas collecting system, which is immersed in water. The other two necks (even if in the figure there are only 2 shown) are closed up after the reactants were inserted in the flask. Lastly the water can wash the product.

In our experimental work we could not find evidence for the release of diborane ( $\text{B}_2\text{H}_6$ ) from the reaction mixture. It was therefore assumed that only molecular hydrogen was released as a gas from the reaction.<sup>81</sup>

The flask and the stirrer dimensions were carefully chosen to ensure efficient milling on the spherical wall of the glass vessel. After the powders were placed into the vessel, two necks were sealed with rubber septa and a third one was connected to a home-made water-filled Torricellian barometer to observe the expected H<sub>2</sub> gas evolution.

Anhydrous pentane or tetrahydrofuran was added to the flask as a dispersing medium in the early syntheses. Neither of these solvents is able to dissolve reactants or products.

The latter syntheses were performed without any organic dispersing medium, since the instrumental analyses performed on the products, prepared in presence or absence of a dispersing medium, did not show any appreciable difference on the structure and composition. However, Molvinger et al. reported a similar synthesis of nickel borides, under wet conditions and in non-aqueous media.<sup>77</sup> The composition of the products was determined to be one mole of nickel for two moles of boron, in agreement with the foreseen composition of our products.

Furthermore, the presence of organic residues could have altered the composition of the compounds, and therefore the instrumental results. The powders were mixed with the magnetic stirrer set at high speed and allowed to react for approximately 1 to 2 minutes, except for the reaction that contained 10 mol-% nickel bromide which never reached completion even after waiting for 10 minutes. During the reaction, the reactants' color gradually changed from initially orange and white into brown, then grey, deep gray, and finally black. Isolation of the reaction products was done by filtration. Removal of residual organic solvent adsorbed on the powders was performed by

washing three times with ethyl ether. Finally, the powders were dried under partial vacuum.

Successive attempts to improve the initial synthesis were performed as follows:

1. Solvent-less reaction
2. A constant value of 5 mol-% of  $\text{NiBr}_2$  was added to a constant value of 10 mmol  $\text{NaBH}_4$ , thus ensuring complete mixing and optimal nickel content.

Reaction products were freed from the matrix through dissolution of the by-product  $\text{NaBr}$  and hydrolysis of excess  $\text{NaBH}_4$  upon water injection.

Isolation of the products was performed through centrifugation on COSTAR spin – X filters, and drying in an oven at  $150^\circ\text{C}$  for several hours.

After hydrolysis and isolation at room temperature the powders were found to be amorphous. They were also found to be insoluble in anhydrous THF and pentane. Therefore, crystallization by reprecipitation methods could not be performed. An attempt to crystallize the material was performed by annealing it at higher temperatures of 500 and  $830^\circ\text{C}$  for 1 and 5 h under argon (99.9% purity) flow. The inert argon atmosphere was maintained throughout the whole annealing cycle starting half an hour before the powders were heated and stopping half an hour after cool-down. Annealing experiments were performed on powders generated from a 5 mol-% starting nickel value only to ensure an optimal nickel and boron mixing. In fact, 7.5 mol-% was not always mixing properly, and no reasons were found for this behavior and the 10 mol-% was not completely mixing at all under the condition provided.

In order to increase the catalyst surface area,  $\text{SiO}_2$  was chosen as a solid support for the catalyst since it is a cheap and inert oxide and also because it is used extensively in the literature to increase the surface area of many catalysts.<sup>32,37,41,45</sup> For

example, Acosta et al reported that the *in situ* prepared Ni<sub>3</sub>B:SiO<sub>2</sub> supported catalyst presented a surface area of 243 m<sup>2</sup>g<sup>-1</sup>.<sup>32</sup> To prepare supported nickel borides we used SiO<sub>2</sub> gel according to the following procedure. The silica was introduced to the reaction mixture just before adding the water used to perform the hydrolysis of the sodium borohydride matrix. The system was maintained under high speed stirring until the hydrogen evolution ceased.

Reaction products were characterized using several techniques in order to determine the composition and structure: FT-IR; XRD, both in-house and at the Advanced Photon Source (APS) at Argonne National Laboratory, Argonne/IL, using the beamline 11-BM; TGA/DSC up to 1300 K, XPS, TEM and EDXS, SEM and EDS. The experimental studies were augmented by DFT calculations performed by Dr. Caputo initially at the EMPA in Dübendorf, Switzerland and later at the ETH in Zürich, Switzerland.

## 2.2 Theoretical calculations

DFT calculations were performed with two goals in mind: 1) to simulate and optimize chemical structures of nickel borides for which no crystal structures had been observed before which was necessary to compare to the observed XRD spectra, and 2) to obtain their phonon dispersion curves allowing the simulation of IR spectra. Moreover, all possible nickel-rich structures such as Ni<sub>3</sub>B, Ni<sub>2</sub>B, and NiB were both calculated and compared with experimental results from literature to validate the calculations results, i.e. compare output from the calculations with data that were already published, analyze theoretical results and quantify discrepancies between the experimental and theoretical data and operate the same routine to the NiB<sub>3</sub> system.<sup>55,56,60,62-64,74</sup> Calculated structures of boron-rich nickel borides could not be

found in the literature. Our efforts initially focused on NiB<sub>3</sub> which was chosen due to analogies with the NiAl<sub>3</sub> orthorhombic (*Pnma*) system.<sup>72,82,83</sup>

To reduce the number of possible structures that needed to be calculated we eliminated all ternary alloys (Ni, B, H), and binary alloys (Ni, H), (B, H), (Na, H) that may form under normal laboratory conditions due to lack of our experimental evidence.<sup>81</sup>

The monoclinic *P2<sub>1</sub>/c* and *P2<sub>1</sub>* structures and the orthorhombic structure lattices together with their lattice occupancies are presented in Table 2-1.

Table 2-1. Atom site occupancies for the monoclinic and orthorhombic NiB<sub>3</sub> structures. Unpublished data adapted from R. Caputo.

Symmetry group (IT)	Atom	Site	X	Y	Z
P <sub>2</sub> 1 (4)	B	2a	-0.0653	0.38209	0.52914
	B	2a	0.49335	-0.39058	-0.02945
	B	2a	0.00001	-0.39277	-0.02640
	B	2a	0.50012	0.39282	0.52586
	B	2a	0.25305	1.04467	0.28198
	B	2a	0.75306	-1.04456	0.21859
	Ni	2a	0.23277	0.36304	1.18258
	Ni	2a	0.73259	-0.36291	-0.68301
P <sub>2</sub> 1/c (14)	B	4e	0.01507	0.35889	0.27825
	B	4e	0.48615	-0.35826	-0.27832
	B	4e	0.25207	0.99896	-0.00710
	Ni	4e	0.27828	0.39252	0.86432
P <sub>2</sub> 12 <sub>1</sub> 2 <sub>1</sub> (19)	B	4a	0.77946	-0.00796	0.63670
	B	4a	0.22308	-0.00201	-0.13936
	B	4a	0.53285	0.25482	1.29271
	Ni	4a	1.42661	0.23363	0.61774
<i>Pnma</i> (62)	B	8d	0.27770	-0.00329	0.39111
	B	4c	0.03208	0.25000	1.04450
	Ni	4c	0.93060	0.25000	0.36382

The calculations showed a minimum–energy structure with monoclinic symmetry *P2<sub>1</sub>/c*. Calculations of lattice molar enthalpies revealed it to be the most stable of the

calculated structures. Other geometries were also calculated: a monoclinic  $P2_1$  and two orthorhombic structures with space groups  $P2_12_12_1$  and  $Pnma$ .

The main difference between these structures relies on the out-of-plane and in-plane bonding of the boron atoms, respectively. Moreover, the orthorhombic  $Pnma$  space group shows slight analogies with the  $\text{NiAl}_3$  alloy of the same symmetry.<sup>72,82,83</sup> In this structure, the boron atoms arrange to form contiguous heptagons in which the central atom is shifted out of the plane (Figure 2-2 a and b).

The calculated orthorhombic structures are very similar to each other. The  $Pnma$  space group showed the lowest calculated enthalpy making it the most stable one. However, the  $P2_12_12_1$  symmetry is only 1.32 meV per formula unit higher in energy and the calculated lattice constants differed by less than 1 mÅ which was the convergence limit of the calculation.

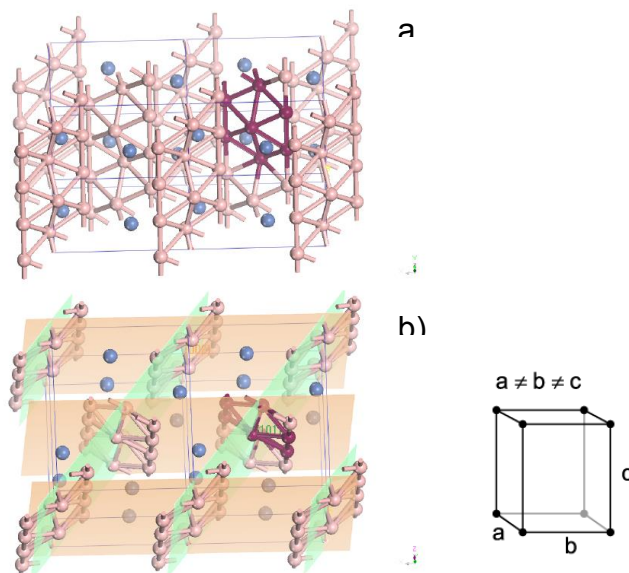


Figure 2-2.  $Pnma$  crystal structure of  $\text{NiB}_3$  a) one of the boron clusters is depicted in violet, the nickel atoms in blue, and the other boron clusters in pink; b) structure with the Bragg planes. Inset: simple orthorhombic unit cell from <http://it.wikipedia.org/wiki/File:Orthorhombic.png>

Differences between the monoclinic structures are more dramatic. In fact, the two more stable structures,  $P2_1/c$  and  $P2_1$ , differ slightly in their angle  $\beta$ . With a small deviation from orthogonality, we obtain  $P2_1$ . When the deviation is slightly larger the more stable  $P2_1/c$  appears. Since the structures are very similar only the most stable of them,  $P2_1/c$ , will be shown (Figure 2-3 a and b).

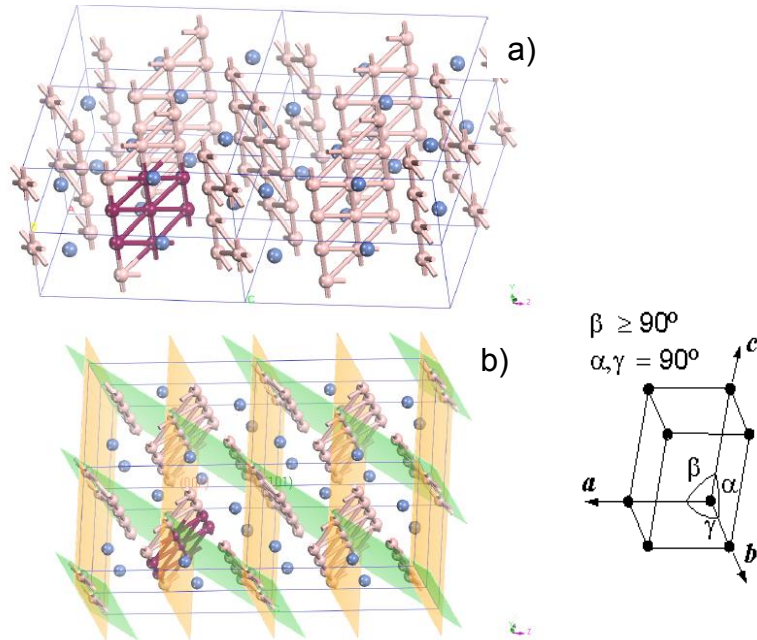


Figure 2-3.  $P2_1/c$  monoclinic crystal structure of  $NiB_3$ . a) one of the boron clusters is colored in violet, nickel atoms in blue, and the other boron clusters in pink; b) Structure with Bragg planes are reported. Inset: simple monoclinic unit cell from: <http://it.wikipedia.org/wiki/File:Monoclinic.png>

The difference between the two monoclinic systems is about 1.86 eV per formula unit. This energy difference is too high to allow for the simultaneous presence of both under normal laboratory conditions. Therefore, we assume that only the most stable form can be found in the powders (i.e. monoclinic ( $P2_1/c$ ) without the entropic contribution or orthorhombic ( $Pnma$ ) with the entropic contribution). The  $\beta$  angle differs from orthogonality only by 2.42 degrees. This small difference is enough to allow the central boron atom to place in or out-of-plane along the  $\vec{a}$  axis. This small change distinguishes

these two monoclinic systems from each other. The comparison between the most stable monoclinic ( $P2_1/c$ ) and the most stable orthorhombic structures ( $Pnma$ ) and the explanation on the existence of one or the other is explained later in Paragraph 2.2. The structural data of the calculated geometries of  $NiB_3$  are reported in Table 2-1 and 2-2, for both orthorhombic and monoclinic systems (IT stands for the “International Tables for Crystallography”).

Heats of formation and unit cell dimensions (lattice constants and angles) are also calculated and are presented in Table 2-2.

Table 2-2. Calculated Thermodynamic and Structural Data of the Compounds.

Compound	a(Å)	b(Å)	c(Å)	$\alpha(^{\circ})$	$\beta(^{\circ})$	$\gamma(^{\circ})$	Symmetry group(IT)	$\Delta_f \bar{H}_0$ (KJ/mol)
NaBH <sub>4</sub>	4.359	4.359	5.909	90.00	90.00	90.00	$P\bar{4}2_1/c$ (114)	-251.817
NiB	3.086	7.512	2.992	90.00	90.00	90.00	$Cmcm$ (63)	-32.873
Ni <sub>2</sub> B	5.101	5.101	4.402	90.00	90.00	90.00	$I4/mcm$ (140)	-59.168
Ni <sub>3</sub> B	5.270	6.905	4.559	90.00	90.00	90.00	$Pnma$ (62)	-87.284
NiB <sub>3</sub>	3.038	8.220	5.212	90.00	87.57	90.00	$P2_1/c$ (14)	-133.995
NiB <sub>3</sub>	5.964	3.275	7.226	90.00	90.00	90.00	$Pnma$ (62)	+46.156

The space groups for the various structures given in the Table 2-2 are the most stable for the given compounds. The calculated values can be compared with published reports.<sup>55,56,60,62-64,74</sup> An enthalpic correction factor must be calculated to account for the difference in temperature between synthetic conditions (normal laboratory conditions) and calculations (0 K).

$$H(T) = H(0) + \int_0^T C_p dT \quad (2-3)$$

The most stable monoclinic and orthorhombic structures differ in the displacement of just one atom. However this small difference in structure causes a big difference in the calculated heats of formation. For the orthorhombic  $Pnma$  space group, the heat of

formation is +46.156 KJ/mol, at  $P = 0$  atm and  $T = 0$  K. Therefore, its formation is possible only if driven by an entropic contribution.

To determine the entropic contribution to the lattice stability we calculated the entropies of the two lattices to temperatures up to 1000 K, using the standard definition:

$$S(T) = \int_0^T \frac{C_p}{T} dT \quad (2-4)$$

The Gibbs free energy of the orthorhombic ( $Pnma$ ) structure yielded slightly more negative results than the corresponding value of the monoclinic ( $P2_1/c$ ) structure while increasing the temperature, indicating that temperature and entropy substantially contribute to the stabilization of the orthorhombic structure. To validate the calculation on the boron-rich  $NiB_3$  structures, the known nickel boride  $NiB$  structure was chosen. Since  $NiB$  structure has already been published, experimental values on heats of formation and on the entropic contribution, as well as the phase diagram of the  $NiB$  can be found.<sup>74,84</sup> These experimental data can be used as benchmark with our theoretical calculations. The validation of the method comes from the agreement between calculated and experimental values. Once the method is validated, we are sure that our calculations on the boron-rich phases  $NiB_3$  are accurate, and therefore, if experimentally found, these theoretical data can be used to compare experimental findings.

The comparison between the monoclinic ( $P2_1/c$ ) and orthorhombic ( $Pnma$ ) structures is shown in Table 2-3. The Table 2-3 lists the total electronic energy  $E$ , the zero-point energy  $E_{ZP}$  and the enthalpic and entropic contributions to the Gibbs energy. The lattice contribution to  $C_p$  is calculated by numerical integration over the wavenumbers of the phonon dispersion curve.

Table 2-3. Calculated energies, zero point energies and entropic contributions of the o - NiB and the o – and m – NiB<sub>3</sub>.  $E_{ZP}$  and the enthalpic and entropic contributions are in kJ/mol. Adapted from Caputo et al., unpublished results.

Specie	$E_{ZP}$ (KJ/mol)	H(T=298 K)	H(T=1000 K)	S(T=298 K)	S(T=1000 K)
o-NiB	18.909	2.478	20.033	$14.105 \cdot 10^{-3}$	$42.923 \cdot 10^{-3}$
o-NiB <sub>3</sub>	33.832	8.520	63.071	$48.299 \cdot 10^{-3}$	$139.004 \cdot 10^{-3}$
m-NiB <sub>3</sub>	45.003	8.206	64.070	$46.751 \cdot 10^{-3}$	$138.829 \cdot 10^{-3}$

The calculated data are useful to predict the stability of the most probable boron-rich phase and are used to compare the predicted XRD and IR spectra with our experimental findings and literature data.<sup>55,56,60,62-64,74</sup>

## 2.3 Experimental Characterization

### 2.3.1 Density

The density of solids is easy to calculate and to verify experimentally. We obtained calculated values for the densities of the most stable lattices of known compounds (NiB, Ni<sub>2</sub>B, and Ni<sub>3</sub>B) and both theoretical orthorhombic (IT 62) and monoclinic (IT 14) NiB<sub>3</sub>. These values were compared with the experimentally determined density of NiB<sub>x</sub>. All of these findings are reported in Table 2-4.

Experimentally, we determined the density of our solids using Archimede's method by the displacement of water.<sup>85</sup>

The calculated densities for NiB<sub>3</sub> are very close to the experimental ones while the other nickel-rich phases show values which are too high. The differences between the calculated orthorhombic and monoclinic NiB<sub>3</sub> values and the experimental value are 0.17 and 0.33 g/cm<sup>3</sup>, respectively.

All nickel-rich phases show values which are higher by more than 2 g/cm<sup>3</sup> when compared to the experimental number.

Table 2-4. Calculated molecular weights, molar volumes and for different nickel borides. Note that all the densities are calculated. The last row shows the experimental result. Caputo et al., unpublished results.

Species	Molar wt (g/mol)	Molar Vol (cm <sup>3</sup> /mol)	Mass density (g/cm <sup>3</sup> )
NiB	69.5	10.44	6.66
Ni <sub>2</sub> B	129.2	17.26	7.43
Ni <sub>3</sub> B	186.9	24.98	7.48
NiB <sub>3</sub>	91.13	20.29	4.49
NiB <sub>3</sub>	91.13	19.59	4.65
NiB <sub>x</sub>	n/a	n/a	4.82

### 2.3.2 Thermal Analysis

Thermal analysis is a common characterization technique for solid materials. It can be performed with a wide range of techniques. Generally, the results show how the solid sample behaves upon annealing. The principal techniques used are TGA (thermogravimetric analysis) and DSC (differential scanning calorimetry) or DTA (differential thermal analysis). TGA determines the loss of mass from the solid, with the increase in temperature of annealing. This data is determined in wt-%. The samples generally lose weight because small volatile molecules escape into the gas phase at specific temperatures, *e.g.*, water (even crystallization waters) or CO<sub>2</sub> (from organic compounds).

DSC is useful in the determination of phase transitions of the solids including molecular rearrangement, re-crystallization, and glass transitions. This technique needs an internal reference, the heat capacity of which is known. Heat capacity differences between the reference and the sample under study are measured as a function of temperature.

The experimental set-up for DTA analysis is very similar to that for DSC.<sup>86</sup>

Experimental data are normally reported as  $\frac{\partial H}{\partial T}$ . The area under the peak of a DTA

thermogram represents the  $\Delta H$  for a particular transition.<sup>87</sup> Reporting experimental DSC data in derivative form is generally accepted because it helps in determining the heats of crystallization or the  $\Delta H$  of the transition.<sup>39</sup>

Interpretation of the data obtained through thermal analyses alone is not straightforward without prior knowledge about the material or the availability of reference data to similar related compounds. However, these experiments are extremely important because they show at which temperatures certain transformations occur. Thermal analyses, furthermore, can reveal if a particular transition is exothermic or endothermic, which can be seen by the sign of the DSC or DTA peak.

The following describes experimental thermal analysis of our NiB<sub>x</sub> samples.

NiB<sub>x</sub> is insoluble in water or any other organic solvent (anhydrous THF and pentane) and therefore cannot be crystallized by re-precipitation methods. Thermal analysis can detect physical changes and structural rearrangements upon annealing of the solid compound, if they fall in the range of temperatures surveyed by the instrument.

Thermal analysis was performed using a TA SDT Q600, dual DSC and TGA, Version 20.5, Build 15 from the series instrument (courtesy of Dr. Miller at the Dept. of Chemistry, University of Florida).

This instrument allowed us to simultaneously perform both DSC and TGA experiments in which the instrument is equipped with a microbalance and a furnace that ramps up to 1300°C. DSC curves are referenced to dry (99.9%) N<sub>2</sub> gas. The results are presented in Figures 2-4, 2-5, and 2-6, in differential form,  $\frac{\partial H}{\partial T}$  for easier comparison with literature data.<sup>39</sup>

The thermograms (Figures 2-4, 2-5, and 2-6, and see end Paragraph 2.3.2) show two regions of interest: The DSC profile shows a broad transition (around 650 K) and another one around 1100 K. Other features are also visible, but due to the small change in energy these features are difficult to interpret or analyze experimentally. Water loss is shown at 323 K or slightly below or above, depending on the system under study. Analogous results were found for 1:10 (wt) silica-supported powders. Both  $\text{NiB}_x$  thermograms were compared to silica alone, to understand the thermal effect(s) of supporting the  $\text{NiB}_x$  material.

The thermogram of silica gel alone (Figure 2-5) shows only a few regions of interest. Feature #1 is common to all thermograms and is clearly due to water loss somewhere around 323 – 373 K. Feature #3 is a slow transformation over a wide range of temperatures between 800 and 1200 K. The basis for this transformation is not clear. Undoubtedly, this thermal behavior reflects a change in the supported powders. Feature #2, a broad peak seen around 650 K in the unsupported powders in fig. 2-4, appears shifted to higher temperatures (around 900 K) in the silica-supported material. In a similar way feature #3 around 1000 K in Figure 2-4 is shifted to somewhat higher temperature (around 1100 K) as well. Additional features in the supported materials appear at 650 and 1150 K. They are not seen in the unsupported catalyst either because they may be hidden by other features there, or simply don't exist. They are difficult to interpret because of the limited intensity (energy change) at various temperatures which are closer to each other, and therefore they change accordingly to the temperature chosen.

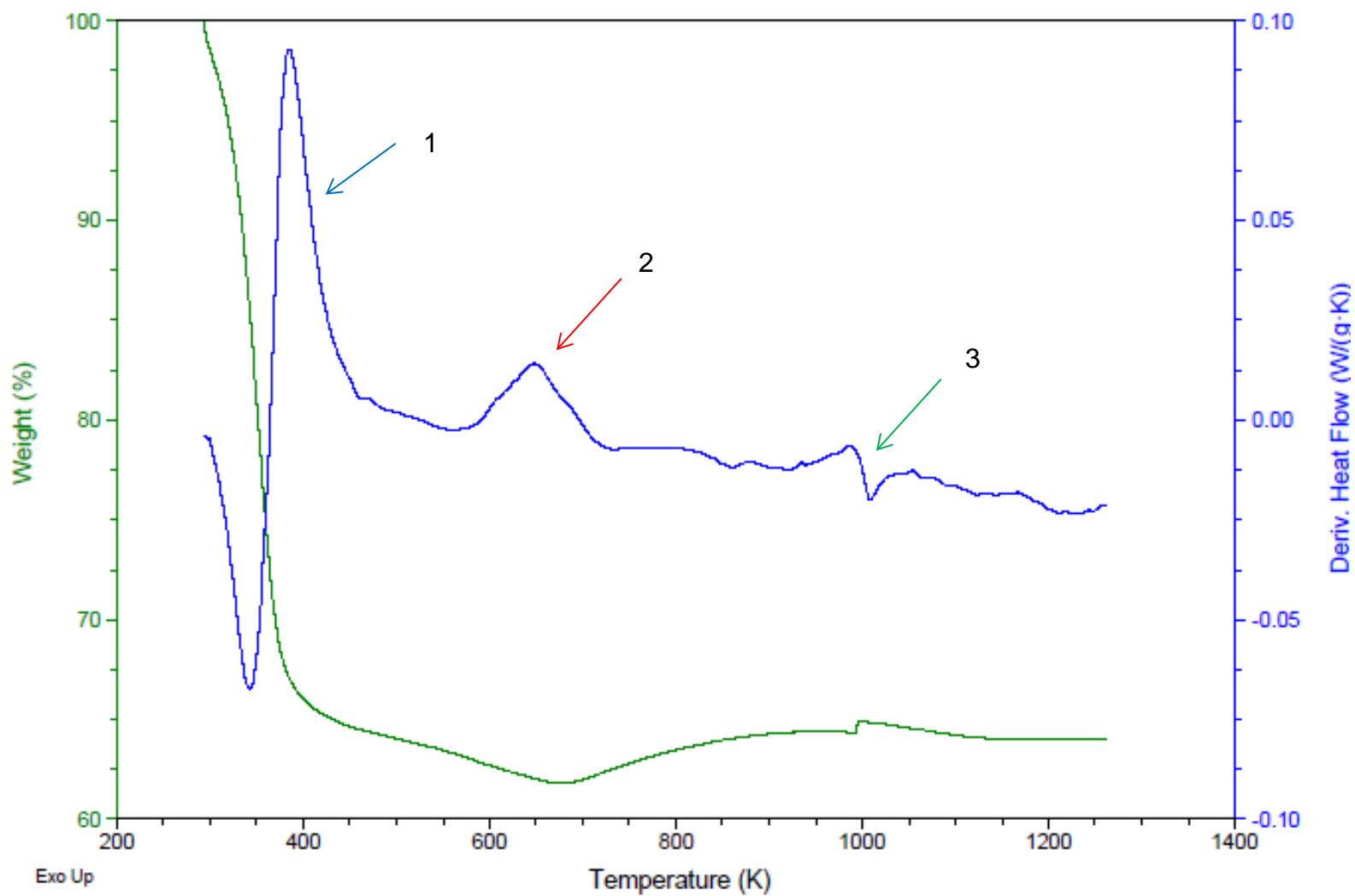


Figure 2-4. TGA/DSC graph of the 5 mol-% Nickel Bromide in NaBH<sub>4</sub> after hydrolysis 1) Water loss; 2) the broad peak position and 3) unexplained feature

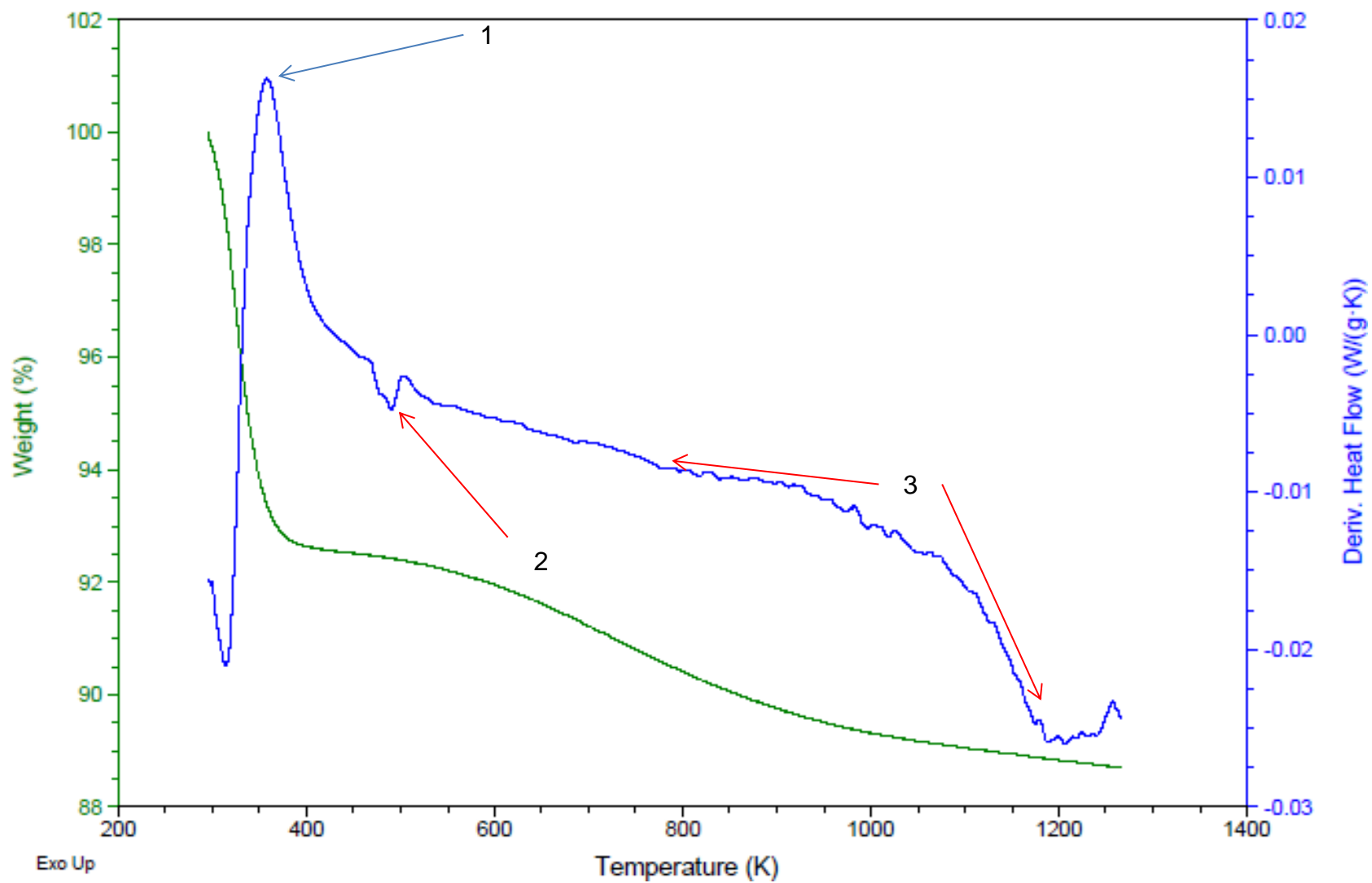


Figure 2-5. SiO<sub>2</sub> gel thermogram: 1) water loss peak. 2) and 3) unassigned transformation(s).

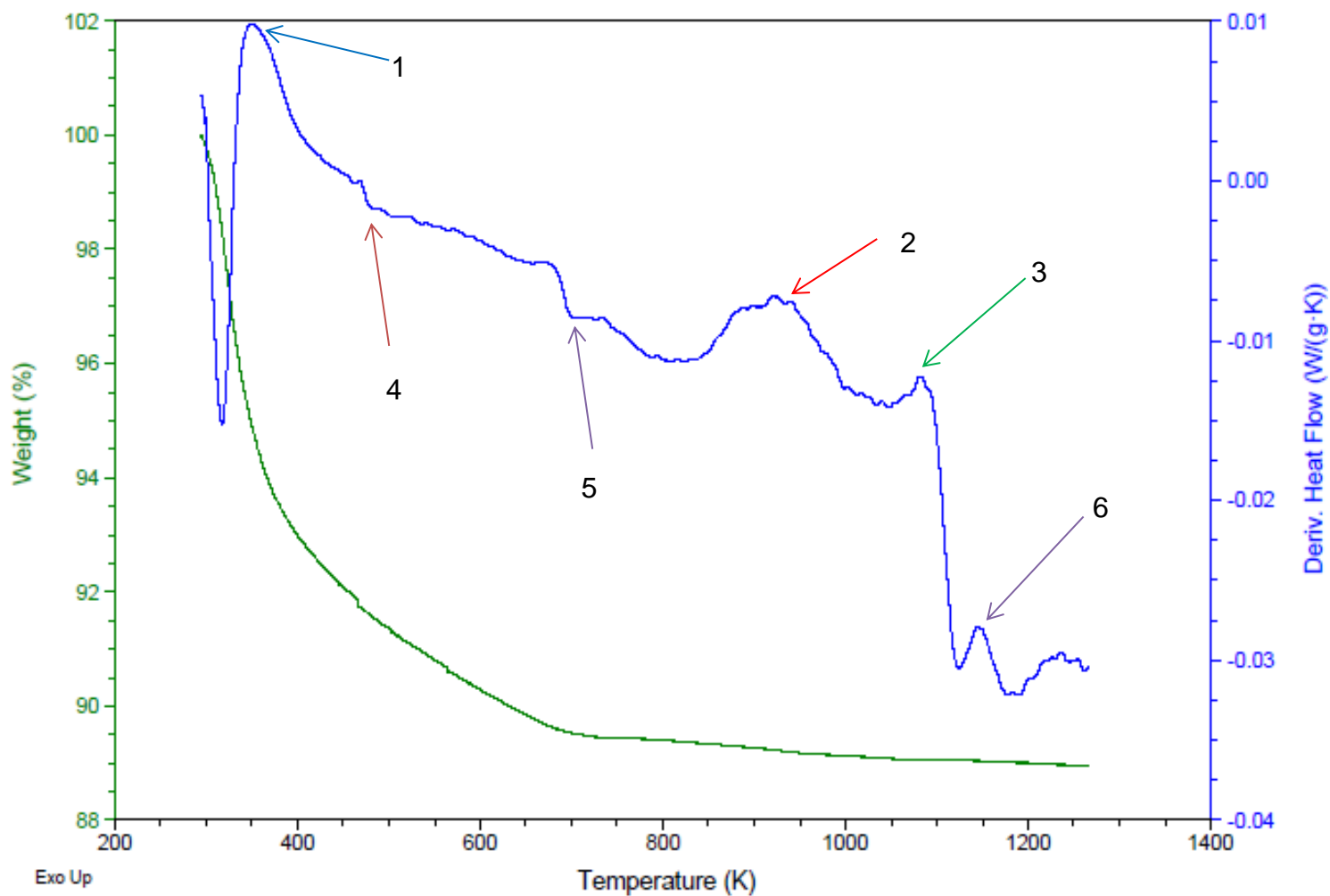


Figure 2-6. NiB<sub>x</sub>:SiO<sub>2</sub> (1:10 wt) supported catalyst thermogram. 1) Water loss; 2) the broad peak is found above 800 K; 3) the rearrangement at 1100 K shows larger energy variation; 4) very weak feature due to SiO<sub>2</sub> (compare with figure 2-6); 5) and 6) unassigned transformations.

No literature data were found for those transitions in all documents studied. For those reasons, therefore, only the main features will be further considered.

Experimental DSC results have been described in the literature<sup>39</sup> and will be compared and their relevance to our results discussed in the discussion section.

### 2.3.3 FTIR

Infra-red radiation is used to probe vibrational frequencies in molecules. Different regions of the spectrum will show characteristic vibrations that can be considered fingerprints for a compound (for example B-B stretch frequencies).

Since there are no experimental IR spectra for NiB<sub>3</sub> with which to compare our experimental spectra, we turned to calculated spectra as the only possibility to give some indication where these vibrations might appear in the spectrum. For NiB<sub>3</sub> they are expected at 1265 cm<sup>-1</sup> (B<sub>1u</sub>), and 1296 cm<sup>-1</sup> (B<sub>3u</sub>). In the far-IR region, a strong absorption is calculated near 230 cm<sup>-1</sup>. Figure 2-7 shows the calculated IR for both the monoclinic (*P2<sub>1</sub>/c*) and the orthorhombic (*Pnma*) NiB<sub>3</sub> structures. Similar calculations are still under way for the predicted NiB<sub>2</sub> structure. Calculated intensities are reported in km/mol, which is commonly used as the unit for the intensity of calculated IR spectra.<sup>88</sup>

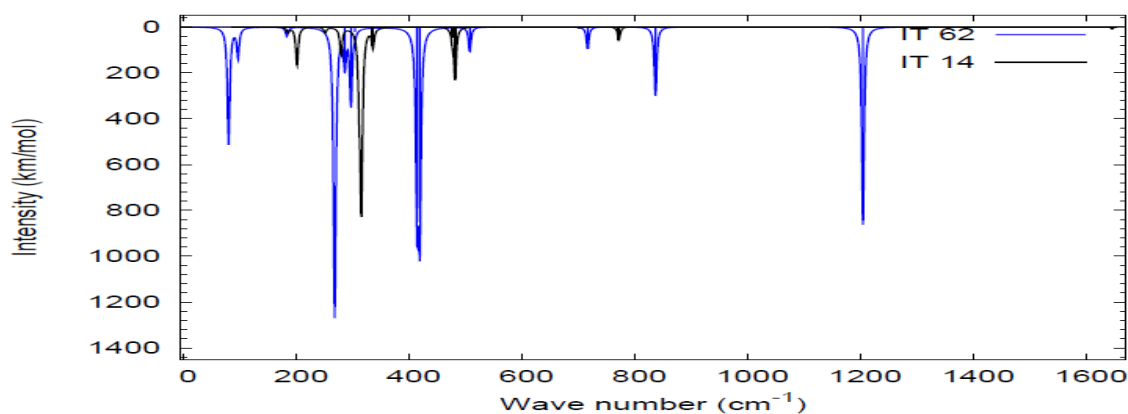


Figure 2-7. Calculated FT-IR spectra of the most stable NiB<sub>3</sub> structures. In blue the orthorhombic *Pnma* structure, in black the *P2<sub>1</sub>/c* structure.

In our study we used the mid-IR range between 4000 and 800  $\text{cm}^{-1}$ .

Raman and FT-Raman spectra were attempted but couldn't be collected because of the strong absorption of the laser light by the sample.

Experimental FT-IR was performed in the solid state using KBr pellets as the matrix with a Bruker Vertex v80 spectrometer, courtesy of Dr. Murray at the Dept. of Chemistry, University of Florida.

Our data are presented after subtraction of the background (KBr) and normalization of the peak at 1126  $\text{cm}^{-1}$ , which could be one of the B-H bending vibrations.<sup>89,90</sup> The spectra of the unhydrolyzed powders with varying nickel content are shown in figure 2-8 and are compared to those of pure reactants, sodium borohydride and the matrix, potassium bromide. In all cases, residual B-H stretches visible by the triplet around 2300  $\text{cm}^{-1}$  and the B-H bends at 1126  $\text{cm}^{-1}$ .<sup>89,90</sup>

Figure 2-8 mainly shows the spectra of sodium borohydride. This is not unexpected since this reactant will remain in the reacted powders to some extent. However, additional bands appear in the region below 1000  $\text{cm}^{-1}$  and between 1300 and 1800  $\text{cm}^{-1}$  and must be due to the reaction products. The intensity of all of these peaks does not seem to be related to the amount of nickel used in the reaction indicating that other reaction products, perhaps nickel borides with different compositions, may have appeared as well and are masking the expected effect. The region between 1300 and 1875  $\text{cm}^{-1}$  shows several broad bands that are difficult to interpret. The B-H stretch region between 2200 and 2350  $\text{cm}^{-1}$  seems to show another vibration around 2325  $\text{cm}^{-1}$  which becomes more resolved with increasing nickel content.

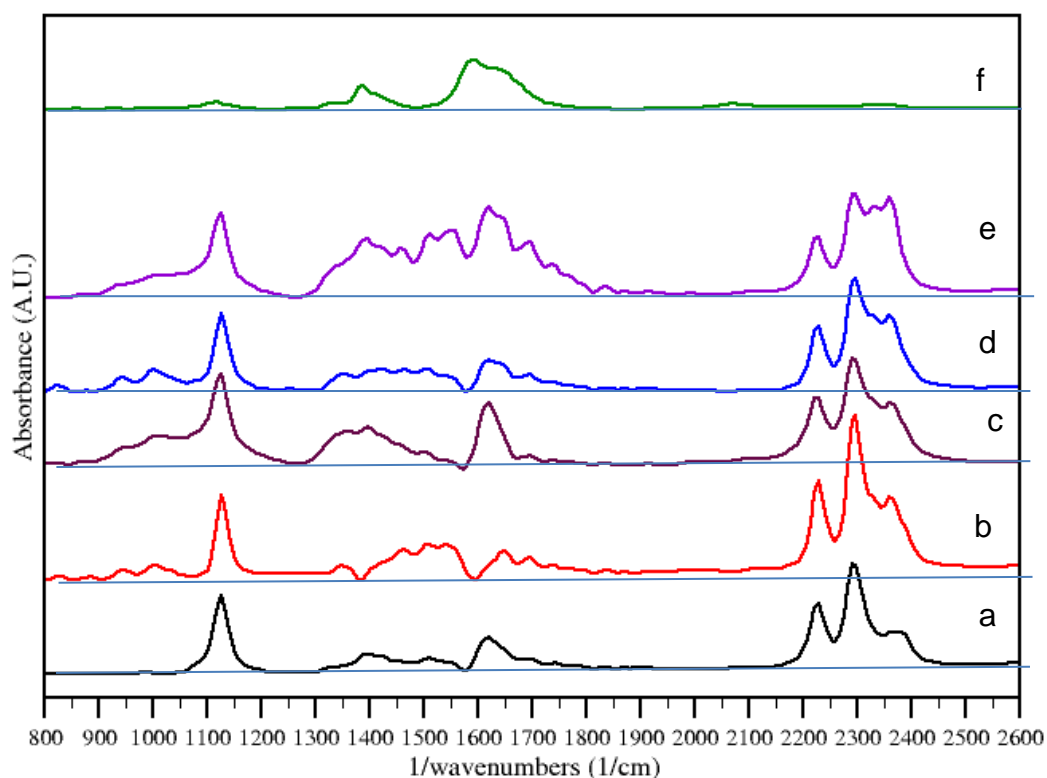


Figure 2-8. FT-IR spectra of the non-hydrolyzed powders. a: Sodium borohydride; b: the 2.5 mol-% Ni containing powder. c: the 5 mol-% Ni containing powder; d: the 7.5 mol-% Ni containing powder; e: the 10 mol-% Ni containing powder; f: the KBr spectrum.

FTIR in the mid-IR range was also performed on the annealed powders, and compared to the spectrum of  $\text{MgB}_2$  to determine boron vibrations.

Magnesium diboride crystallizes in a hcp lattice, with the  $P6/mmm$  space group. The IR spectrum of  $\text{MgB}_2$  has been reported by Sundar et al and is reproduced in Figure 2-10.<sup>91</sup>

In the mid-IR  $\text{MgB}_2$  shows two broad but weak absorption bands at 1442 and 1635  $\text{cm}^{-1}$ . The strong and broad peak at 1040  $\text{cm}^{-1}$  is most probably due to unreacted crystalline boron, as reported by Sundar et al.<sup>91</sup> In their work they prepared fresh  $\text{MgB}_2$

using both crystalline and amorphous boron and magnesium, and characterized it by FT-IR (both far-IR and mid-IR).

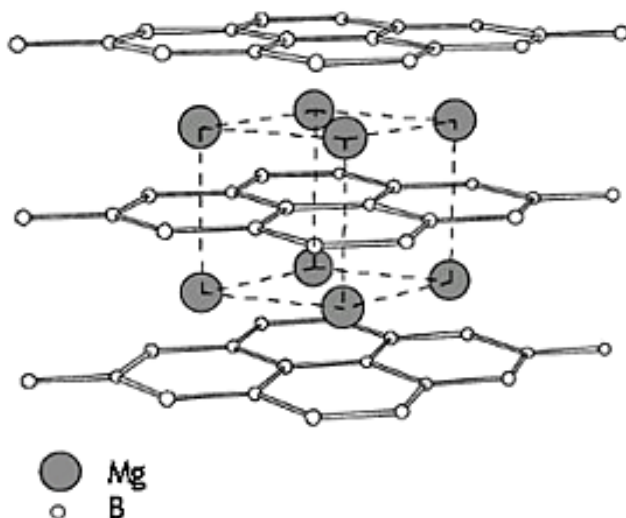


Figure 2-9. MgB<sub>2</sub> crystal structure.<sup>92,93</sup> Dashed lines show the cubic structure of Mg. Figure reprinted from <http://www.magnet.fsu.edu/magnettechnology/research/asc/research/mgb2.html> retrieved 2/9/2012 @ 20:41

In their work they prepared fresh MgB<sub>2</sub> using both crystalline and amorphous boron and magnesium, and characterized it by FT-IR (both far-IR and mid-IR). In Figure 2-10 are shown their FT-IR spectra, in the mid-IR, of amorphous and crystalline boron, and the product of the synthesis, which was clearly affected by the presence of unreacted crystalline boron. This result, can be easily seen by the presence of a broad peak around 1040 cm<sup>-1</sup> in the spectra of the products and in crystalline boron and which is absent in the spectrum of amorphous boron.

Figure 2-11 shows the IR spectra of the annealed powders and the magnesium boride. The spectra of the annealed powders seem to show the same vibrational frequencies as MgB<sub>2</sub>.

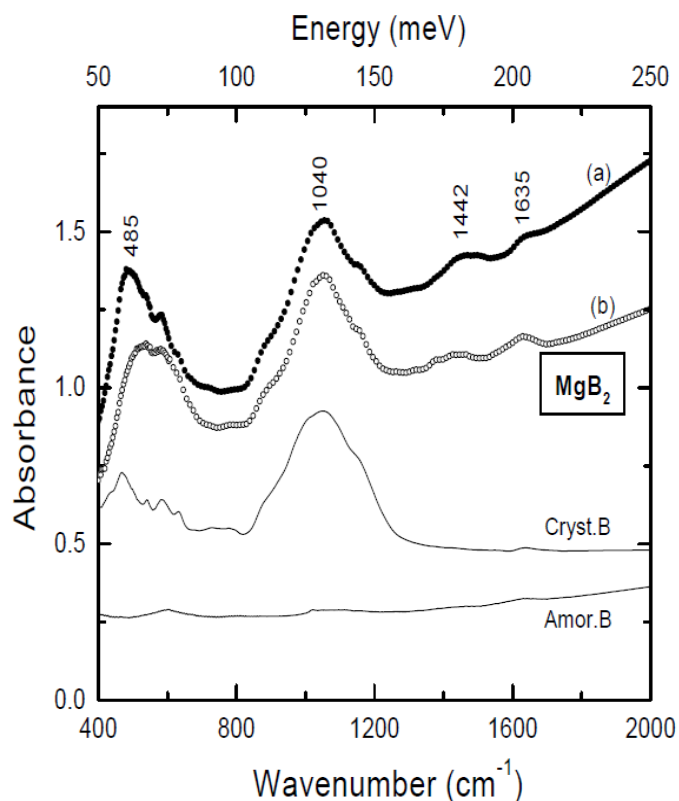


Figure 2-10. IR spectra of  $\text{MgB}_2$ . Adapted from Sundar, C.<sup>91</sup> (a) is the experimental spectrum of  $\text{MgB}_2$  produced by the authors, (b) is the spectrum obtained from commercial  $\text{MgB}_2$ , Cryst. B is the spectrum of crystalline boron and Amor. B is the one obtained from amorphous boron

This may be due to a structural arrangement of the boron atoms in nickel borides which recall the structure of  $\text{MgB}_2$ . Overall the spectra show the same behavior, and it is also similar to the spectrum of  $\text{MgB}_2$ .

The spectra all look very similar presumably because the background subtraction was insufficient and the main contribution in all of them are  $\text{SO}_4^{2-}$  impurities in the KBr pellet.<sup>94</sup>

However, small differences can be found when analyzing the spectra. The effect of supporting the powder onto silica was also studied by FTIR spectroscopy. This

experiment had the aim of determining vibrations frequencies of each of the components in the supported powders.

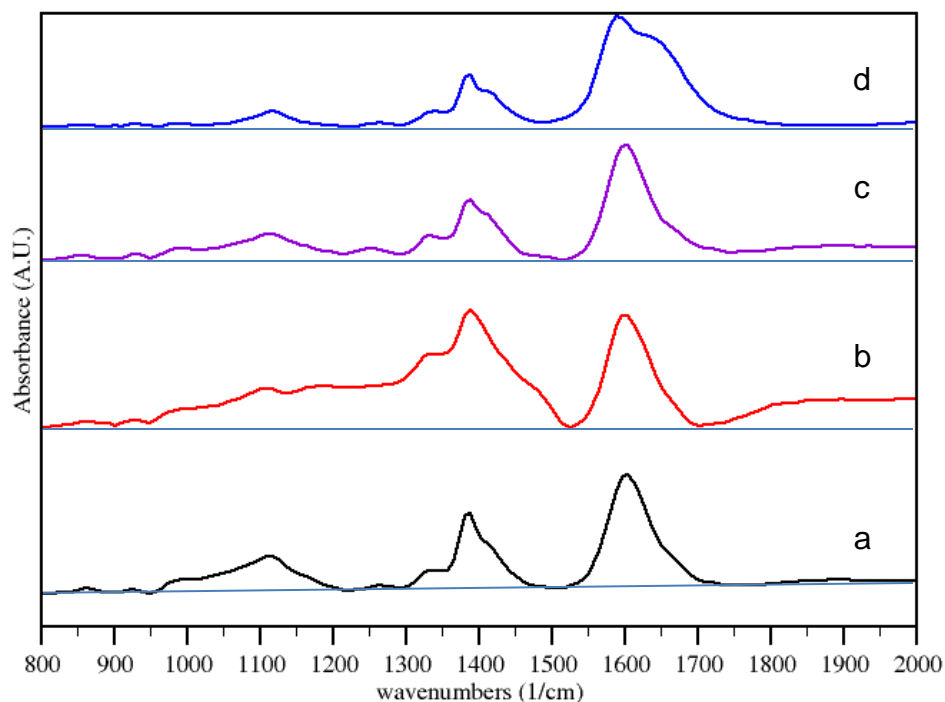


Figure 2-11. FTIR spectra : a)  $\text{MgB}_2$ , b) the powder annealed 5 h at  $500^\circ\text{C}$ , c) the powder annealed 5 h at  $830^\circ\text{C}$ , d) KBr.

The spectra are presented in Figure 2-12.

The spectra show the same vibrations overall. Very few pronounced differences can be found when comparing both spectra. The broad peak at  $1100\text{ cm}^{-1}$  in the spectrum of the silica gel, due to Si-O stretching, is slightly shifted after interaction of the powder. The peak is also attenuated in the latter case and it is broadened, as it can be inferred by the FWHM (full width half maximum). This peak presents a shoulder around  $1080\text{ cm}^{-1}$  ( $\text{SiO}_2$  spectrum, black line) which is not found in the spectrum of the supported  $\text{NiB}_x$ . The silica spectrum, furthermore, shows a weak peak in the low end of the spectrum ( $800\text{ cm}^{-1}$ ), which is not revealed by the supported  $\text{NiB}_x$  spectrum.

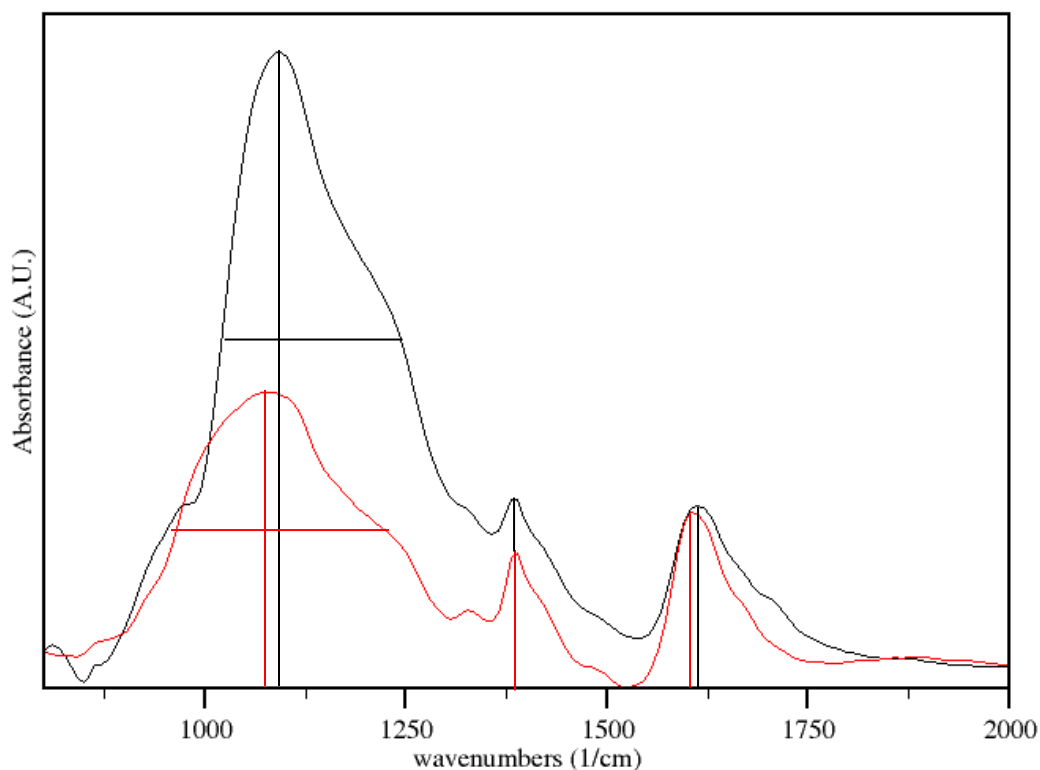


Figure 2-12. FTIR in the mid IR of the commercial SiO<sub>2</sub> gel (in black) and the supported nickel boride (in red). Vertical lines are the peak maxima positions and horizontal lines are FWHM.

The peak at 1620 cm<sup>-1</sup> due to water bending seems broadened in the case of SiO<sub>2</sub>, maybe because of the interaction of the water with the superficial Si-OH groups, which are covered by the NiB<sub>x</sub> powder after the reaction. It is also slightly shifted in the latter case, as compared with the spectrum of the SiO<sub>2</sub> alone. However the vibrations from NiB<sub>x</sub> are not seen due to the impurities found in the KBr, which show predominantly in the spectra. The lack of peculiar vibrations from the NiB<sub>x</sub> powder can either be attributed to very little powder ending up in the pellet or to very weak vibrations which are covered by the stronger vibrations.

FTIR on annealed supported powders was not performed, since after annealing (under argon) clear phase separation was observed.

### 2.3.4 Powder XRD

As explained by West,<sup>95</sup> powder XRD diffraction is a powerful technique used on micro-crystalline samples to reveal structural information.

Diffraction techniques rely on the interference between radiation paths transmitted through or reflected from a sample with internal periodic structure such as crystal planes in microscopic crystallites. The Bragg equation relates the reflection angle  $\theta$  to the wavelength of the radiation,  $\lambda$ , and the spacing between crystal planes  $d$

$$2d \sin \theta = n\lambda \quad (2-6)$$

where  $n = 1, 2, \dots$  is the so called diffraction order.

The Bragg theory, which explains the diffraction process in crystals, considers crystal layers or planes as semi-transparent mirrors. Beams are reflected from these planes with an angle of reflection equal to the angle of incidence. Reflection occurs when the path lengths of reflected beams from neighboring planes fulfill the Bragg condition (equation 2-6) which leads to constructive interference (see Figure 2-14).<sup>95</sup>

Two X-ray beams are reflected from consecutive planes (red lines in Figure 2-14), separated by a  $d$  spacing between successive crystal planes. The difference in optical path lengths between beams 1 and 2 are given by the length  $\overline{XYZ}$ . In order for 1' and 2' to be in phase this path length must be an integer multiple of the wavelength. The perpendicular distance between two consecutive planes is called the *d-spacing* (see Figure 2-13).

The angle between the incident beam and the lattice is called the *Bragg angle*,  $\theta$ . The relationship between the path length difference and the Bragg angle as well as the *d-spacing* is given by the trigonometric relationship:

$$XY = YZ = d \sin \theta \quad (2-7)$$

Thus

$$XYZ = 2d \sin \theta \quad (2-8)$$

In order to have constructive interference, the following condition must be satisfied:

$$XYZ = n\lambda \quad (2-9)$$

and consequently,

$$2d \sin \theta = n\lambda \quad (2-10)$$

This condition is required for the reflected beam to be in phase, and to interfere constructively. At angles different than the Bragg angle, the interference is more or less destructive and cancellation of the beam occurs. Complete cancellation happens within a few tenths of a degree of the determined angle due to the large number of planes within the crystal on which the beam is reflected. These *lattice planes* are defined by the crystal symmetry and the lattice parameters of the unit cell. They are parallel throughout the crystal and are labeled using *three numbers* known as *Miller indices* for each set of planes.

Derivation of the Miller indices of the various planes cutting the crystal structure depends on the geometric construction of the unit cell. Taking one edge as the origin of the cell, there will be planes which will pass parallel to one or more faces or obliquely through the unit cell (see Figure 2-14).

In figure 2-14 various Miller planes for cubic structures are shown. In the first figure (top left) the red colored area cuts the x, y and z axis at  $1a$ ,  $\infty b$  and  $1c$ , where  $a$ ,  $b$

and  $c$  are the lattice constants, i.e. the minimal distances between adjacent atoms in a unit cell.

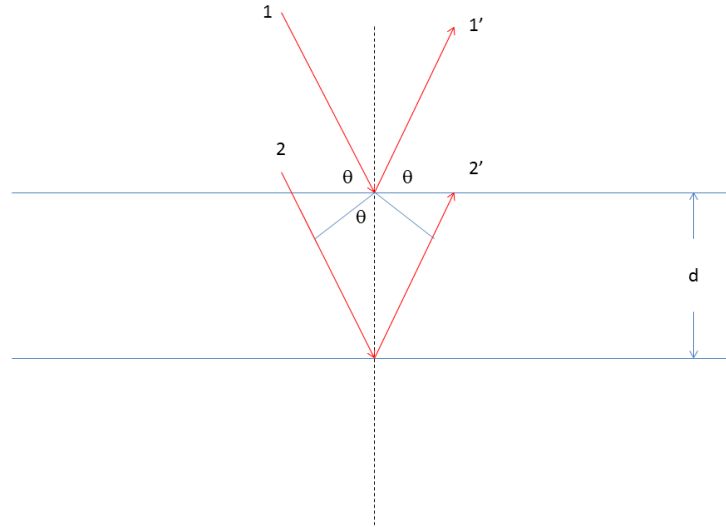


Figure 2-13. Schematic used in the derivation of Bragg's Law for X-ray diffraction.  $d$  represents the distance between neighboring crystal planes. The angle  $\theta$  is the angle of incidence or reflection of the X-ray beam. The path length between beams reflected from neighboring planes is given by  $\overline{XYZ}$ .

To Miller index that plane we need to take the reciprocals of 1,  $\infty$  and 1, i.e. naming it the (101) plane. The Miller index of 0 indicates that the plane will be parallel to a particular axis. Generally the Miller indices are expressed in the order  $x$ ,  $y$ , and  $z$  within parentheses, the so-called  $(hkl)$  formalism. It is used for equivalent sets of planes. Overlined indices indicate that its direction is opposite or negative for the corresponding axis.

The  $d$ -spacing for a given set of  $(hkl)$  planes can be calculated with the following formula:

$$\frac{1}{d^2} = \frac{h^2}{a^2} + \frac{k^2}{b^2} + \frac{l^2}{c^2} \quad (2-11)$$

By definition the unit cell must contain at least one formula unit per compound. In centered cells and in some primitive cells the unit cell can contain more than one formula unit.

Loss of information is inherent to the XRD experiment because a 3D object is projected onto a 1D detector plane. To overcome this issue, the experimental patterns are fitted with known structures through the so called Rietveld refinement.<sup>96</sup>

Rietveld refinement works best for multi-phasic powder patterns, which contain more than one crystal structures.<sup>96</sup>

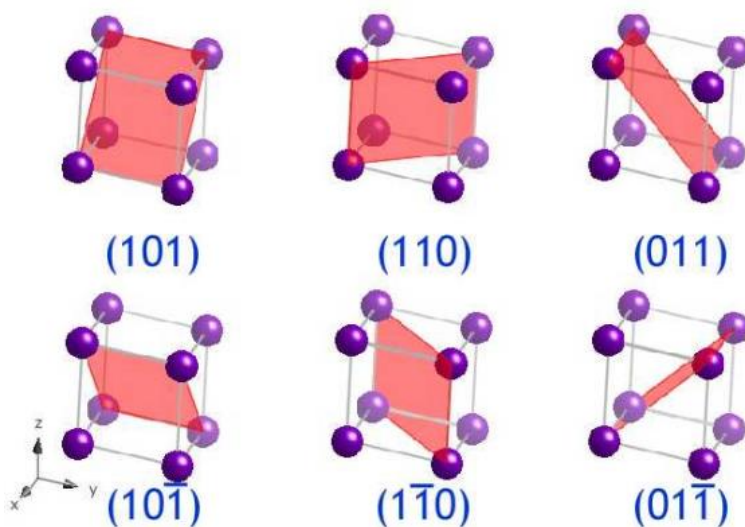


Figure 2-14. Miller planes and indexing in a simple unit cell.

([http://www.doitpoms.ac.uk/tlplib/miller\\_indices/printall.php](http://www.doitpoms.ac.uk/tlplib/miller_indices/printall.php), retrieved 3/5/2012 at 1:09 p.m.)

The process of refinement uses calculated or published structures as a starting point to simulate experimental XRD patterns. Many software programs are downloadable free of charge. For our refinements we used the BRASS software (Bremen Rietveld Analysis Structure Suite).<sup>97</sup> Using Rietveld refinement it is possible to predict a number of useful parameters such as quantitative content of different crystal

phases (from multiphase systems), stress/strain of the crystal structure, and refined lattice parameters for all the structures present in a given sample among others. The refinement utilizes the least squares method of error analysis when comparing the predicted to the experimental XRD spectrum in order to optimize the lattice parameters.

After the refinement step the software graphically plots the background function(s), the identified peaks and phases, the fitted patterns, and the so-called *residuals*. The residual curve gives an indication of the goodness of the fit. It should show a flat line with only experimental noise superimposed in the case of perfect agreement between the predicted and experimental spectrum.

Structural data for a crystalline system is reported as atomic coordinates which can be used to derive bond distances and angles. This information is used in the Rietveld refinement in two ways. It allows to increase the number of geometric “observations” and/or diminishing the number of simulation parameters for the calculation. The set of “observations” is treated as a secondary data-set and the function which is minimized is given by:<sup>98</sup>

$$S = S_y + c_w S_G \quad (2-12)$$

$S_y$  is the weighed difference between the observed and calculated intensities  $[Y_{(calc)}]$  and  $[Y_{(obs)}]$ .<sup>98</sup>

$$S_y = \sum_i w_i \cdot [y_i (obs) - y_i (calc)]^2 \quad (2-13)$$

and represents the error function which is minimized by the software.  $S_G$  is the difference between the observed and calculated geometric constraints, weighted by the parameter  $c_w$ .

$$S_G = \sum w \cdot [G(obs) - G(calc)]^2 \quad (2-14)$$

$c_w$  changes with the improvement of the model. It is usually large at the beginning of the refinement since the initial guess of the model is approximate (bond distances might be too short or too large, angles are too narrow or too wide) and will be reduced while the optimization improves the predicted structure within the given constraints.

The goodness of the fit is determined by the  $\chi^2$  value, which assumes the form of:

$$\chi^2 = \frac{R_{wp}}{R_{exp}} \quad (2-15)$$

where:

$$R_{wp} = \left\{ \frac{\sum_i w_i \cdot [y_{obs} - y_{calc}]^2}{\sum_i w_i \cdot [y_{obs}]^2} \right\}^{1/2} \quad (2-16)$$

is the  $R$  value for the weighted profile and

$$R_{exp} = \left\{ \frac{N - P}{\sum_i^N w_i \cdot [y_{obs}]^2} \right\}^{1/2} \quad (2-17)$$

is the statistically expected  $R$  value, with  $N$  being the number of observations and  $P$  the number of parameters refined.<sup>98</sup>

Ideally, the final  $R_{wp}$  value should be close to  $R_{exp}$  ( $\chi^2 = 1$ ). Experimentally, a  $\chi^2 = 1$  or near one is very difficult to obtain. Generally  $\chi^2$  is greater or smaller than 1. If the data are acquired too quickly, and the parameters for the refinement needed are too many, (this means a very small  $R_{exp}$ ), the  $\chi^2$  value will be much greater than one. On the other hand, if the experimental data has been collected too fast (allowing little time per angle to collect the diffracted X-rays), the intensity of the experimental peaks ( $y_{obs}$ ) tends to be very small since the detector collects very few X-ray photons. This causes  $R_{wp}$  to be too small and consequently the  $R_{exp}$  value will be very big resulting in a  $\chi^2$  much less than one.<sup>98</sup>

XRD patterns were measured with a Phillips APD 3720 diffractometer, courtesy of MAIC at the University of Florida. For comparison we obtained data from the Advanced Photon Source (APS) in Argonne, Illinois, with the help of Dr. Jacob Jones in the Dept. of Materials Science & Engineering (MSE) who has an active collaboration with the APS. In the APD3720 the samples were mounted and glued on diffraction slides with an acrylic spray which was also used for a blank background to be able to subtract any background signal peaks.

The background pattern of the acrylic spray itself is flat with very little noise and the spray is suitable to use for our powders. Samples were placed on the slide holder and inserted into the diffractometer. All patterns were collected using the following parameters: 0.5 seconds per degree, a range of 10 – 90 degrees, 0.02 degrees increment per second, 20 mA, 40 kV, on a source of Cu  $K\alpha_1$  (1.5408 Å wavelength) without filter.

The samples prepared for the APS were inserted in Kapton capillaries and fixed mainly at the center of the capillary. The capillary ends were sealed using Cha-seal<sup>®</sup> from Kimble Chase which is used in our lab for sealing EPR capillaries to avoid sample loss during transport or during experiments. The Kapton capillaries were placed into a sample holder and shipped to Argonne. The radiation wavelength at the 11 BM (bending magnet) at the APS facility was calibrated at 0.413068 Å.

The goal of Paragraph 2.3.4 is to describe the experimental results which have provided insights into structural changes upon annealing of the powders. We started with the initial hypothesis that our powders were mainly composed of amorphous  $NiB_3$  and a theoretical XRD pattern was obtained using the predicted structure described in

Paragraph 2.2. In particular, we are interested in the peaks at low angles arising from the (101) and (002) diffraction planes. For pure monoclinic  $P2_1/cNiB_3$  the peaks fall at 20.17 and 21.60 degrees while they show up at 19.83 and 24.62 degrees for the orthorhombic  $Pnma$  case. These low-angle peaks are absent in all nickel-rich nickel boride structures surveyed in the literature.<sup>49,51,52,72,99</sup> Similar calculations are currently underway in the lab of our collaborator in Switzerland (Dr. R. Caputo) for the  $NiB_2$  system.

#### **2.3.4.1 Powders as Synthesized (Under Normal Laboratory Conditions)**

The XRD pattern of the as-prepared powders was dominated by the crystal peaks of unreacted sodium borohydride and sodium bromide (Figure 2-15). The background was fitted with a power function. The residual curve is found below the refinement (grey line).

The increasing intensity of the background towards lower angles is due to the amorphous nickel borides. Generally, nickel borides synthesized in aqueous solution under normal laboratory conditions yield an amorphous XRD pattern similar to the one we have detected (see Figure 2-16).<sup>39</sup> Rietveld refinement of an unstructured pattern observed from a sample with amorphous structure is not possible and would not give useful results.

#### **2.3.4.2 Annealing the Powders under Ar(g)**

We performed annealing experiments on the powders under inert argon atmosphere at 773 K and at 1100 K for 1 and 5 h each. The resulting XRD patterns after 1h annealing time at 773 and 1100 K are compared to the as-synthesized sample in Figure 2-17.

As it is easy to see the 1h annealed powders patterns are similar to each other.

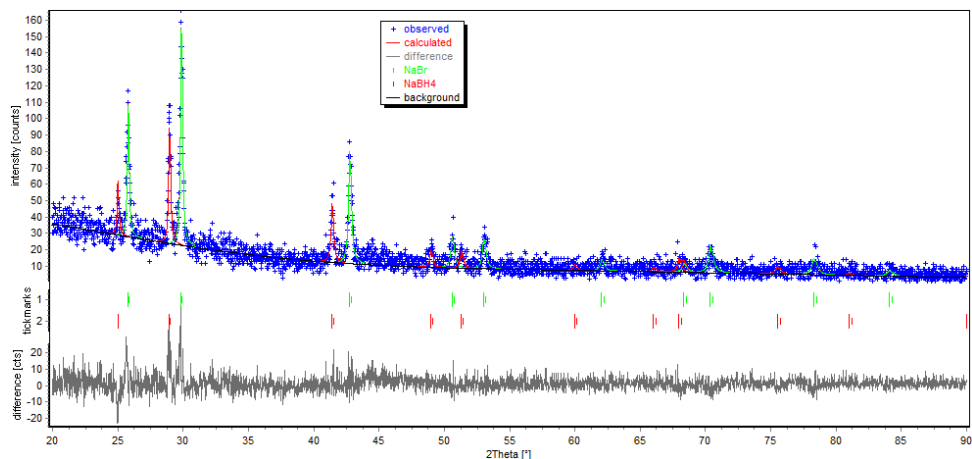


Figure 2-15. XRD pattern of the freshly prepared powders. Blue: Experimental pattern. Red: NaBr. Green: NaBH<sub>4</sub>. Grey:Residuals.

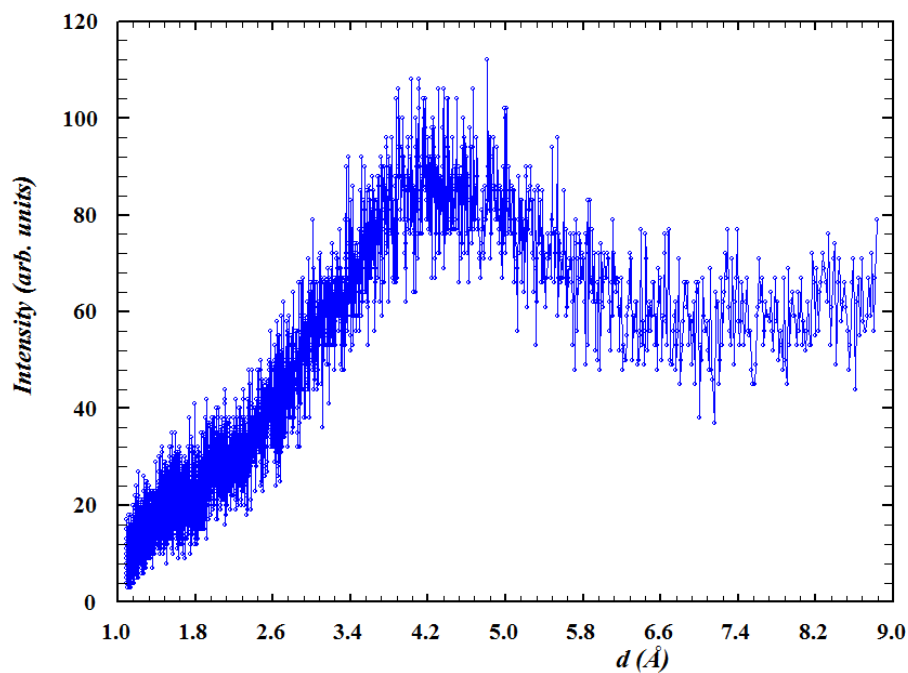


Figure 2-16. XRD pattern obtained on the hydrolyzed powders.

The pattern all look broad and no reasonable crystalline pattern is observed. For this reason no conclusion could be taken from the spectra annealed for one hour, and no refinement was possible since there were no crystalline patterns to refine. For these reasons we decided to extend the annealing time in attempt to observe a crystalline

pattern that could be refined, and so giving us semi-quantitative data or, alternatively, a full refinement of a NiB<sub>2</sub> crystal structure.

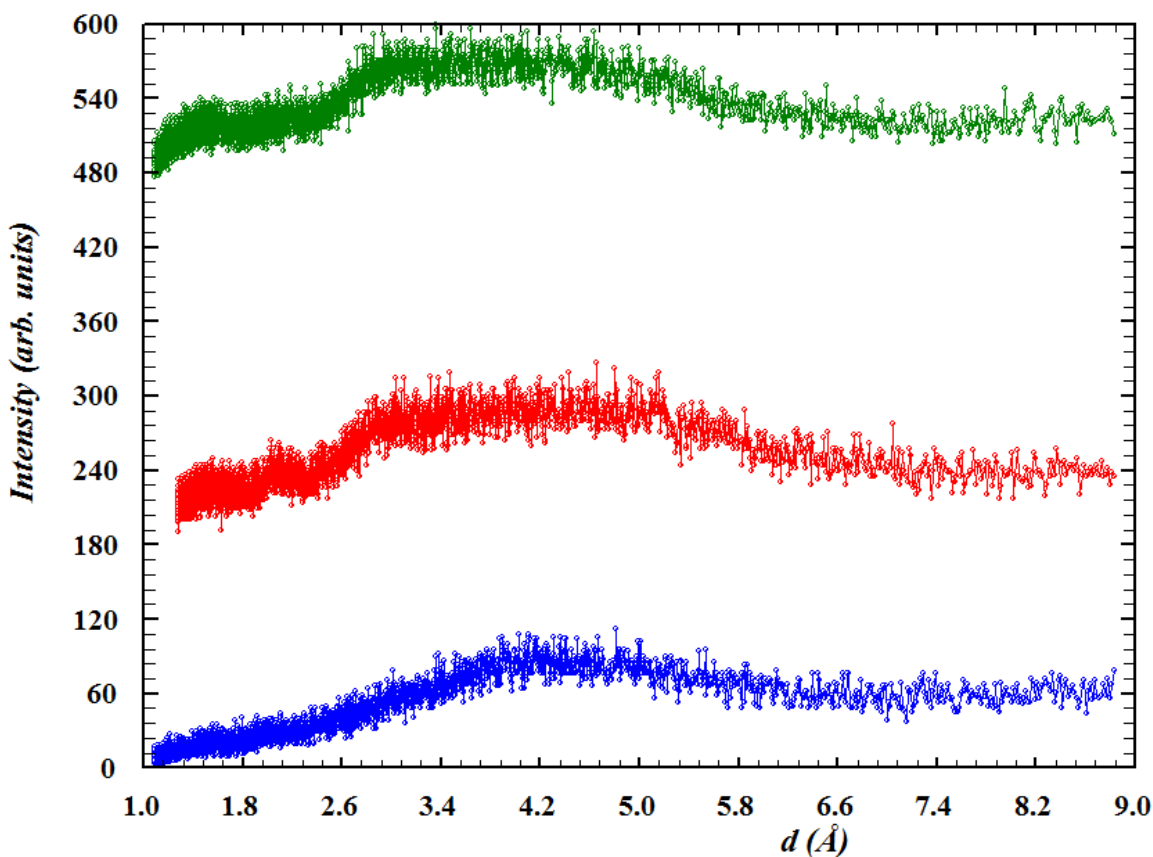


Figure 2-17. Annealing patterns. Blue: Hydrolyzed powder not annealed (298 K). Red: Annealed at 773 K for 1 h. Green: Annealed at 1100 K for 1 h. All patterns were taken with the APD3720 instrument (UF Dept. of Material Science & Engineering).

As can be seen from Figure 2-17, there is not much change when the powders are annealed for 1 h both at 773 and 1100 K. Therefore, we explored longer annealing times. Figure 2-18 shows the powders at room temperature, 1100 K annealed for 1 h powder and 1100 K annealed for 5 hours. The longer annealing time resulted in a crystalline XRD pattern. Attempts at using refining this pattern and assigning a structure to it have so far failed. None of the available nickel-rich nickel borides nor the theoretical NiB<sub>3</sub> structure are able to fit the experimental pattern.

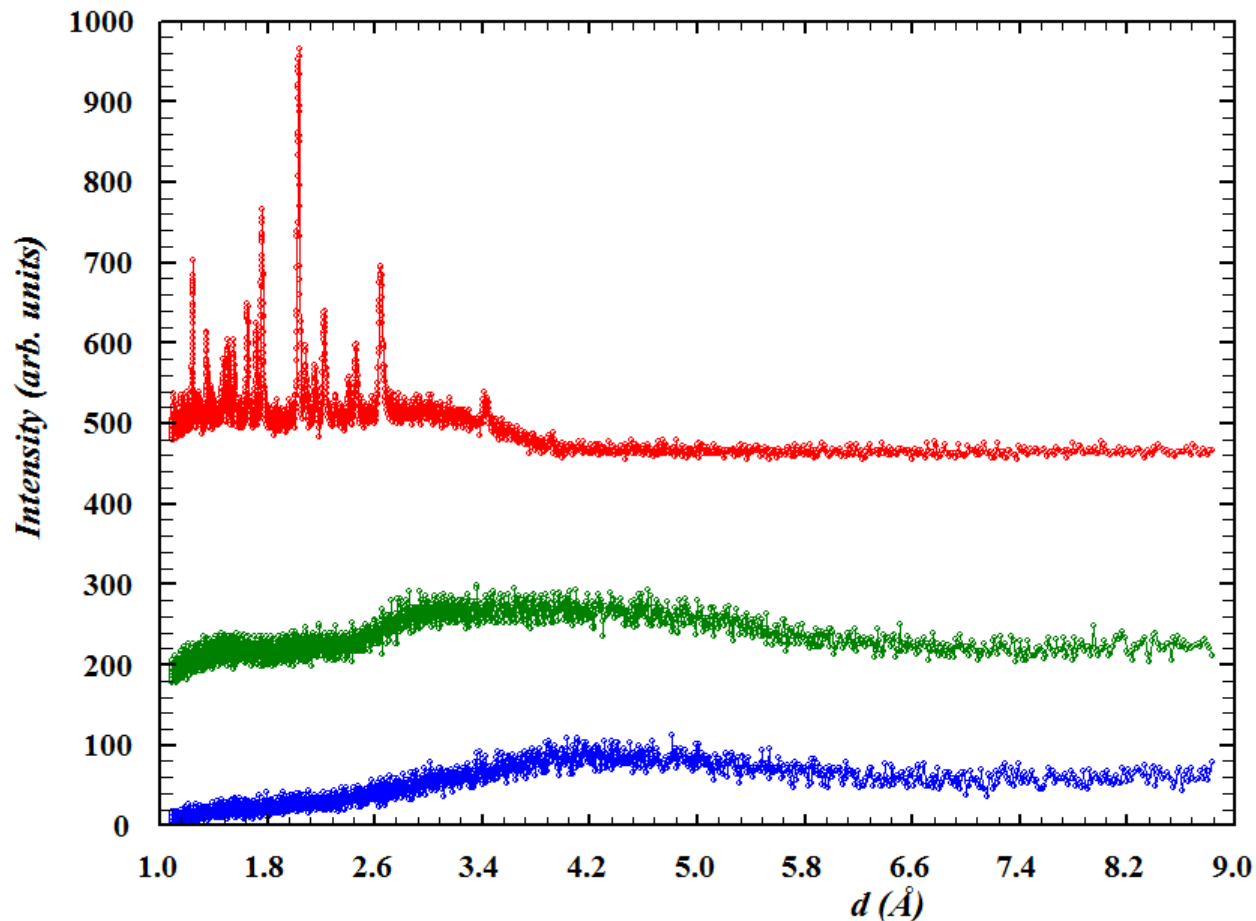


Figure 2-18. Blue: RTP hydrolyzed powder pattern. Green: Annealed for 1 h under Ar(g) at 1100 K. Red: Annealed for 5 h under Ar(g) at 1100. Experimental patterns were taken at the APD3720 (UF).

Samples were sent to the APS at the Argonne National Laboratory in Argonne, Illinois, to improve resolution and eliminate instrumental broadening. The samples sent to the facility were prepared with 5 mol-% Ni in sodium borohydride as non-hydrolyzed, hydrolyzed (normal lab conditions), annealed at 773 K for 5 h under Ar(g), and annealed at 1100 K for 5 h under Ar(g).

XRD scans were taken at the 11-BM, with a wavelength of 0.413068 Å. Figure 2-19 shows the patterns obtained at the APS in Argonne.

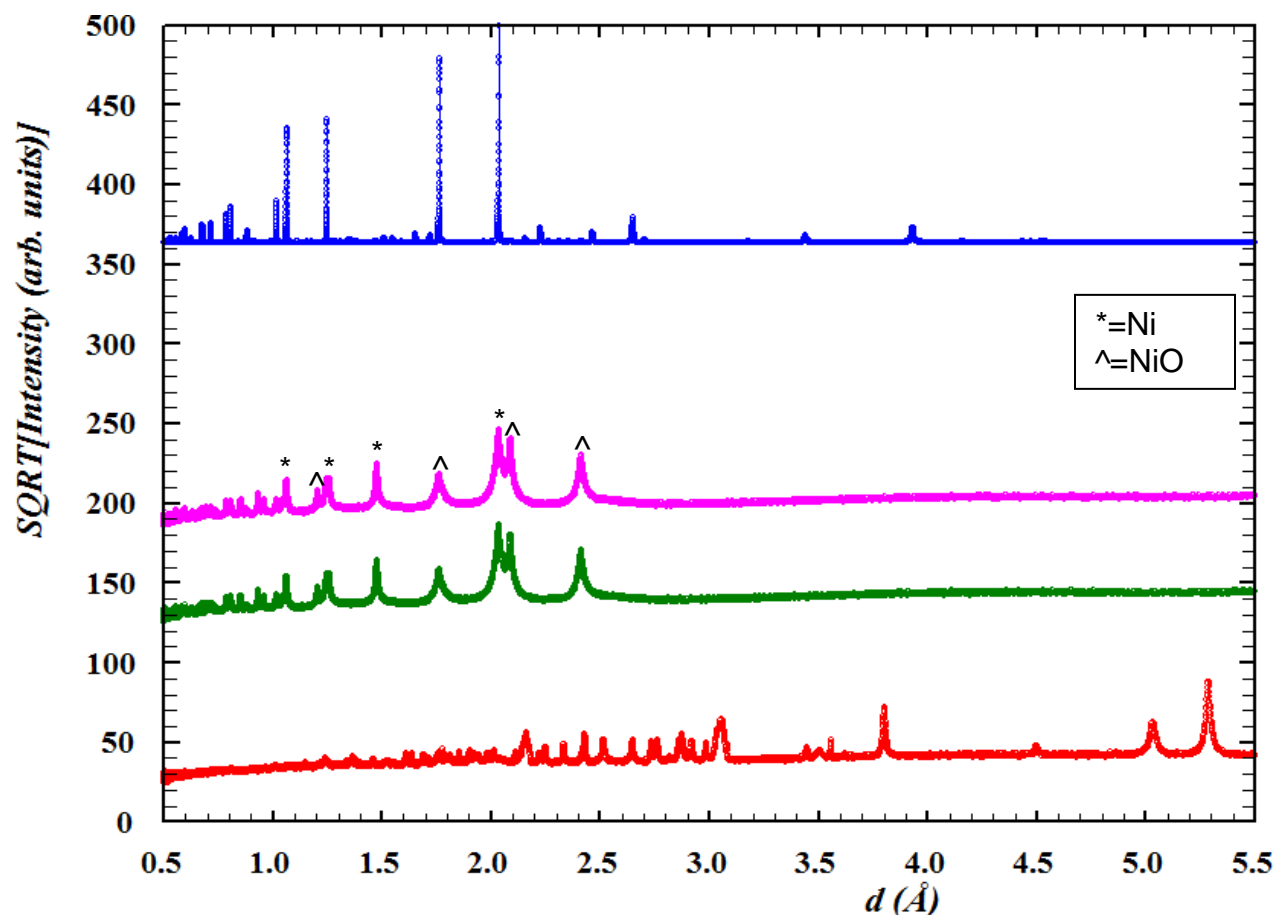


Figure 2-19. XRD patterns obtained at the 11BM beamline of the APS in Argonne. Plots are presented in  $d$ -spacing. The y-axis reports the square root of the intensity. Red: Un-hydrolyzed powder. Green: Fresh hydrolyzed powder. Magenta: Powder annealed at 773 K under Ar(g) for 5 h. Blue: Powder annealed at 1100 K under Ar(g) for 5 h.

Air handling of the powders and the time difference between the in – house measurements and the Argonne ones (aging), may also have altered the composition of the powder due to oxidation of the samples resulting in nickel, and nickel oxide patterns.

It is easily seen that the patterns are different, even though the freshly hydrolyzed and the 773 K annealed powders are dominated by the nickel and nickel oxide. The peaks, however, of these two patterns are wide, sign that the nickel and nickel oxide crystals are very small, maybe nanoscopic scale. Furthermore, the intensity of the nickel oxide peak versus the intensity of the nickel peaks is slightly weaker, sign that nickel

oxide crystallites quantity is comparable to nickel metal crystallites. However, the width of the peaks seems not to change up to 773 K. The un-hydrolyzed powder pattern (red), as in the in-house instrument, seems to be dominated by the  $\text{NaBH}_4$  matrix which is dominating. The last pattern, coming from the powder annealed under argon at 1100 K for 5 h, seems to be quite different from the others: the lines narrow down (this means bigger crystals) and also peaks from other crystal phases appear, which may be due to the unknown nickel boride. However, since the  $\text{NiB}_3$  crystal structures hypothesized were never found, and thanks to the absence of reliable  $\text{NiB}_2$  structures, it is difficult to understand if some peaks can be attributed to  $\text{NiB}_2$  or if other phases are crystallizing. One possibility is that some boron oxide is crystallizing, as nickel oxide and metallic nickel, inside the powders; however, the formation of some nickel borate ( $\text{Ni}_3(\text{BO}_3)_2$ ) cannot be excluded, nevertheless the care used in maintaining the whole experiment under argon flow.

The APS instrument allows reflected radiation to be observed at lower angles than in the in-house instruments which means that larger  $d$ -spacings can be observed. The conversion between spacing and angles comes directly from Bragg's law.  $d$ -spacing plots are useful because they reflect the distances between planes, in a crystalline material and should be independent of the instrument used. We present all XRD spectra as a  $d$ -spacing plot as this allows for easy comparison between the different instruments used. Since the planes in a crystal are defined by the crystal lattice, it is possible to determine the crystal lattice constants.

#### **2.3.4.3 $\gamma$ -Irradiation of the Powders.**

Concerns were raised about radiation damage due to the high flux rates under which the experiments were done. To ensure that the peaks arising at 1100 K are not due to

radiation damages of the sample (the beam uses beam energies of around 30 keV) we irradiated the material with  $\gamma$ -rays ( $^{60}\text{Co}$  source) for different lengths of times: 10 minutes, 1 h, 1 day and 1 week. Figure 2-20 shows the patterns arising from these data.

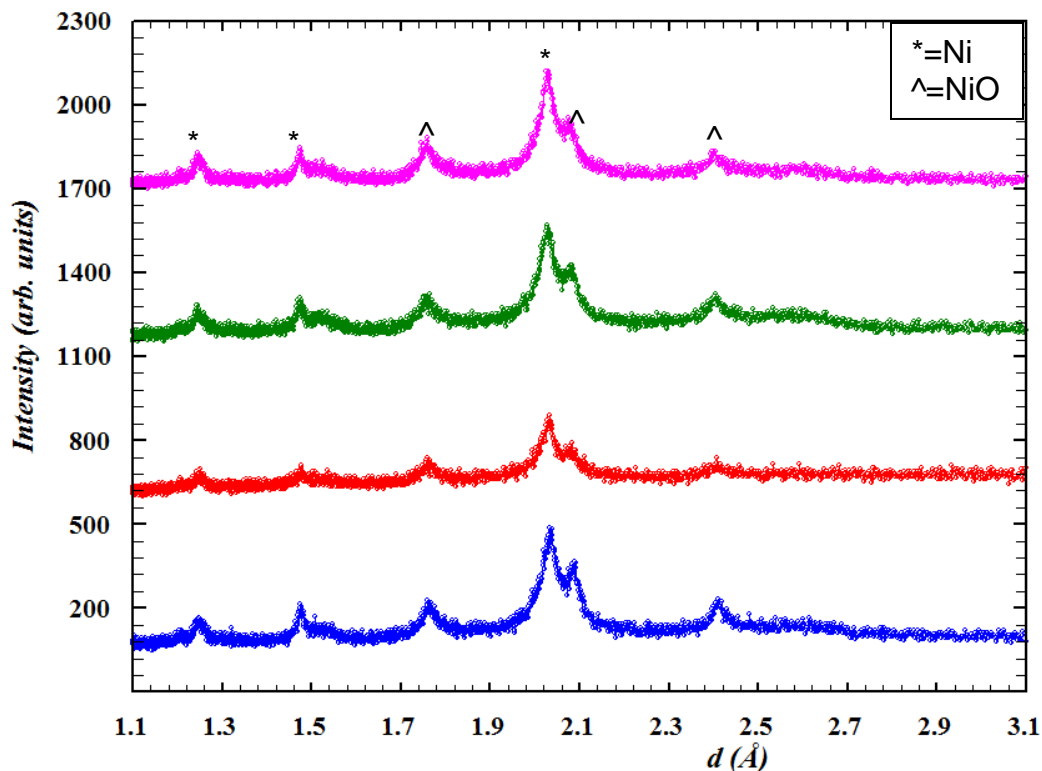


Figure 2-20.  $\gamma$ -irradiated NiB<sub>x</sub> samples after 10 mins (blue), 1 h (red), 1 day (green) and 1 week (magenta). Patterns were collected at the APD 3720 (UF).

Clearly, radiation damage can be excluded as the source of the observed XRD patterns.

### 2.3.5 Quantitative Elemental Analysis: ICP-AES

Elemental analysis was carried out by ICP-AES (Inductively Coupled Plasma – Atomic Emission Spectroscopy).

ICP-AES is useful in determining the relative concentration of the elements in an unknown compound. In fact the intensity of the emission lines, which are specific for each element, is proportional to the concentration of the element itself. Since the

sample under study has an unknown composition, it is practical to use methods of calibration of the emission intensity. There are several methods available for standard calibration in which a standard of known composition and purity is used and compared to the unknown. In the standard addition method a standard for a certain element is added to the analyte in solution (analyte and standard must contain the same element). Subsequent addition followed by linear extrapolation back to the abscissa, yields the elemental concentration in the analyte. The calibration curve method uses a series of known increasing concentrations of the element under analysis. Again, the intensity of the emission lines is plotted against the total concentration giving a linear correlation between the intensity/concentration. The unknown concentration must be in the range of the concentrations used and its value is obtained by localizing the intensity of the analyte on the calibration curve.

Generally, a solid sample is solubilized in a suitable solvent and then diluted with water to test for linearity of the detector response. The solution is injected into an ionizing flame using Ar gas as the carrier. It is good practice to test whether the solvent or acid used to dissolve the solid sample interferes with the analysis. Therefore blanks are used to record a zero point, i.e., the point for which the chosen wavelength(s) will have zero or minimal intensity because of the negligible quantity of the analyte in question.

A Varian Vista CCD Simultaneous ICP-AES, which allows for the determination of multiple elements simultaneously, was used in these experiments.

#### **2.3.5.1 Determination of the Nickel Amount in the Unknown**

The following lists the protocol for the example of a sample of room temperature-hydrolyzed powders. The sample was weighed in at 14.4 mg and was dissolved in 1.0

mL of fuming nitric acid (90.7%, Fisher) and diluted 100 fold with NanoPure (Barnstead) 18.2 M $\Omega$  cm<sup>-1</sup> water. We prepared a series of standards in which [Ni] was equal to 0 (stock fuming nitric acid 100 fold diluted with NanoPure water as blank), 0.025, 0.05, 0.25 and 0.5 mM respectively, using solid NiCl<sub>2</sub>·6H<sub>2</sub>O (Fisher) as the Ni(II) source. The amount of Ni(II) per each solution was 1.47, 2.93, 14.7 and 29.3 mg of Ni(II) per L of solution. However, the final volume of the solutions was 100 mL, therefore a factor of 10 was needed to determine the amount of Ni(II) in the standards and in the unknown.

A calibration curve was generated for these samples as seen in Figure 2-21. The plot shows a linear correlation between the intensities of the standard at both observation wavelengths of Ni (231.604 and 232.138 nm) and their concentration with  $R^2$  values of 0.9968 for 231.604 nm and 0.9943 for 232.138 nm. The intensities of the unknown concentration observed at both wavelengths were 6068.7 and 783.65, and fell in the range of the concentrations used. The amount of nickel deduced in the sample of nickel borides was 1.877±0.006 mg in 14.4 mg of sample.

In order to obtain a molar ratio between boron and nickel, elemental amounts were calculated in mg of analyte per gram of sample used. Therefore if 0.032 mmols of nickel, (i.e. 1.877 mg of nickel) are found in 14.4 mg of sample, 2.22 ± 0.01 mmols (i.e. 130 mg of nickel) are found in 1.0 g of sample. Errors were calculated using the least square method, and reported as standard deviation from the mean value. The relative error on the amount of nickel is of the magnitude of 0.3%.

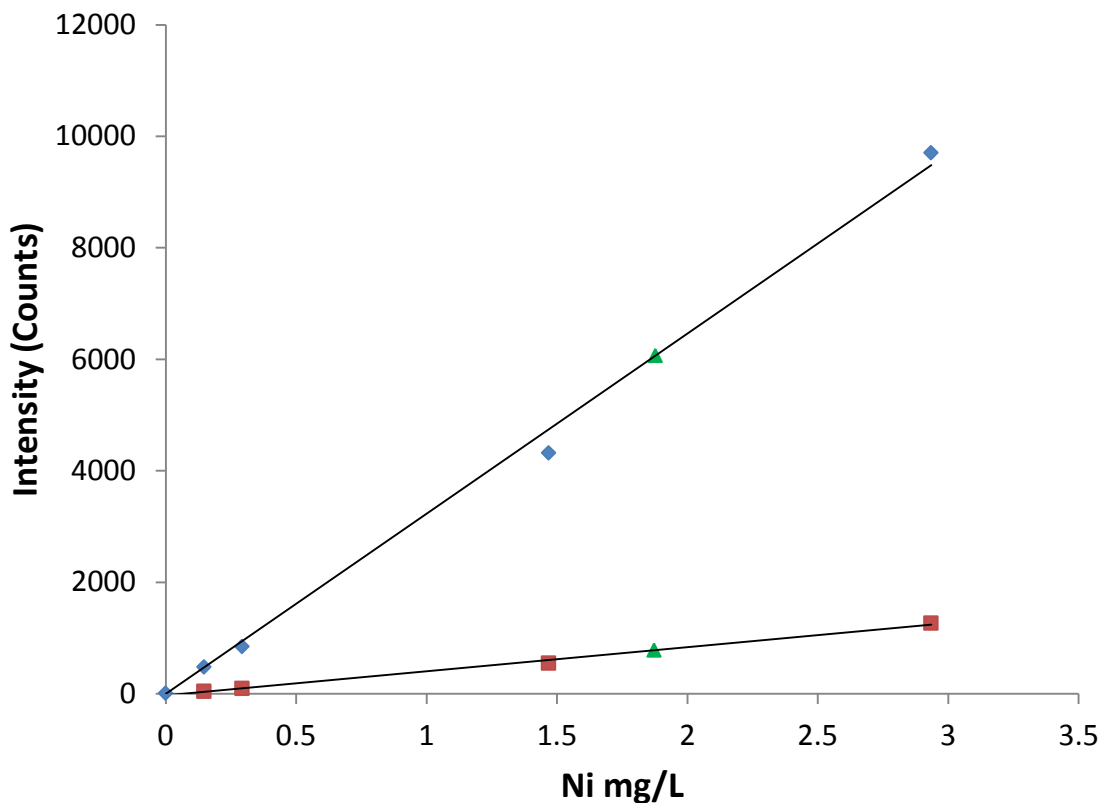


Figure 2-21. Correlation plots for the nickel standard observed at 231.604 nm (blue diamonds), and at 232.138 nm (red squares). The green triangles represent the unknown concentrations at both wavelengths.

### 2.3.5.2 Determination of the Boron Amount in the Unknown

Attempts to measure boron amounts through ICP-AES were met with initial difficulty. 14.2 mg of the unknown sample and 3.1, 5.0, 6.7, 11.8, 17.2 and 23.5 mg of  $MgB_2$  (i.e. 1.5, 2.4, 3.2, 5.6, 8.1, 11.1 mg of B) (our standard), were placed in quartz tubes and dissolved using 3.0 mL fuming nitric acid for the  $NiB_x$  and 5.0% commercial (Fisher) nitric acid for the  $MgB_2$ . The vigorous reaction between the  $MgB_2$  and the concentrated acid forced the use of dilute nitric acid in order to obtain a clear solution without any solid spill. One mL of each solution was further diluted 50-fold. Data were collected in a similar way as for nickel using two known emission lines for boron at 249.678 and 249.772 nm.

The standard calibration curves for boron are presented in Figure 2-22 together with the intensities observed from the unknown.

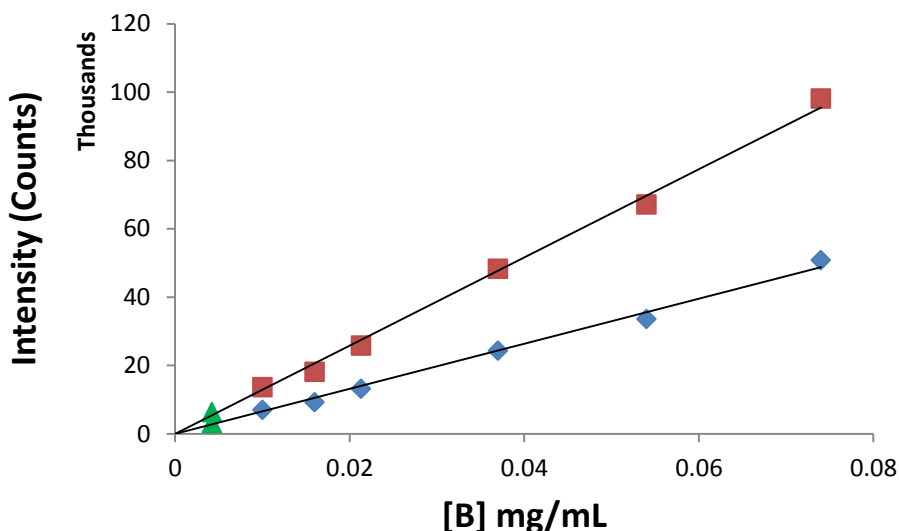


Figure 2-22. Correlation plots for the boron standard observed at 249.678 nm (blue diamonds) and at 249.772 nm (red squares). The green triangles represent the unknown concentrations at both wavelengths.

The plots showed a linear correlation between intensity and concentration with  $R^2$  values of 0.9961 (for the line at 249.772 nm) and 0.9929 (for the line at 249.678 nm). Intensities are reported in thousands of counts. The intensities of the two B lines for the unknowns averaged 3116.73 and 6216.41 counts yielding  $0.00421 \pm 0.00001$  mg B per mL of solution. The relative error on the amount of nickel is of the magnitude of 0.2%.

Results were converted into mmol of Ni or B per g of compound. The amount of nickel was  $2.22 \pm 0.01$  mmol per gram of compound and that for boron was  $4.11 \pm 0.01$  mmol per gram of compound. The molar ratio  $\frac{\text{mmol B}}{\text{mmol Ni}}$  was 1.851:1. The relative error on the moles is 0.004 moles, which is the 0.2% from the average value. This result, however, confirms our second guess, in which the structures should have shown a stoichiometry of 2 mols of boron per mole of nickel, as discussed in the Paragraph 2.1.

### 2.3.6 Quantitative Analysis: XRD Refinement

Whenever a pattern is retrieved from a multi-crystalline phase, it is possible to determine the relative quantity of each of the phases from a Rietveld refinement.

In fact, all the software, including BRASS (the one used in our work), use the same equation to determine the relative quantity for each of the phases composing a multi-crystalline powder, as described by Hill and Howard:<sup>100</sup>

$$w_p = \frac{S_p(ZMV)_p}{\sum_j S_j(ZMV)_j} \quad (2-18)$$

where:  $w_p$  is the weight fraction (or mass fraction, they are still called weight fraction but with the same meaning),  $S$  are the scale factors of the phases,  $Z$  is the number of unit formula in the unit cell,  $M$  is the molecular weight of the formula unit, (therefore  $Z \cdot M$  is the molecular mass of the unit cell) and  $V$  is the unit cell volume.

The total quantities of nickel and boron which reacted in a typical experiment were determined through the analysis of quantitative data calculated from the refinement shown in Figure 2-15. Results are presented in Figure 2-23 and reported in mol-%. After the reaction, the unreacted  $\text{NaBH}_4$  was  $83 \pm 5\%$  of the initial. This value corresponded to 8.40 mmols. The amount of  $\text{NaBH}_4$  initially used for the reaction was 10.07 mmols. This suggests that 1.67 mmols of sodium borohydride had reacted with 0.52 mmols of nickel bromide. According to this analysis the ratio  $\frac{\text{molB}_T}{\text{molNi}_T}$  was estimated to be 3.2:1.

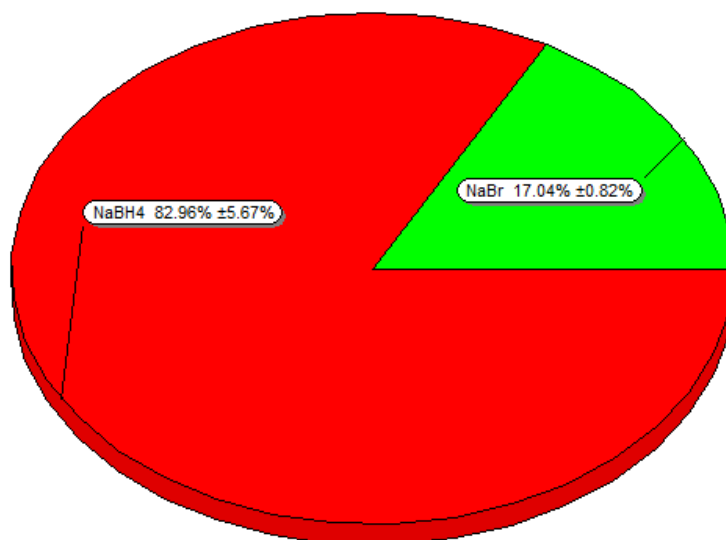


Figure 2-23. Quantitative results from the XRD refinement shown in Figure 2-15.

### 2.3.7 XPS

XPS (x-ray photoelectron spectroscopy) is a surface technique which relies on core-ionization potentials and detects kinetic (or binding) energies of the emitted electrons. Spectra are collected under high vacuum to avoid ionization of air and scattering of the released electrons at gas molecules. This technique can determine quantitative information of the elements on the surface of the sample. However, care has to be taken when trying to extend the interpretation of the results to the bulk sample.

The main advantage of this technique is the possibility to discern between different oxidation states of a particular element depending on the peak position and shape. In this work, an extensive XPS study has been performed on the nickel borides to determine their surface composition and to reveal oxidation states of both Ni and B.

XPS has been widely used to study the surface composition of nickel borides<sup>50,80</sup> as well as nickel boride nanoparticles.<sup>101</sup> However, these earlier studies only deal with nickel-rich nickel borides.

The instrument used to perform XPS on the samples prepared was a Perkin Elmer 5100 XPS System, courtesy of MAIC at UF. As a reference for the Boron 1s peak commercial crystalline MgB<sub>2</sub> was used. All peak positions and relative shifts shown by the instrument must be referenced to the C 1s peak that is set at 284.6 eV by default.

Survey experiments were performed under the following experimental parameters: 300 kV, 15 mA, 0.5 eV step, 0 – 1320 eV for MgB<sub>2</sub> and 0 – 1100 eV for the unknown powders.

HR (high resolution) spectra were acquired for boron, magnesium, carbon (reference), oxygen, and nickel (the latter measured only in the samples).

HR spectra were acquired 40 times, with a step of 0.1 eV, and range of  $\Delta E$  of ~10 – 30 eV from the center of the peak. This  $\Delta E$  was chosen based on the width of the peak (or the multiplet) assigned to a particular element. The shifts of the peaks were determined by the difference in binding energies between the default position of the carbon peak and the experimental value. Both the experimental and the projected unshifted C 1s peaks are shown in Figure 2-24.

The difference in binding energies between both peak positions is the shift that needs to be subtracted from each of the other peaks to correct for instrumental shifts in a particular experimental setup.

Peak shifts, which are sample-dependent, are calculated on the basis of the shift of the C 1s peak coming from impurities (anion of the nickel) of the sample (as in Okamoto et al.<sup>50</sup>) or, as in our case, from the position of the sample inside the sample holder, since the sample was placed in a paper – stick slide with organic glue on it.

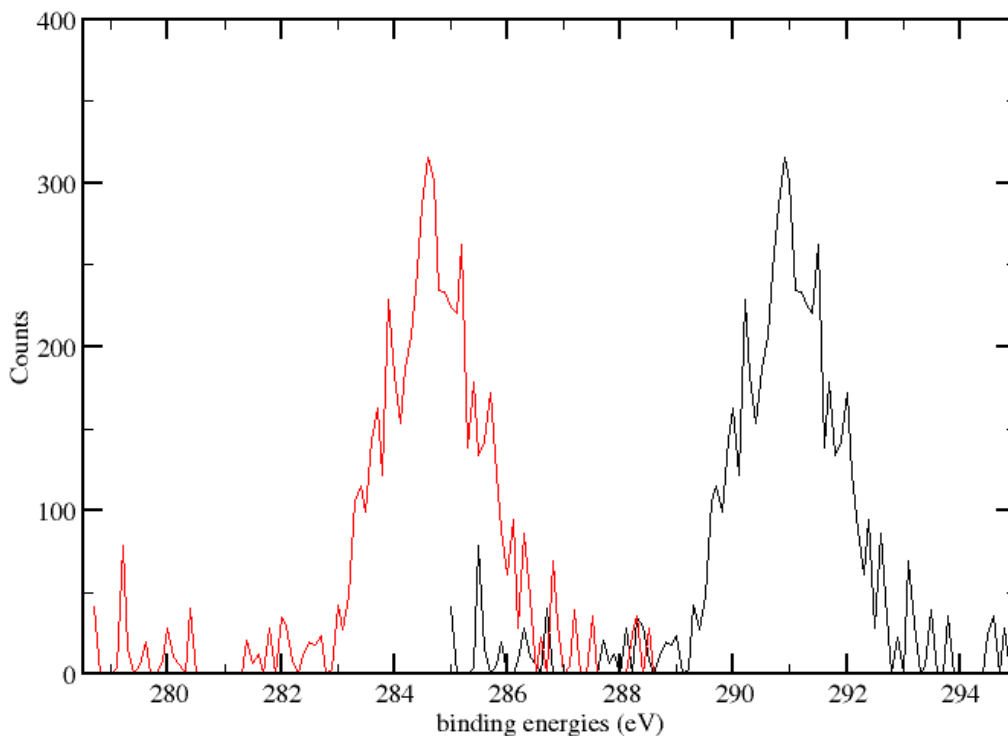


Figure 2-24. Room temperature C 1s peak. The black line represents the as-determined peak, the red one is the peak as expected for the default C 1s position.

The paper stick may have slight different angles or slight different organic composition which may alter both the intensity and the position of the carbon peak. However, to eliminate this issue, which can generate heterogeneous results, the instrument has set a C 1s reference which happens at 284.6 eV. On the basis of relative shifts for this peak, peak shift was determined this way for each set of data. The shift values are 6.3 eV for the room temperature hydrolyzed sample; 7.1 eV shift for the powder annealed at 500 C and crushed in open air in mortar and pestle and 5.1 eV for the 830°C annealed powders. MgB<sub>2</sub> presented a shift of 6.2 eV, very close to the shift presented by the room temperature sample (6.3 eV). In this work the data of the XPS study are presented as received from the instrument. Literature reports XPS data only

for nickel-rich nickel borides which will be compared to our  $\text{NiB}_x$  here. In particular, B 1s peaks are assigned to elemental boron and oxidized boron.<sup>50,80,101</sup>

### 2.3.7.1 Determination of Nickel through XPS

Three nickel boride samples were measured after the following treatments a) after hydrolysis of the sodium borohydride matrix at RTP (room temperature and pressure), b) after annealing at 500°C for 5 h under Ar(g) and c) after annealing at 830°C for 5 h under Ar(g). The Ni 2p peaks are shown in Figure 2-25.

Nickel in the 0 oxidation state is generally found at ~852 eV.<sup>50,80</sup> Samples investigated in this work show in all cases nickel peaks in the range between 854.9 and 855.6 eV after correction for peak shifts. A value for nickel at 852 eV is not observed excluding metallic Ni at the surface of the sample. The difference in energy between the theoretical value for nickel metal and the experimental values ranges between 2.9 and 3.6 eV.

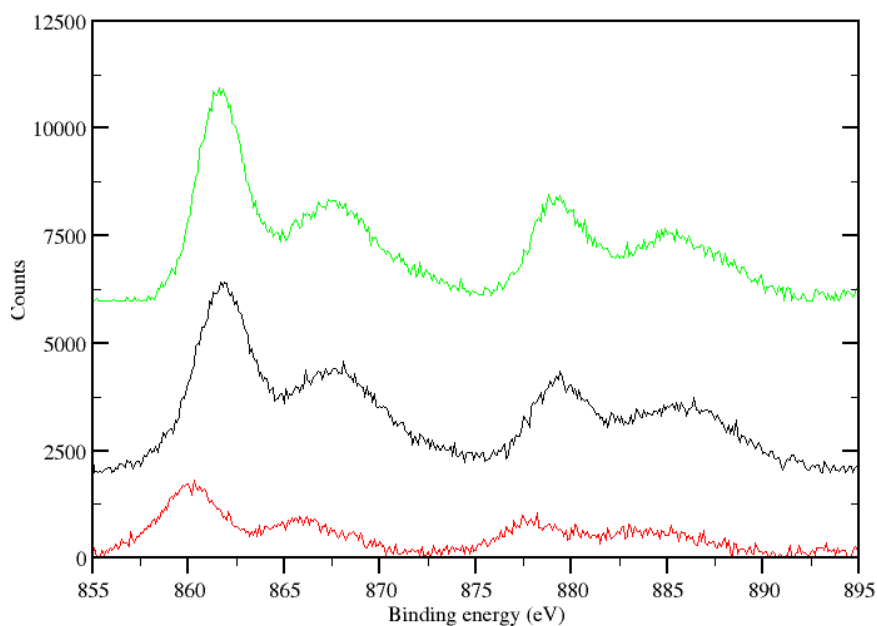


Figure 2-25. Ni XPS spectra under the following sample conditions: rtp (in red), sample was annealed at 773 K for 5 h, sample was annealed at 1100 K for 5 h (green).

### 2.3.7.2 Determination of Boron through XPS

Boron is present in two different forms in  $\text{MgB}_2$ , as elemental boron (stronger peak, at lower binding energies) and oxidized boron on the surface (weaker peak, at higher binding energies). After peak shift correction these peaks are found at 186.6 eV and 190.83 eV, respectively (see Figure 2-26). The relative distance between the two peaks is 4.23 eV.

Figure 2-27 shows the B 1s peaks, zoomed in from the survey experiments, and compared with the B 1s peak of  $\text{MgB}_2$ . Normally, B 1s peaks fall between 185 and 190 eV. Our nickel boride samples show one main peak at 191.7 (for the room temperature sample) and 191.9 eV for the annealed samples. All the spectra, in the region below 185 eV, show weak peaks, noticeably a weak band which appears above the noise level at 181.7 eV (room temperature sample) and 181.9 eV (for the annealed samples).

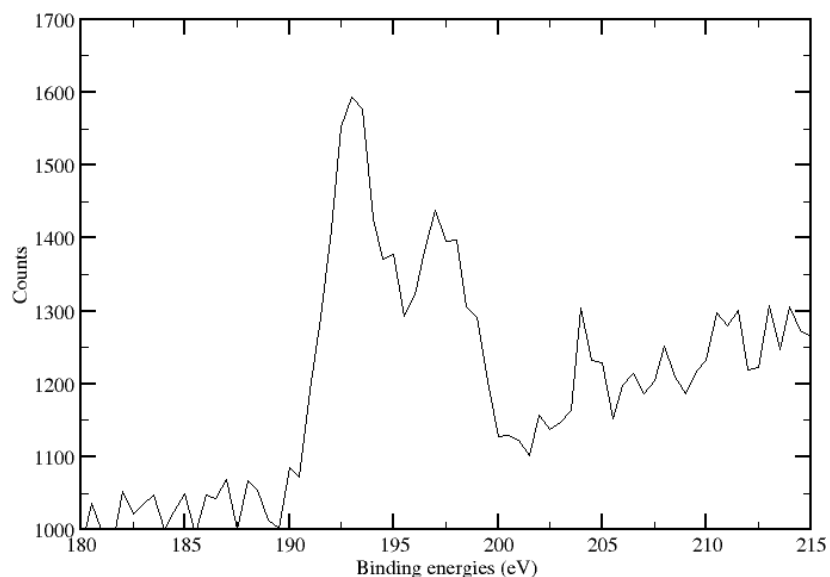


Figure 2-26. High resolution spectrum of commercial  $\text{MgB}_2$ .

This is not normally a range in which boron peaks are found. Since the intensity of this peak is rather low it might be possible to be a satellite peak.

To solve this question high resolution spectra were acquired in this energy range.

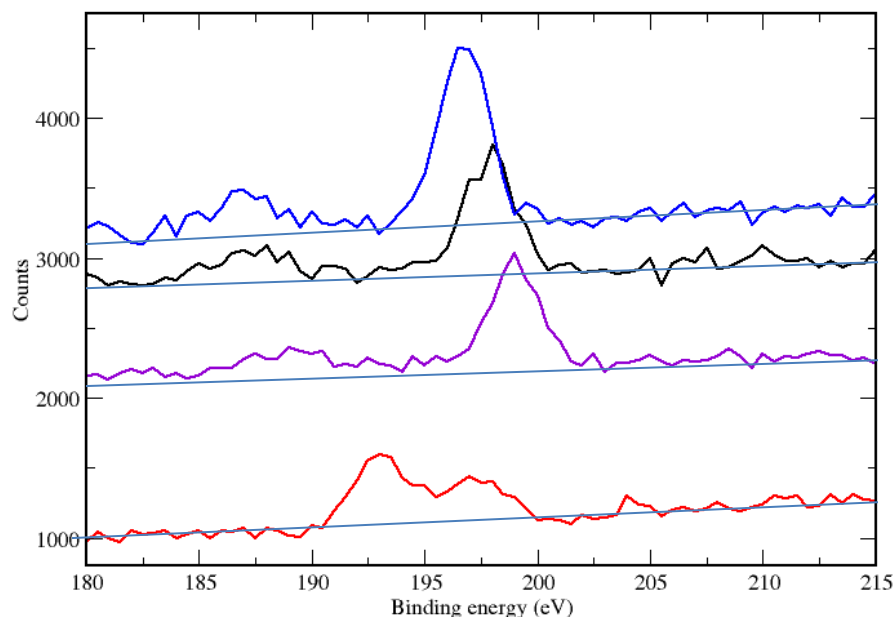


Figure 2-27. Comparison of the B 1s peaks: commercial  $\text{MgB}_2$  (red); powder hydrolyzed at RTP (violet); powder annealed at 773 K for 5 h under Ar (black); powder annealed at 1100 K for 5 h under Ar (blue).

High resolution spectra were acquired using two anodic materials: Mg and Al, which operate at different X-ray wavelengths. If the weak peaks are satellites of the main peak, a corresponding shift is expected in the two measurements. Moreover, the intensity of the satellite peak area should not be more than 6-8% of the main peak, depending on the anode used. Only one sample was analyzed in this way. The sample was the powder annealed at 500°C and quickly ground with mortar and pestle in air. The results are shown in Figure 2-28. The spectrum shows two peaks for boron with a relative intensity of approx. 1:3 for both lines. The energy difference between both peaks remained constant at ~10 eV for both X-ray sources.

This result is significant because it means that the peak arising at ~182 eV is not a satellite. It is also unprecedented, since all the nickel-rich nickel boride phases show boron peaks which appear at about 186 eV.<sup>50,80,101</sup> Furthermore, it is interesting that the

difference in energies between the two peaks is 10 eV, which is about 2.5 times the difference in energy of the B 1s peaks for  $\text{MgB}_2$ .

The energy difference between the (reduced) boron peak positions found in  $\text{MgB}_2$  and in our nickel borides ranges from 4.7 to 4.8 eV.

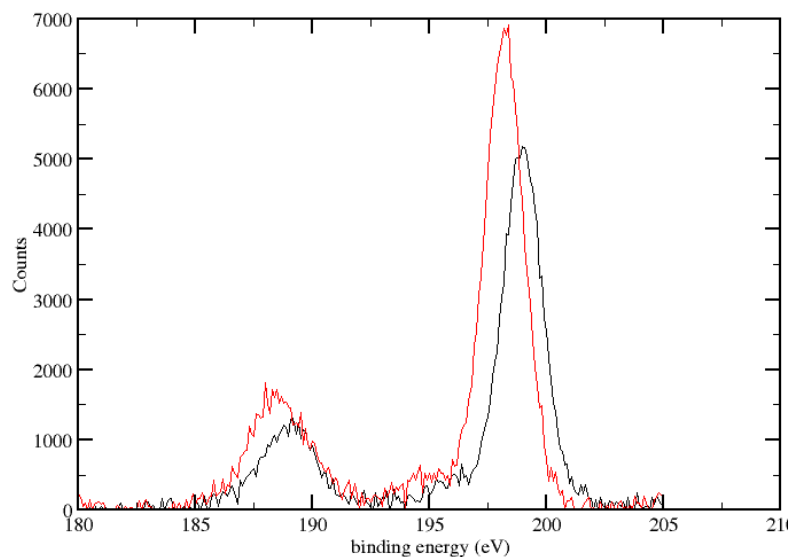


Figure 2-28. XPS HR spectra of the B 1s peak. Intensities ratio are 3:1 for oxidized boron. Al anode in black; Mg anode in red

### 2.3.8 Morphology of $\text{NiB}_x$

#### 2.3.8.1 TEM and EDXS

Microscopic studies are needed to determine the morphology of these powders. Since no crystal structure could be determined, yet, the aim of microscopy experiments is to resolve structural features which have not been revealed in other experiments.

T.E.M. (transmission electron microscopy), ED (electron diffraction) pictures of the powders, and semi-quantitative EDXS data (EDXS – Energy dispersive X-ray spectroscopy) have been collected at the ETH Zürich, Switzerland, in the group of Prof. Nesper.

Thanks to this technique periodic ridges, on the surface of the  $\text{NiB}_x$  grains were discovered. These ridges are spaced approx.  $65 \text{ \AA}$  apart in an almost periodic arrangement. Results are shown in Figure 2-29.

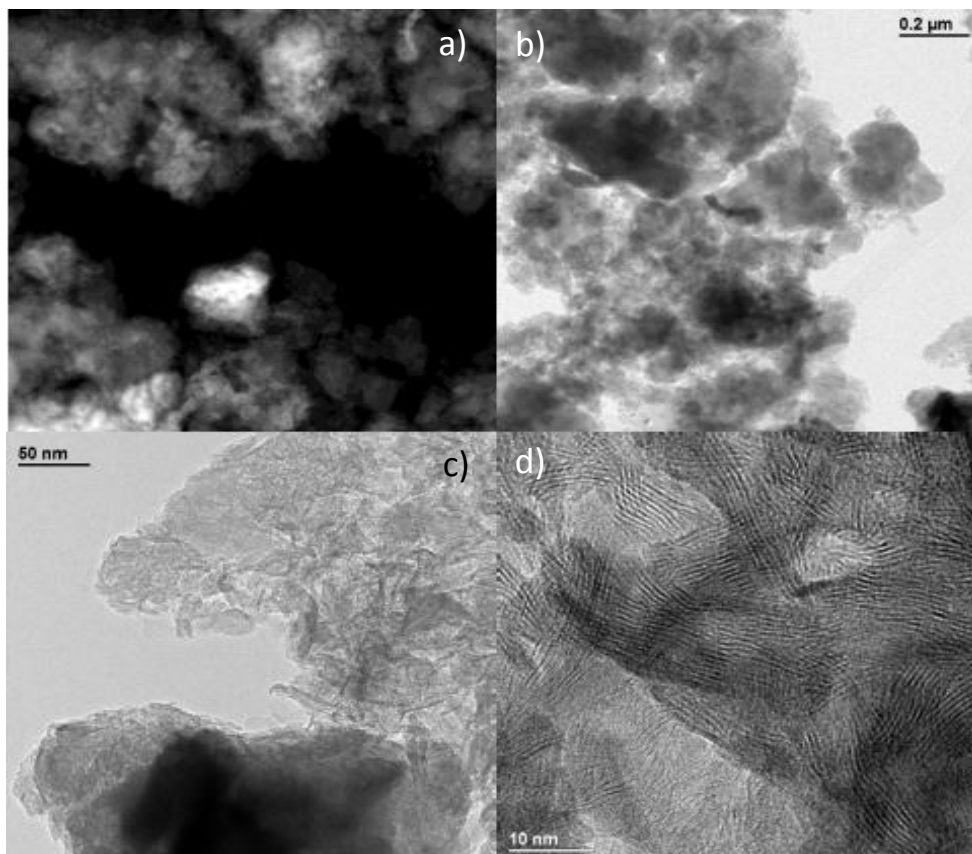


Figure 2-29. From a) to d), respectively: a STEM image and increasingly resolved TEM images of the powders.

Figure 2-29 shows a field emission Scanning Transmission Electron micrograph (a) and three TEM images with increased magnification. TEM images, taken at the same spot, with doubled magnification are shown in Figure 2-30. Higher magnification clearly shows the ridges which appear in ordered arrays, parallel to each other and separated by a constant distance of about  $65 \text{ \AA}$ . These experiments yield important information about the morphology of the particles in the  $\text{NiB}_x$  powders. In fact, the

discovery of these ordered arrays or ridges is reminiscent of the structures seen for  $\text{MgB}_2$  (see Figure 2-9).

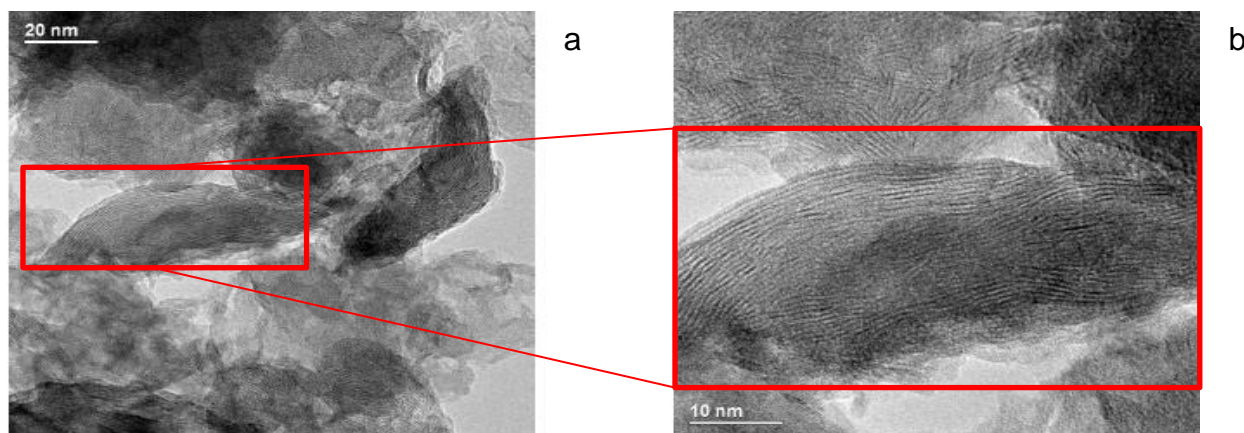


Figure 2-30. TEM images of a grain of material. a) and b) show images of the same grain of powder with the magnification doubled. The ridges can be readily seen on the surface of the grain.

Moreover, the TEM experiments allow to perform qualitative elemental analysis of the sample using the EDXS technique. The spectra of the unsupported amorphous  $\text{NiB}_x$  and  $\text{SiO}_2$ -supported  $\text{NiB}_x$  are shown in Figures 2-31 and 2-32. In the low energy range of the spectrum, boron and carbon peak positions are found within 0.2 eV of each other.<sup>45,102</sup> In the unsupported powder the spectrum reveals two peaks with only the carbon one labeled. However, the most intense peak can be attributed to boron, since it shows up at an energy lower than carbon.

The results for the supported amorphous  $\text{NiB}_x$  are not as clear-cut as those for the unsupported powders. However, even in this experiment it is possible to see that the position of the carbon label does not intercept the maximum of the peak.

Figures 2-31 and 2-32 show EDXS spectra of the non-supported  $\text{NiB}_x$  powders and the supported  $\text{NiB}_{2x}$  powders, respectively.

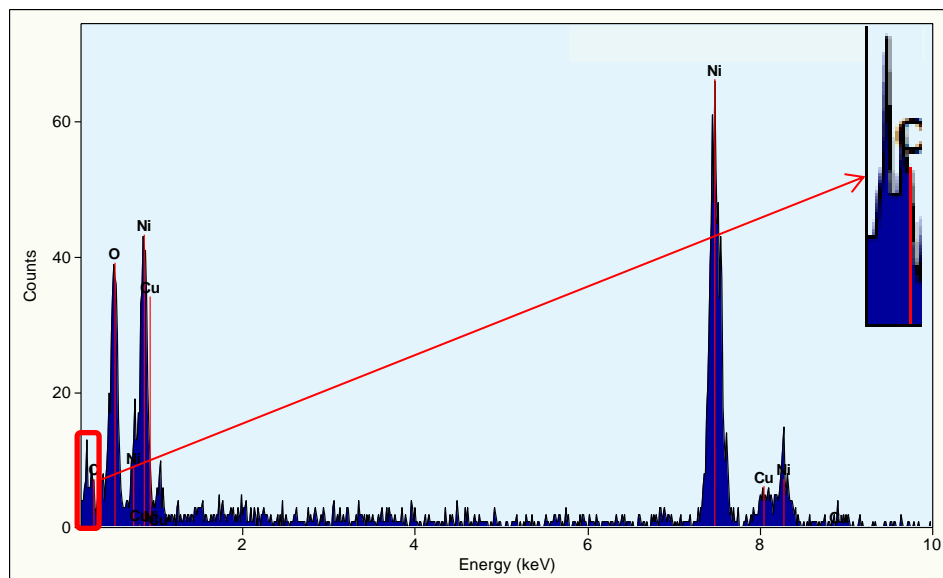


Figure 2-31. EDXS of  $\text{NiB}_x$  unsupported sample showing a boron peak which is more intense than the carbon peak. Nickel peaks are also clearly visible.

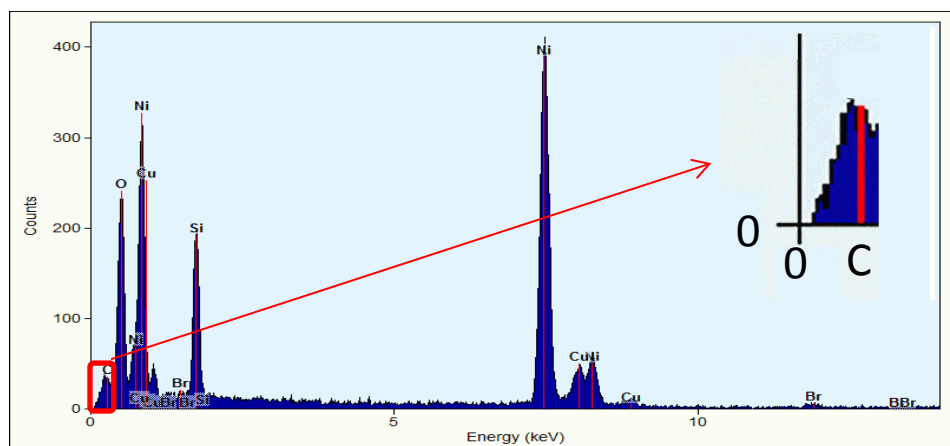


Figure 2-32. EDXS of the supported powders. The low energy peaks containing contributions from C and B are framed in red and zoomed in.

### 2.3.8.2 SEM Microscopy and EDS

SEM microscopy was employed to ensure the efficiency of supporting the material. Experiments have been performed by Dr. Wayne Acree at the MAIC, UF. The instrument used was a JEOL SEM 6400.

SEM is a technique which allows the investigation of surfaces of solid materials.

To ensure the best resolution, samples must be conductive or must be coated with a conductive material.

Analytes are placed on metallic or graphitic sample holders and then coated with gold or graphite. The surface of the material is revealed by contrast.

SEM images are shown in Figure 2-33. The length scales for the images are indicated by bars as 200  $\mu\text{m}$  (1-4) and 50  $\mu\text{m}$  (5-6).

The pictures indicate that, after the reaction with the nickel salt sodium borohydride loses its crystallinity to form a potentially amorphous material (Figures 2-33, a–b). In fact, the image in Figure 2-33 a) shows that the smooth surface of the sodium borohydride is evidently roughened after it reacted with nickel bromide. The borohydride grains, in fact, are not smooth as in the as-measured sample (which is shown by crystalline materials), but, instead, shows a roughened surface which may be due to the interaction with nickel bromide (and consequent liberation of hydrogen). The powders maintain an overall disordered amorphous-looking structure after hydrolyzation (Figure 2-33 b). Some elongated cylindrical structures (encircled by red ovals) can be observed (Figure 2-33 c), d). Amorphous  $\text{NiB}_x$  upon contact with silica covers the smooth surface of the hosting materials (Figure 2-33 e),f).

$\text{SiO}_2$  has been demonstrated to be a stable support for many nickel-rich nickel borides.<sup>32,37,41,45</sup> To determine whether  $\text{SiO}_2$  is also a stable support for boron-rich nickel borides, EDS analysis was performed during the experiment choosing a spot on a grain of the composite material.

This experiment can ensure if silica can be used as stable support for the powders produced according to the reaction we are proposing.

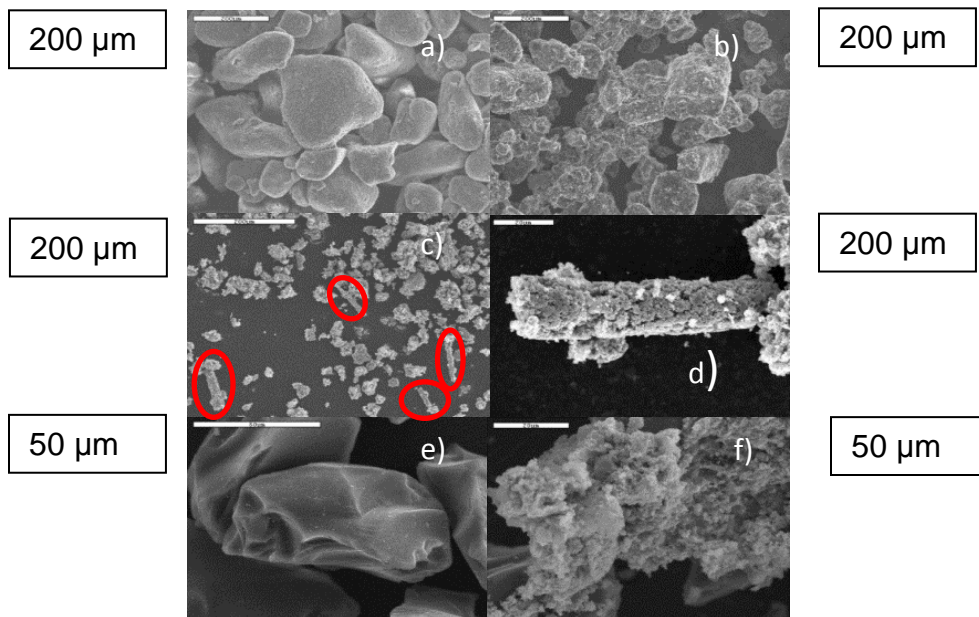


Figure 2-33. SEM images of the various powders: a) Sodium borohydride; b) Sodium borohydride + 5% NiBr<sub>2</sub> non hydrolyzed; c) and d) Overview of the hydrolyzed powders (in red ovals the elongated structures) and a single rod. e) Commercial silica gel mesh (80 – 100 mesh) and f) Supported NiB<sub>x</sub> on the silica gel surface.

The spectrum is shown in Figure 2-34 (without phase separation between NiB<sub>x</sub> and SiO<sub>2</sub>) and shows Ni, Si, and O peaks.

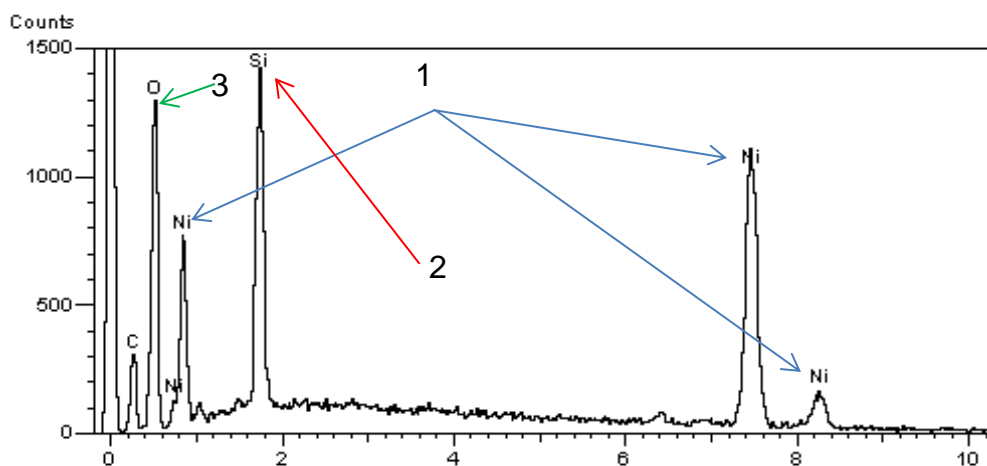


Figure 2-34. EDS spectroscopy of SiO<sub>2</sub> supported NiB<sub>x</sub>. The peaks of Ni (1) Si (2), and O (3) are clearly visible. The boron peak is usually difficult to see, and may also be hidden by the carbon peak which is enhanced because of the graphitic coating.

A carbon peak is found because of the graphitic coating used to make the samples conductive and because the sample holder was graphitic, too. A potential boron signal may therefore be hidden below the carbon peak.

## 2.4 Discussion of the Results

### 2.4.1 Thermal Analysis

The experimental results presented in preceding chapter were compared with those from the literature that refer to nickel borides prepared in aqueous solution and investigated by DSC.<sup>39</sup> Thermal analysis was used to investigate potential crystallization processes of the amorphous nickel boride powders. The composition of the nickel borides investigated by Wang et al.<sup>39</sup> was assumed to be 3:1 ( $\text{Ni}_3\text{B}$  stoichiometry). The DSC results revealed a rather exothermic crystallization peak at 614 K preceded by a structural rearrangement at 447 K (see Figure 2-37 for a reproduction of Wang et al.'s results).

This work was used as a benchmark to compare with our own results which turned out to show some similarities but also important differences.

Our DSC results on  $\text{NiB}_x$  revealed a peak around 650 K similar to that seen in  $\text{Ni}_3\text{B}$ <sup>39</sup> albeit broader and much less. However, several other features were observed in our experimental results that were not reported in the Wang et al.'s paper.<sup>39</sup>

The temperature range surveyed by Wang et al. ranged from room temperature (298K) to 900 K. Our data was collected up to 1300 K and revealed another relatively intense transition at 1000 K which would have escaped Wang et al.<sup>39</sup> When  $\text{NiB}_x$  was supported on silica, the transitions shifted to higher temperatures with the 1000 K transition demonstrating the larger shift when comparing the supported with the unsupported powders.

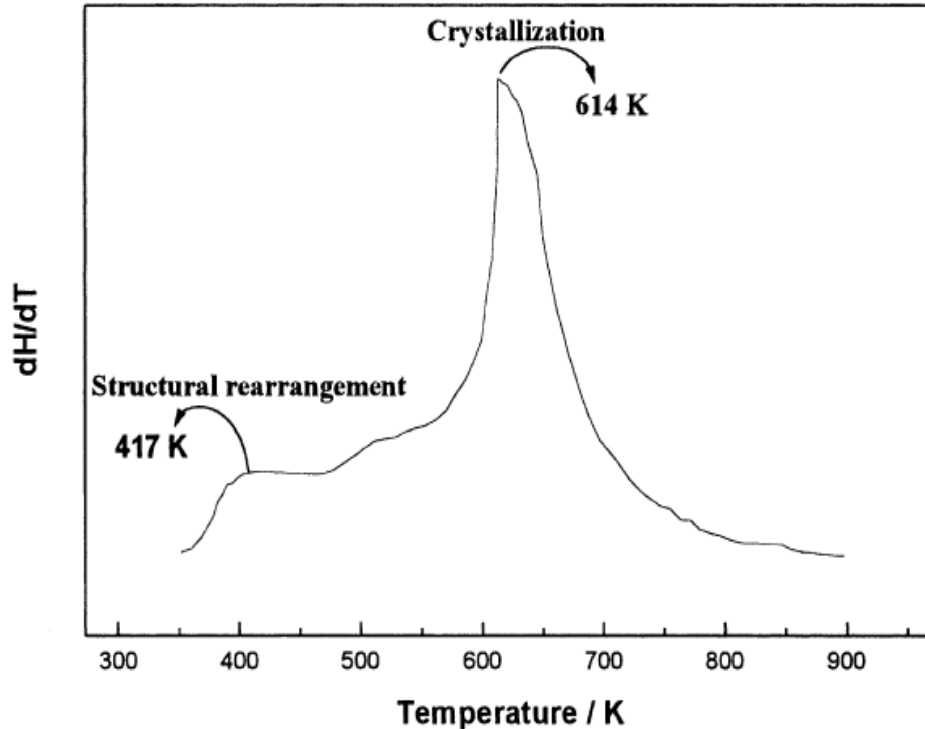


Figure 2-35. DSC thermogram of Ni<sub>3</sub>B. Reprinted by permission from Wang, M.; Li, H.; Wu, Y.; Zhang, J. *Mat. Lett.* **2003**, *57*, 2954. Copyright (2003) Elsevier

The rearrangement at 447 K found by Wang et al.<sup>39</sup> is not well described in their publication and lacks any structural details. We did not observe such a transition in our experiments. The high temperature peak has been investigated, and the annealing of the powders showed that this transformation can be attributed to some sort of crystallization (see Paragraph 2.3.4.2). However, it is still not clear which phases are crystallizing. However, since aging and air-handling showed the formation of nickel and nickel oxide, it is possible that some amorphous boron oxide is crystallizing at those temperatures, and so a consistent part of the pattern may be due to nickel, nickel oxide and boron oxide. Alternatively, nonetheless the care used in blowing Ar (99.9% purity grade) for 30' before, all the annealing time and 30' after the annealing experiment to purge the furnace from all the oxygen, the elements combined at high temperatures to form nickel borates (Ni<sub>3</sub>(BO<sub>3</sub>)<sub>2</sub>). Alternatively, the formation of the nickel borides with

NiB<sub>2</sub> stoichiometry might be proven through calculated structures which can be used as models for the refinement of the pattern.

However, the existence of these boron-rich content nickel boride phases is very difficult to achieve due to the ease of oxidation of these materials which in very little time can form other phases which are difficult to crystallize.

#### 2.4.2 FTIR

Our FTIR data was compared with the results of Molvinger<sup>77</sup> and Portehault.<sup>45</sup>

Results from Portehault and coworkers<sup>45</sup> are presented in Figure 2-36.

Experimental IR spectra were compared with several boron-based materials: amorphous boron (bulk), B<sub>2</sub>O<sub>3</sub>, and bulk B(OH)<sub>3</sub>, and the metal borides produced.

This paper was used as a benchmark to determine the vibrations due to the boron oxide and water present in the isolated powders. By comparison it becomes clear that after hydrolysis of the borohydride matrix our powders contain non-negligible quantities of boron oxide. This amorphous material may cover the actual active material which is consistent with our XPS and may explain part of our XRD results.

The experimental IR spectra for the nickel borides synthesized by Molvinger *et al.* are shown in Figure 2-37.<sup>77</sup>

The spectra show a peak at 1630 cm<sup>-1</sup> which is assigned by the authors to be due to water bending. The same peak is also found in the FTIR of Portehault<sup>45</sup> and in our own experimental data for NiB<sub>x</sub>. Two other bands are clearly visible at 1030 cm<sup>-1</sup> and at 1350 cm<sup>-1</sup>.

The 1030 cm<sup>-1</sup> band is very close to the one found in MgB<sub>2</sub> (due to unreacted crystalline boron) and crystalline boron at 1040 cm<sup>-1</sup>.<sup>91</sup> However this band is reported to

disappears upon rigorous elimination of crystallization waters from the precursor nickel salt by Molvinger et al., and therefore the band assignment is in doubt.<sup>77</sup>

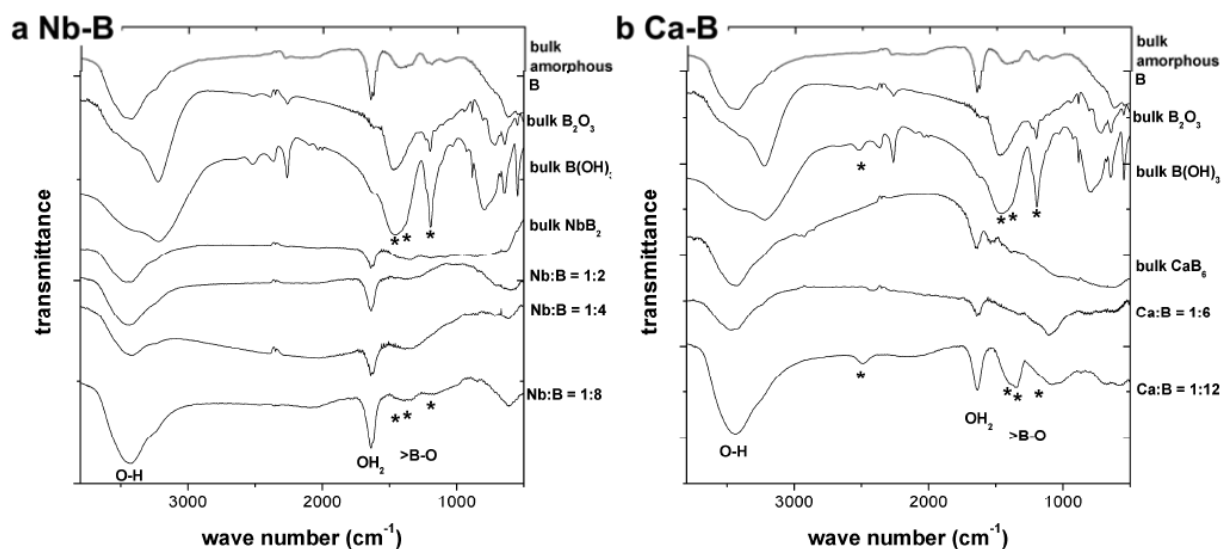


Figure 2-36. IR spectra of  $\text{NbB}_2$  and  $\text{CaB}_6$  microcrystalline borides. Reprinted by permission from Portehault, D.; Devi, S.; Beaunier, P.; Gervais, C.; Giordano, C.; Sanchez, C.; Antonietti, M. *Angew. Chem. Intl. Ed.* **2011**, *50*, 3262. Copyright (2011) Elsevier.

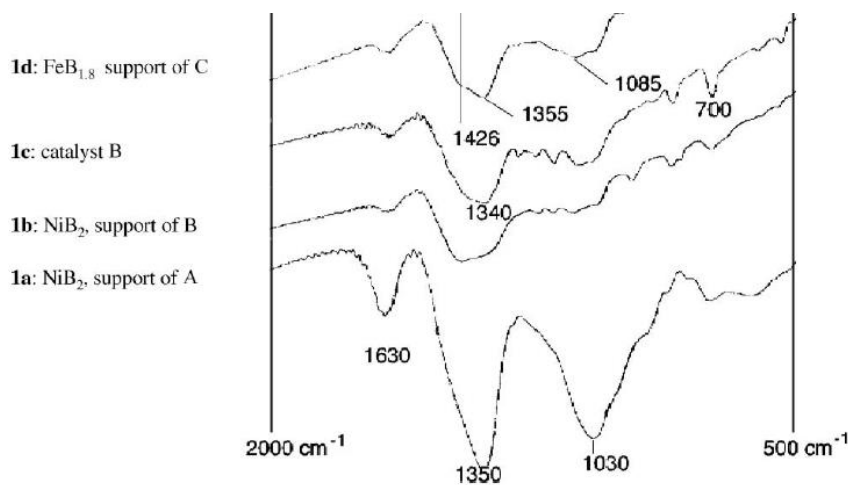


Figure 2-37. Experimental IR from Molvinger, K.; Lopez, M.; Court, J.; Chavant, P. Y. *Appl. Catal. A: Gen.* **2001**, *231*, 91. Reprinted by permission. Copyright (2001) Elsevier.

The  $1350\text{ cm}^{-1}$  band is assigned by the authors to a bidentate mononuclear  $\text{M-BH}_4$  complex (see Figure 2-38), but this assignment is questionable since B-H bands are

typically expected at  $1120\text{ cm}^{-1}$  and may be hidden under the broad band at  $1030\text{ cm}^{-1}$ . The B-H stretches, which for sodium borohydride fall in the range between  $2200$  and  $2400\text{ cm}^{-1}$  are not seen in fig. 2-37 because the cut-off limit of the spectra that are presented between  $500$  and  $2000\text{ cm}^{-1}$ .<sup>77</sup>

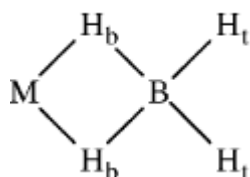


Figure 2-38. Mononuclear bidentate M-BH<sub>4</sub> complex. Reprinted by permission from Molvinger, K.; Lopez, M.; Court, J.; Chavant, P. Y. *Appl. Catal. A: Gen.* **2001**, 231, 91.

Experimental FTIR spectra of our powders are not conclusive, since the powders, upon annealing, show exactly the same peak positions as MgB<sub>2</sub> and KBr suggesting an impurity such as SO<sub>4</sub><sup>2-</sup> in the KBr matrix. It is not possible to distinguish between the vibration of the unknown powders and the impurities in the KBr matrix. This result makes it impossible to give a clear assignment of the absorption bands of the nickel borides in Figure 2-8. However, possible assignments can be predicted from calculated structures. The purpose of the calculated NiB<sub>3</sub> intensities served to understand if the powders might contain this particular compound, and as a benchmark in assigning boron-related vibrations. However, there was no experimental evidence for the presence or absence of NiB<sub>3</sub> in the FTIR spectra. The literature is also silent on the assignment of specific boron-boron stretch vibrations for NiB<sub>2</sub> compounds. The problem is compounded by the fact that these vibrational bands are quite broad and weak for other nickel borides.<sup>45,77</sup>

Comparison of the experimental FTIR spectra with those from Portehault et al.<sup>45</sup> gave us some limited insight on the interpretation of the vibrations in the supported nickel borides. Figure 2-39 reproduces the experimental FTIR from Portehault et al.'s paper.<sup>45</sup> The experimental FTIR spectrum of our supported powders show the same vibrations found for other supported metal borides in the literature.<sup>45</sup> The Si-O vibrations (around 1100 cm<sup>-1</sup>) and B-O stretches (around 1400 cm<sup>-1</sup>) are visible. The peak due to the water bending mode was also found around 1600 cm<sup>-1</sup>. It was not possible to detect the vibrations due to the B-O-Si stretching mode, which are expected around 700 cm<sup>-1</sup>, since the lower limit of detection of the instrument, in the mid-IR is 800 cm<sup>-1</sup>. However, it has not been possible to determine the B-O-Si stretching mode even in the far-IR, supporting and completing the FT-IR information, since the spectra in the far-IR did not show any particular peak (or band) in the same range. Annealed supported powders were not measured by FTIR since a clear phase separation was observed after annealing these samples.

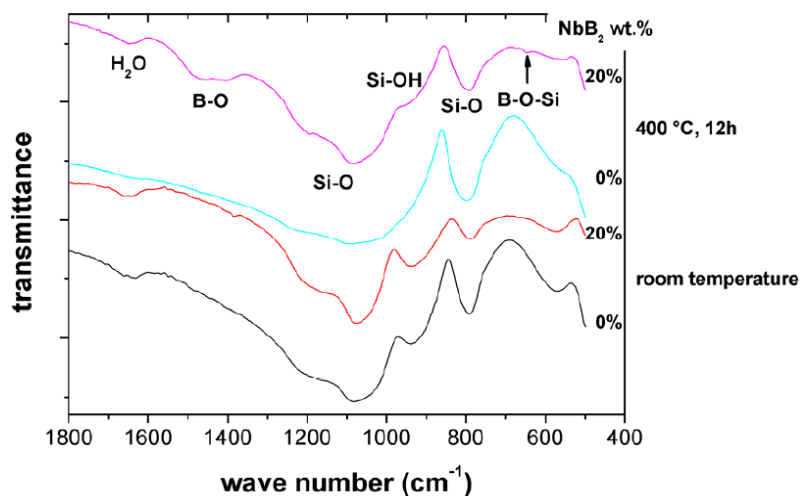


Figure 2-39. FTIR spectra of SiO<sub>2</sub> supported NbB<sub>2</sub> at room temperature and after annealing under Ar for 12 h. Reprinted by permission from Portehault, D.; Devi, S.; Beaunier, P.; Gervais, C.; Giordano, C.; Sanchez, C.; Antonietti, M. *Angew. Chem. Intl. Ed.* **2011**, *50*, 3262. Copyright (2011) Wiley.

### 2.4.3 XRD

XRD experimental data were compared with the data published by Wang et al.<sup>39</sup> Their study followed up on their thermal analysis by collecting XRD patterns at each step increasing the temperature by 20 K every 0.5 h under dry nitrogen atmosphere. Figure 2-40 reports their XRD patterns of the nickel borides from room temperature up to 633 K. The amorphous broad band which is seen at low temperatures in Figure 2-40 (a), is giving space to a more crystalline pattern which starts to show peaks at 553 K (Figure 2-40 c). In Figure 2-40 (d) the system is showing a large number of peaks, most of them at very low intensity which were attributed to a mixture of nickel borides of Ni<sub>3</sub>B and Ni<sub>2</sub>B stoichiometries. However, further annealing of the powders temperatures, higher than 573 K, demonstrated the formation of metallic nickel. To determine the fate of the boron, XPS experiment were performed, revealing oxidized boron in the powders.<sup>39</sup>

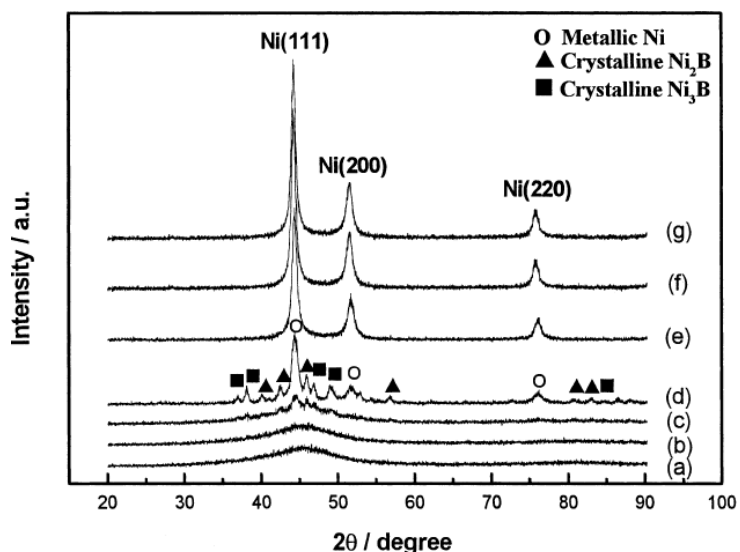


Figure 2-40. XRD patterns of nickel borides reprinted by permission from Wang, M.; Li, H.; Wu, Y.; Zhang, J. *Mat. Lett.* **2003**, *57*, 2954. Copyright Elsevier (2003). (a) to (g): XRD patterns for powders annealed at 513, 533, 553, 573, 593, 613, and 633 K under dry N<sub>2</sub> flow for 0.5 h per spectrum.

Our materials did not show this behavior which may be peculiar to  $\text{Ni}_2\text{B}$  and  $\text{Ni}_3\text{B}$  phases. However, a clear crystalline patterning upon heating the powder at 1100 K for 5 hours under  $\text{Ar(g)}$  was observed. At this point in time it is not possible to distinguish which of these peaks are due to nickel borides, since we don't have any structural file, even though we are looking for calculated ones. However, other phases which can also be present (nickel metal, boron oxide, nickel oxide) can be seen in a refinement. In this case, however, the refinement will be rather poor since some of the peaks cannot be revealed due to an incomplete model of the phases contained in the powders. In any case, even though the amorphous matrix was still present after annealing at 1100 K for 5 h under argon, it was much less pronounced. Aging of the samples and air-handling of the powders may have contributed to the formation of nickel and nickel oxide. This result may be comparable to those observed by Wang et al.<sup>39</sup> who noticed the formation of metallic nickel upon annealing under dry nitrogen atmosphere. However, even if the formation of nickel oxide can be more evident, thanks to the reaction of the powders with the air, it is still not clear how it is possible the formation of metallic nickel.

#### **2.4.4 XPS**

The XPS results were compared with literature data.<sup>50,80,101,103</sup> In these studies, nickel borides prepared from aqueous solutions were investigated with XPS. Both bulk material and nanoparticles were investigated. To determine the oxidation state of the nickel, experimental data were compared with Vedrine et al.<sup>103</sup>

The oldest XPS study on nickel borides was described by Okamoto et al.<sup>50</sup> They prepared a variety of metal borides and tested their surface composition by means of XPS. In this work, particular relevance is given to nickel borides which have been prepared from a number of nickel salts. Reaction products were distinguished according

to the solvent used in the preparation: catalysts synthesized from aqueous solution are labeled P-1, and those synthesized from 95% ethanol solutions are labeled P-2. All data are referenced to the C 1s peak which falls at 288.3 eV. Observed binding energies for B 1s were found at 192 and 188.2 eV. A third peak appeared at 199 eV. This latter peak was assumed to derive from chloride impurities in the sample. Boron lines were denoted B-I and B-II with no further explanation. Later on, these B-I and B-II lines were identified as oxidized boron and “elemental” boron by Schreifels et al.<sup>80</sup> Ni 2p<sub>3/2</sub> signals were found at 852 eV. They were further deconvoluted into contributions from nickel metal and nickel oxide. The nickel oxide electron binding energy was found to be 855.7 eV.<sup>50</sup> Figure 2-41 reports the spectra from Okamoto et al.<sup>50</sup> The B 1s and Ni 2p<sub>3/2</sub> lines are reported.

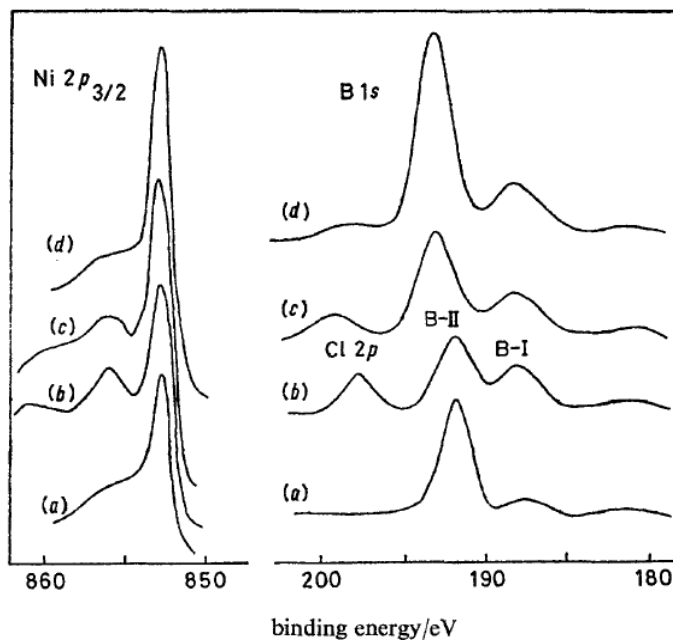


Figure 2-41. XPS spectra of Ni 2p<sub>3/2</sub> and B 1s for the nickel borides prepared from nickel acetate at 30°C, a) unwashed b) washed 3 times with water, and 3 times with 99% ethyl alcohol c) evacuated at 200°C for 1 h, d) evacuated at 400°C for 1 h. Reprinted by permission from Okamoto, Y.; Nitta, Y.; Imanaka, T. *Faraday Trans. 1* **1979**, 75, 2027. Copyright, Royal Society of Chemistry

The second work that has been used as a reference was carried out by Schreifels and coworkers<sup>80</sup> in an attempt to determine the surface composition of nickel borides with a Ni<sub>2</sub>B composition before and after the hydrogenation of organic compounds.

The main aim of this work was to understand surface modifications in terms of composition and area before and after hydrogenation of acrylonitrile.

Results of this work are again referenced to the C 1s peak at 285 eV.

Experimental lines of nickel and boron are reported in Table 2-5. Metallic nickel and nickel oxide was measured as the nickel references, and boron, sodium borohydride, boric acid, and borax were measured as the boron references. Experimental results were also compared with commercial Ni<sub>2</sub>B and Ni<sub>3</sub>B. Metallic nickel and nickel boride lines were found between 852.6 and 853.2 eV. Nickel oxide was observed at 852.6 eV. Boron lines ranged from 186.7 to 193.3eV.

Table 2-5. XPS B 1s and Ni 2p<sub>3/2</sub> line positions, as reported by Schreifels et al.<sup>80</sup>  
Adapted with permission. Copyright Elsevier (1980)

	B(1s)			Ni(2p <sub>3/2</sub> )
	Line 1 (eV)	Line 2 (eV)	Line 3 (eV)	
Standards				
B			186.7	
NaBH <sub>4</sub>	193.3 <sup>a</sup>	188.7		
H <sub>3</sub> BO <sub>3</sub>	193.2			
B <sub>2</sub> O <sub>3</sub>	193.3			
Na <sub>2</sub> B <sub>4</sub> O <sub>7</sub>	192.0			
Ni				852.6
NiO				856.2
NiB	193.7	189.1		853.4
Ni <sub>2</sub> B	194.3	190.1		852.6
Ni <sub>3</sub> B	192.1	187.6		853.2
Catalysts				
Ni <sub>2</sub> B P-1.00	192.3	187.9		852.0
Ni <sub>2</sub> B P-1.50 <sup>b</sup>	192.2	188.0		852.1
Ni <sub>2</sub> B P-1.50 <sup>c</sup>	193.5			852.9
Ni <sub>2</sub> B P-1.75	192.2	187.9		851.9
Ni <sub>2</sub> B P-2.00	193.0	187.8		852.0

<sup>a</sup> Initially weak, intensifies with X-ray exposure; <sup>b</sup> Atmospheric exposure followed by H<sub>2</sub> reduction at 400°C; <sup>c</sup> no atmospheric exposures.

The authors state:

“The relative intensity of the lines is also a measure of the thoroughness of the grinding process which leads to smaller particles, averaging the composition between bulk and surface. Lower binding energies are attributed to the boride species, while higher binding energy was attributed to superficial boron oxide species.”<sup>80</sup>

The bulk stoichiometry of the samples under study, in this work, was determined to be Ni:B = 2:1. Experimental XPS spectra from this work are shown in Figure 2-42.

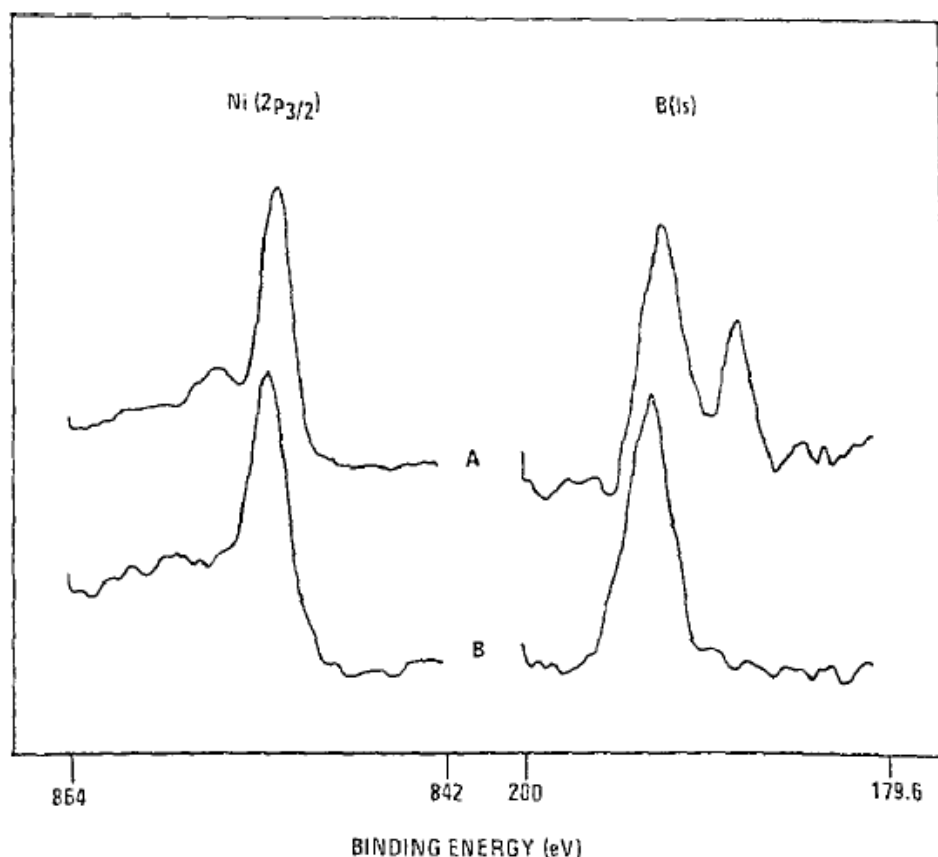


Figure 2-42. XPS spectra showing the Ni 2p<sub>3/2</sub> and B 1s lines observed by Schreifels, J. A.; Maybury, P. C.; Swartz, W. E. *J. Catalysis* **1980**, *65*, 195. Copyright Elsevier (1980). a) no atmospheric exposure b) after atmospheric exposure and followed by reduction with hydrogen at 400°C. Reprinted by permission.

The XPS technique is an inherently surface-sensitive method and scans only the first few atomic layers (approx. 5 to 10 Å deep). The cited publications assume a

homogeneous composition of the samples with very little differences between surface and bulk which may be questionable under normal atmospheric conditions.

No references were found for XPS studies on boron-rich nickel borides and we will use the published spectra to compare and distinguish our own experimental results.

Experimental spectra of the  $\text{NiB}_x$  powders show nickel peaks only in the region of 855 eV. This particular energy value corresponds to Ni(II) and is normally found for NiO.<sup>50,80,103</sup> X-ray diffraction indicated (see Paragraph 2.3.4.2) the presence of some nickel oxide in the powders. However, the nickel oxide phase was not the principal phase of the nickel borides samples, even after extended exposure to air. Of course, the grinding process using mortar and pestle in the presence of oxygen may have increased the amount of nickel oxide. While nickel oxide is clearly visible on the surface through the XPS spectra the X-ray diffraction data actually showed comparably larger amounts of nickel metal (see the Paragraph 2.3.4.3) in the samples. However, the only XPS peaks observed for nickel were the ones found in the nickel oxide range (855 eV). No signals were observed at 852 eV where the  $\text{Ni}^0$  lines are expected. This indicates a heterogeneous composition of nickel oxides on the surface with deposits of nickel metal (perhaps in the form of nanoparticulate metal deposits) in the bulk of the powder. Evidence for metallic nickel also comes from EPR spectra which demonstrate ferromagnetic resonance (see appendix Figure A-9).

The XPS experiments showed B 1s peaks at ~182 eV and 192 eV. The 182 eV value is anomalously low and has not been reported before in the literature. Comparing this result with those of the  $\text{MgB}_2$  B 1s lines, the peak position for the nickel borides appears shifted to lower binding energies by about 5 eV. The normal energy range, for

boron 1s peaks in nickel borides is between 4 and 5 eV.<sup>50,80</sup> A difference of 4.23 eV was found experimentally for commercial MgB<sub>2</sub>, but the two boron signals, in NiB<sub>x</sub> are separated by about 10 eV which is twice the reported energy difference for the boron peaks in nickel-rich nickel borides.<sup>50,80,101</sup> It is not clear what causes this behavior in the powders. The lack of signal at the Ni<sup>0</sup> line (852 eV) caused us think about an overlap of the nickel and nickel oxide signals. Perhaps that NiB<sub>x</sub> shows electronic back-donation from the boron framework to the metal framework, even if, up to now, no evidence has been found for such behavior. However, all the nickel rich phases never showed such behavior. On the other hand, similar behavior was predicted for the calculated NiB<sub>3</sub> structures.<sup>81</sup> Results from calculations are presented in Figure 2-43.

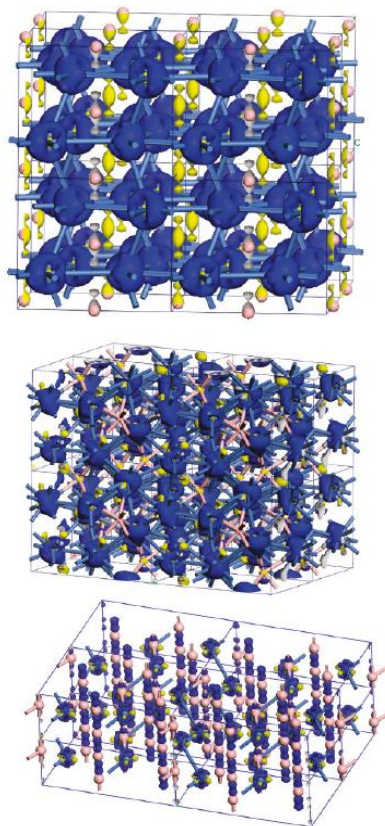


Figure 2-43. Electron density difference of Ni<sub>2</sub>B, Ni<sub>3</sub>B, and NiB<sub>3</sub>. Isodensity surfaces are at the following values: 0.012, 0.045, 0.045 and 0.040 electrons/Å<sup>3</sup>. Representing colors: charge depletion, yellow; charge accumulation, blue.

According to this hypothesis, the Ni<sup>0</sup> lines are shifted to 855 eV, i.e., about 3 eV higher compared to its usual position. Thus we would interpret the observed Ni lines not as due to nickel oxides but rather as a nickel compound bound to B atoms, potentially with a similar oxidation number of +2. On the other hand, the boron (B<sup>0</sup>) signal is found at lower energy of about 5 eV, compared to the usual B<sup>0</sup> line positions. The shift in energy for both elements is not the same, and therefore the hypothesis of electronic backdonation from boron framework to nickel framework still needs to be verified with additional experiments.

#### **2.4.5 Quantitative Elemental Analysis**

The elemental analysis of boron and nickel outlined in chapter 2-3 revealed an atomic ratio of B:Ni of approximately 2. This is expected if the formation of these nickel borides is passing through an initially slow formation of metastable metal borohydrides followed by a decay path to the metal borides (see Paragraph 2.1). Since no diboranes were observed in our experiments all the boron should be found in the solid material either in the form of nickel boride or unreacted borohydrides. The ICP-AES elemental analysis allowed us to confirm a specific ratio of B:Ni of 2.1.

The XRD patterns of the as-prepared powders and careful quantitative analysis of the left-over borohydride reactant suggested a 3.2 B:Ni ratio. It should be noted that this analysis is somewhat vague as it depends on the difficult quantitation of XRD patterns and the subtraction of relatively large numbers which necessarily incurs relative large errors. Nevertheless, it also confirms the fact that our powders contain a boron-rich nickel boride material. Further quantification of the metallic Ni in our samples may be appropriate since this may reveal yet a different stoichiometry of NiB<sub>x</sub> with  $x > 2$  depending on how much nickel is bound in the metallic state.

However, the relative amount of boron and nickel, clearly, is not necessarily giving the stoichiometry of the  $\text{NiB}_x$  molecule, since the powders may be affected by foreigner contaminants such as  $\text{Na}^+$  and  $\text{Br}^-$  which can still be present even after the hydrolysis performed to remove all the water-soluble contaminants ( $\text{NaBH}_4$  and  $\text{NaBr}$ ).

#### **2.4.6 Morphology of $\text{NiB}_x$**

Data from the microscopy studies were compared with earlier work by Birajdar et al.<sup>102</sup> and Portehault et al.<sup>45</sup> In particular the experimental EDXS spectra were compared with the reported ones.

The first study was intended to quantitatively reveal boron content using microscopy (TEM and SEM) on crystalline  $\text{MgB}_2$ . The aim of this paper was to analyze the response of boron atoms when performing energy dispersive spectroscopy, which is based on X-ray fluorescence.<sup>102</sup> The principal goal of Birajdar's paper was to obtain spectroscopic information from the response of the boron atoms, even though this element is a poor X-ray scatterer. The TEM and the B-related EDXS spectrum from Birajdar et al.<sup>102</sup> are presented in Figure 2-44.

It has been found that the X-ray fluorescence of boron atoms is very sensitive to the observation angle relative to the source.<sup>102</sup> Relatively accurate elemental quantities can be deduced using energy dispersive spectroscopy only for those surfaces normal to the electron beam.

Therefore, when the sample contains light elements of interest, such as boron, care needs to be taken in analyzing the spectra. The main problem is that techniques like EDXS are not quantitative in the determination of the atomic composition, even though a rough estimate might be obtained.

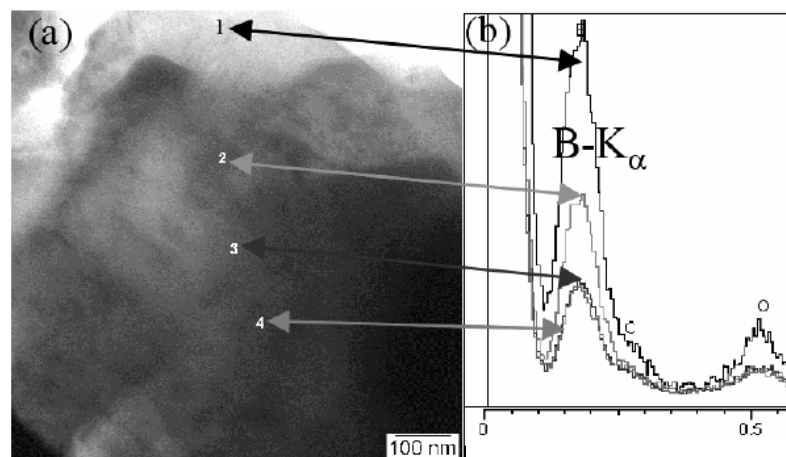


Figure 2-44. TEM image and relative EDXS for  $\text{MgB}_2$  reprinted by permission from B. Birajdar, N. Peranio, O. Eibl, *Microsc. Microanal.*, 2007 Vol.13 (Suppl. 3), 290 - 291. Copyright (2007) Cambridge Journals.

In another study, Portehault *et al.*<sup>45</sup> reported the EDXS spectrum obtained from their samples ( $\text{NbB}_2$ ) which is presented in Figure 2–45.

The spectrum showed an intense peak in the low energy range, which was attributed to boron species.

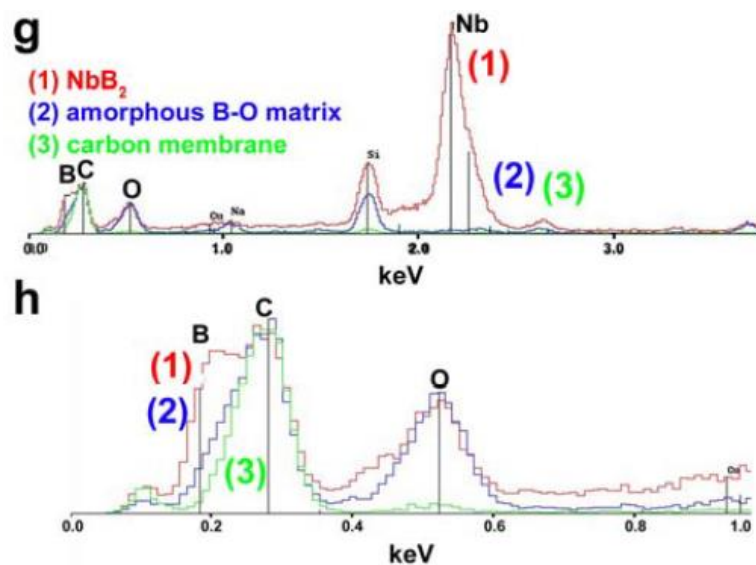


Figure 2-45. EDXS spectra reprinted by permission from Portehault, D.; Devi, S.; Beaunier, P.; Gervais, C.; Giordano, C.; Sanchez, C.; Antonietti, M. *Angew. Chem. Intl. Ed.* **2011**, *50*, 3262, Supporting Info. Copyright Wiley (2011).

Both references helped in the determination and assignment of the boron peak in our experimental spectra. In fact, comparing Figure 2-44 and Figure 2-45 with Figure 2-30, it appears clear that the boron content in our powders is higher than those in the literature. However, it should be noted that these intensities do not allow for a quantitative analysis. In fact, when analyzing the supported powders shown in Figure 2-31 the carbon and boron peaks are comparable. This means that in doing this experiment, the powder could have been contaminated by some carbon left from the solvent used to deposit it on the sample holder which was not completely evaporated. However, literature data show that EDXS performed on light elements such as B is rather poor when it is time to obtain quantitative data.

While it is not clear whether our sample contains a homogeneous  $\text{NiB}_2$  phase and the possibility is still open that higher B:Ni ratios may be present within the actual nickel boride contained in our powders, our results confirm the initial hypothesis that milling of the solid reactants nickel bromide and sodium borohydride will form and opens up a facile route to boron-rich nickel borides. However, elemental boron could not be directly detected nonetheless the extensive efforts, and the various analytical techniques used. It is mainly due to intrinsic difficulty to find elemental boron. In fact 1) the ICP-AES has given the total amount of boron per gram of substance versus the total amount of nickel per gram of substance. However it does not specify the oxidation state of the element; 2) IR did not reveal any particular boron vibration; 3) XPS revealed an anomalous peak which is found at energies that are too low as compared with data regarding elemental boron.<sup>50,80</sup>

## CHAPTER 3 CATALYSIS OF NICKEL BORIDES

### 3.1 Experimental Results

It should be noted that experiments described in this chapter showed that the nickel borides are not catalysts in the narrow sense since they participate in the reaction and may not be fully recovered after a cycle. Their mode of action is more in line with calling them reaction promoters. Nevertheless, the term “catalyst” will be used in this chapter repeatedly and is meant in a wider sense that includes “promoters.”

Hydrolysis of highly alkaline solutions of sodium borohydride was performed using both supported and non-supported amorphous  $\text{NiB}_x$ . The active material is assumed to be a nickel boride with a stoichiometry of  $\text{NiB}_2$  based on elemental analysis described in chapter 2. of the kinetics of hydrogen evolution from borohydride at pH ~14.00 was studied in the presence and absence of the nickel boride material. Both the supported and unsupported nickel boride were used. Reactions were conducted at room temperature and pressure. The volumes of the evolved hydrogen were determined by a Torricellian barometer described in Figure 2-1.

Experiments were performed at room temperature as well as at elevated temperatures in order to obtain information about the activation energy for the reaction. The temperature of the reaction vessel was controlled by a mineral oil bath and a thermometer to measure the temperature to  $\pm 0.1^\circ\text{C}$ .

Reactions were performed using about 1.5 mmol of sodium borohydride for each trial. Fresh 1 M NaOH solutions were prepared for each trial, dissolving 4.0 grams of NaOH pellets (Fisher) in 100 mL of Nano Pure Water (Barnstead,  $18.2 \text{ M}\Omega \cdot \text{cm}^{-1}$ ). The amounts of nickel borides used were 0.10 grams of the unsupported and 1.0 g of the

supported powders which allowed comparison of the effect maintaining a comparable activity of the mediating material.

Sodium borohydride and the mediating material were placed in a vacuum flask equipped with a magnetic stirrer. The flask was sealed with rubber septa and connected to the barometer. A timer with precision of  $\pm 1$  sec was used for reading the time. 10 ml of the 1 M sodium hydroxide solution where inserted into the vessel using a syringe penetrating the rubber septum and simultaneously starting the timer. This allowed the measurement of evolved hydrogen volume with time elapsed.

Figure 3-1 represents the kinetics of the hydrogen evolution from three reactions.

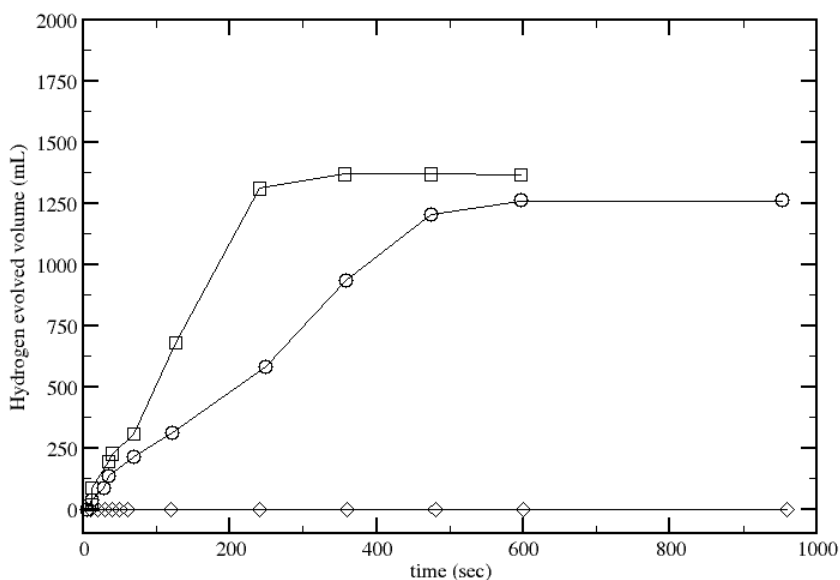


Figure 3-1. Kinetics of hydrogen evolution for various reactions. Diamonds: not catalyzed. Circles: supported catalyst. Squares: Unsupported catalyst.

Mediated reactions are rather fast, evolving almost all the hydrogen (88%) from the solutions within 20 minutes. In comparison the non-catalyzed reaction (control) does not lead to any observable hydrogen evolution in the same time frame under the conditions of pH, temperature, and pressure used. Table 3-1 reports the relative yields

of hydrogen evolution. The fundamental reaction taking place consumes sodium borohydride according to Equation 3-1:



Table 3-1. %-yield of hydrogen evolution from catalyzed hydrolysis of sodium borohydride: NC stands for Non-Catalyzed, UP stands for Unsupported Powder and SC stands for Supported Powder (mediated reactions).

	NaBH <sub>4</sub> (mmol)	Theo H <sub>2</sub> amt. (mmol)	Exp. H <sub>2</sub> amt. (mmol)	T (K)	%yield
NC	1.70	6.80	0	30	0
NC	1.66	6.64	0.03	40	0.6
NC	1.69	6.76	0.6	60	8.9
NC	1.67	6.68	0.81	85	12.1
UP	1.64	6.56	6.25	30	95.3
UP	1.64	6.56	5.95	40	90.7
UP	1.64	6.56	5.66	60	86.3
UP	1.66	6.64	5.35	85	80.7
SP	1.65	6.60	5.24	30	79.4
SP	1.67	6.68	5.59	40	83.7
SP	1.65	6.60	4.91	60	74.3
SP	1.67	6.68	4.83	85	72.2

Additional studies were performed to determine the stability of the powders after successive cycles of hydrogen evolution.

The surface area of the catalytic materials was determined through BET (Brunauer-Emmett-Teller) adsorption isotherm experiments. This technique uses the adsorption and desorption of N<sub>2</sub> on solid materials at 77 K and its theory is well described in the literature.<sup>104</sup> BET analysis showed a high surface area of 146 m<sup>2</sup>/g for the 1:10 supported powders. However, the surface area degrades rapidly upon repeated catalytic cycles. In Figure 3-2 the surface areas of both the supported and unsupported powders are plotted against catalytic cycles. In fact, after only 3 catalytic

cycles the surface of the supported powder was degraded from a high of  $146 \text{ m}^2\text{g}^{-1}$  to just  $16 \text{ m}^2\text{g}^{-1}$ .

Analogous results were found for, the unsupported powder, whose surface degraded from  $11.25 \text{ m}^2\text{g}^{-1}$  to  $0.67 \text{ m}^2\text{g}^{-1}$  after only one cycle of hydrogen evolution.

Kinetic cycles and the BET surface area versus number of cycles are shown in Figures 3-2 and 3-3.

Kinetic analysis of the reaction using the supported catalyst showed fast evolution during the first cycle reaching the end-point of hydrogen evolution after just 5 minutes. The second kinetic cycle already showed a much slower hydrogen evolution with the end-point apparently still not reached after 1 h. In the third cycle the powder is almost inert toward the solution.

This result shows that it is questionable whether the  $\text{NiB}_x$  materials are true catalysts since they lose their activity too quickly.

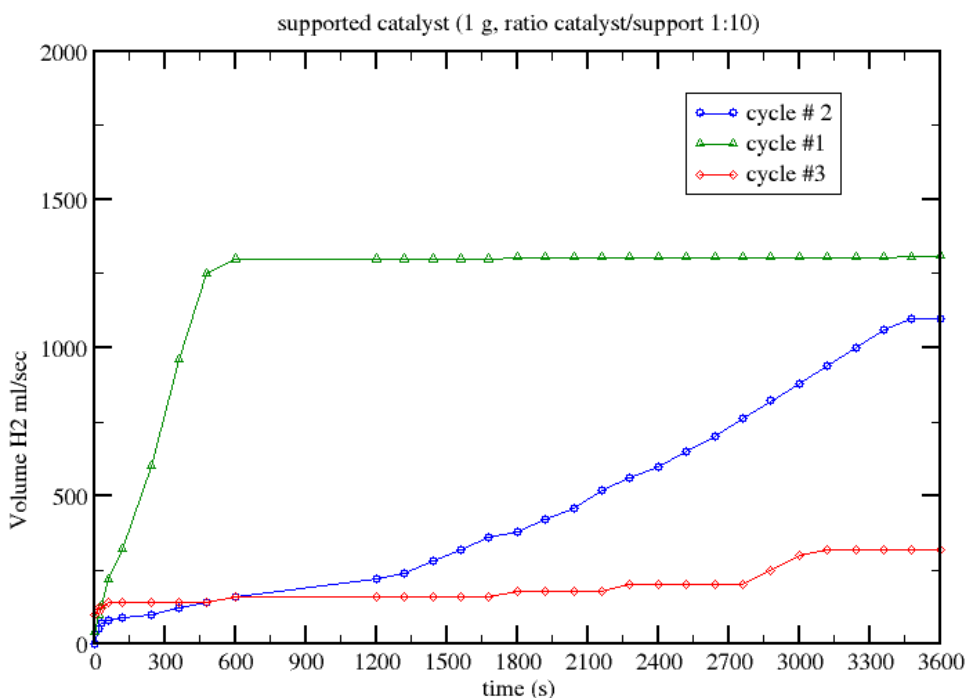


Figure 3-2. Kinetics of hydrogen evolution during different catalytic cycles.

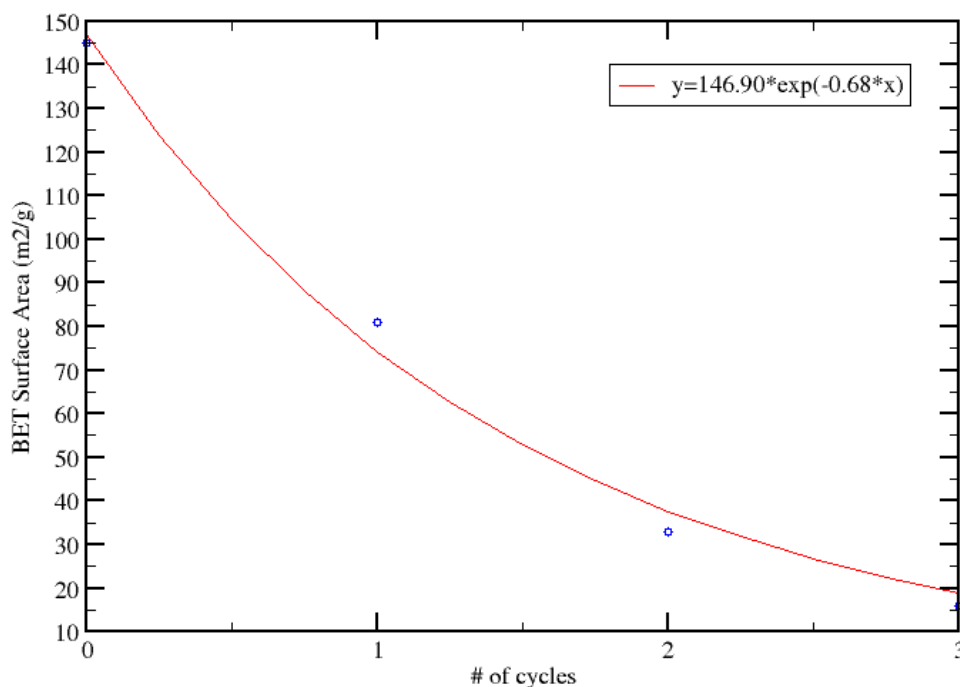


Figure 3-3. Surface area versus number of cycles of the supported material. The red line represents an exponential fit curve of the surface area to guide the eye. However, this does not mean that the surface area decays in an exponential fashion.

Results for the unsupported catalyst are shown in Figures 3-4 and 3-5.

In the literature, many nickel borides have been cycled for more than 200 times.<sup>6</sup> Unfortunately, no elemental analysis was performed after the cycles of hydrogen evolution to determine the composition, structure, and quantity of the nickel boride before and after the reaction which would allow to verify if the powders are true catalysts. It is clear that either the NiB<sub>x</sub> gets poisoned rather quickly or there is a concurrent loss of the active ingredient which leads to loss of activity during subsequent cycles.

For this reason we may consider the material as an additive which promotes the hydrogen evolution through hydrolysis of alkaline solutions of sodium borohydride.

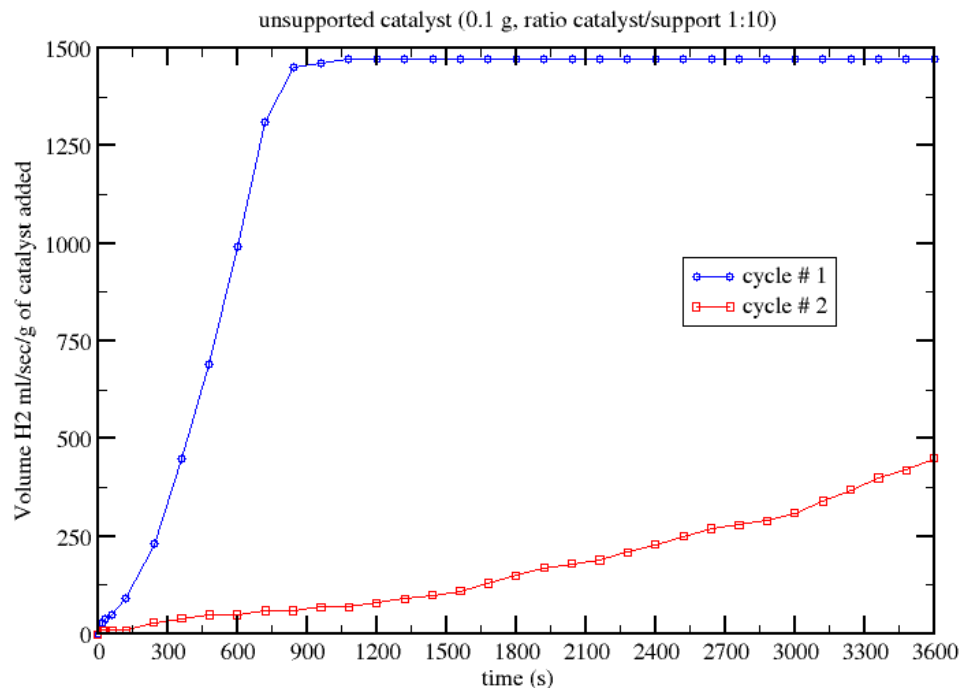


Figure 3-4. Kinetics of the unsupported catalyst during successive cycles.

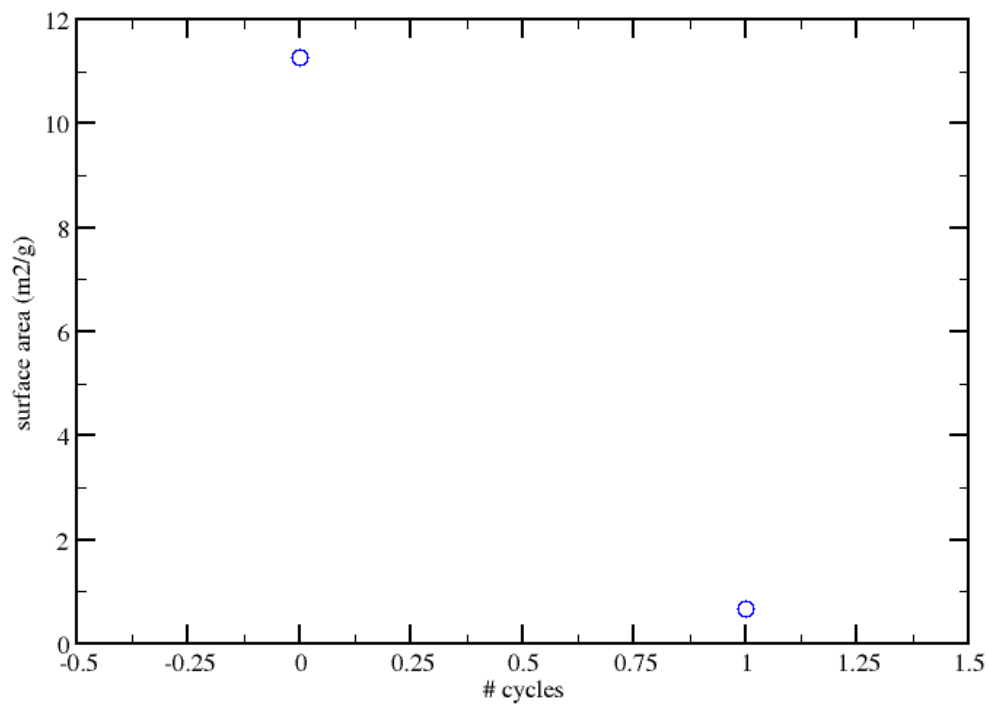


Figure 3-5. Decay of the surface area for the unsupported catalyst after successive cycles.

The observed fast breakdown of the sample activity suggests the presence of side reactions during catalysis. One can test this by analyzing the products. With regards to this question the literature simply implies that all catalyzed reactions of this type yield  $\text{NaBO}_2$  as the only product.<sup>6-8,39,40</sup> However, no experimental analysis has been published on the structure/composition of the products of reaction. Analysis of the products is not only important for the determination of their composition which can prove if the material used is a true catalyst or just a promoter of the reaction, but also in the formulation of a reaction mechanism.

In Paragraph 3.2 we will explore the energetics of the reactions, both the supported and unsupported nickel boride-mediated reactions and the non-mediated reactions.

### 3.2 Energetics of the Reactions

The apparent activation energies of the reactions are described in this chapter.

Temperature-dependent hydrogen evolution was carried out at 30°C, 40°C, 60°C, and 85°C.

The results are summarized in Figure 3-6.

The simplest model that can describe the linear increase of hydrogen evolution is a 0<sup>th</sup> order reaction. In this case the increment of the hydrogen concentration with time ( $\frac{\partial[H_2]}{\partial t}$ ) is equal to the rate constant, since the initial concentration of gas is  $[P]_0 = 0$ .

$$\frac{\partial[H_2]}{\partial t} = k \quad (3-2)$$

The reaction constant, obtained through the initial velocities method, i.e., through linear regression of the hydrogen evolution curve, has the dimension of mL/s. This has

to be converted to concentration units assuming the hydrogen gas to behave as an ideal gas:

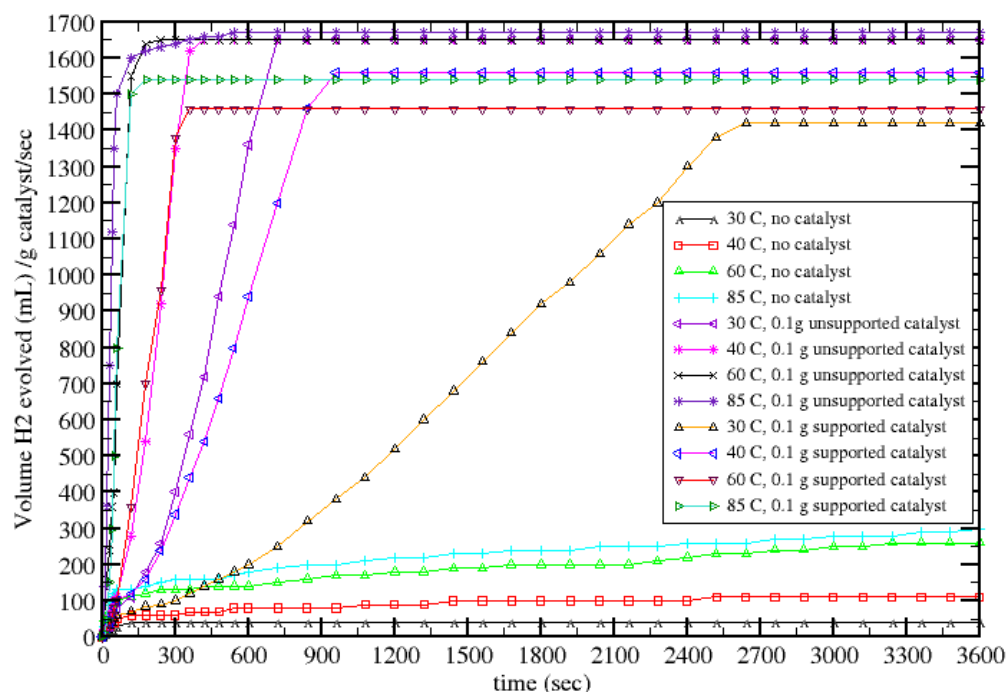


Figure 3-6. Kinetics of the reactions at 30°C, 40°C, 60°C, and 85°C for uncatalyzed reactions and reactions catalyzed with the supported and unsupported catalyst.

$$P^*V = nRT \quad (3-3)$$

Where  $P^*$  is the external pressure corrected by the vapor pressure at room temperature.  $T$  is the temperature of the hydrogen evolution reaction, and  $V$  is the observed volume. Rearranging the equation yields:

$$\frac{P^*V}{RT} = n_{H_2} \quad (3-4)$$

The kinetic constants were, then converted, with units of mol/L-s, (dividing the moles of hydrogen so obtained, by the volume of water used for the hydrolysis, which was held constant at 10 mL for each trial, and neglecting the amount reacted) which were needed for 0<sup>th</sup> order reaction. The kinetic constants and relative errors are shown

in Table 3-2. Errors have been calculated using error propagation, assuming that the variations due to the atmospheric pressure and the water vapor pressure are negligible with respect to the instrumental errors (temperature, volume). Although this is a rather cursory way to obtain activation energies for the reactions it allows us at least in principle to compare the activities of the supported and unsupported catalysts using an apparent activation energy.

Table 3-2. Temperatures and constants for the three sets of reactions

$T$ (K)	$K_{NC}$ (mol/L·s)	$K_{SP}$ (mol/L·s)	$K_{UP}$ (mol/L·s)
303.15	$(8 \pm 1) \cdot 10^{-6(1)}$	$(2.53 \pm 0.03) \cdot 10^{-4}$	$(1.14 \pm 0.01) \cdot 10^{-3}$
313.15	$(1.6 \pm 0.1) \cdot 10^{-5}$	$(8.40 \pm 0.08) \cdot 10^{-4}$	$(2.07 \pm 0.02) \cdot 10^{-3}$
333.15	$(3.5 \pm 0.8) \cdot 10^{-4}$	$(1.93 \pm 0.03) \cdot 10^{-3}$	$(5.08 \pm 0.08) \cdot 10^{-3}$
358.15	$(1.3 \pm 0.3) \cdot 10^{-3}$	$(5.08 \pm 0.08) \cdot 10^{-3}$	$(1.13 \pm 0.03) \cdot 10^{-2}$

However, 0<sup>th</sup> order kinetic reactions imply that the reaction rate constant is independent of reactant concentration. According to Retnamma, Novais and Rangel, the reaction seems not to follow 0<sup>th</sup> order reactions, because the different concentrations of sodium borohydride (especially in highly concentrated solutions) alter the rates of the reactions, altering the ionic strength effects. However, many papers reported 0<sup>th</sup> order reaction for catalyzed reactions.<sup>20</sup>

Activation energies were calculated using the Arrhenius equation:

$$k = Ae^{\frac{-E_a}{RT}} \quad (3-5)$$

The Arrhenius model is the simplest model able to explain the temperature dependence of the rate constants. The pre-exponential factor, A, gives an indication of

<sup>1</sup> This value has been estimated since we could not use the initial rates method to determine this constant. The rule of thumb used is for a reaction rate which doubles every 10 K under same external conditions.

the frequency of favorable collisions between the atoms (or molecules) forming products.  $E_a$  represents the energy barrier that the reactants have to overcome to form products. Generally, experimental values are plotted as the natural logarithm of  $k$  versus the inverse temperature,  $1/T$  (temperature units is K), the so-called Arrhenius plot. The activation energy can be obtained through a linear regression of the experimental points in this representation. The experimental results are shown in Figure 3-8 and give the following activation energies:  $88 \pm 12$  kJ/mol for the non-catalyzed reaction;  $46 \pm 7$  kJ/mol for the reaction conducted in the presence of the supported powder and  $38 \pm 2$  kJ/mol for the reaction conducted in the presence of the unsupported powder.

However, due to the limited amount of experimental points which can be collected, through this experiment, the assumption that the points can be linearly fitted may not be real, since errors can be very high, as it seems to be the case for the nickel borides mediated – reactions. The errors related to the calculation of activation energies, seem to be high: absolute errors, (calculated assuming Arrhenius behavior of the reaction) are between 5 and 15%. This may be due to the simplicity of the model used to fit the kinetic curves or to the fact that the calculus of the energy was not averaged across a sufficient number of experiments. One hypothesis that can be drawn is that the reactions are not catalyzed by nickel borides. In fact, it may be that these compounds react releasing gradually all the boron, until they remain as amorphous nickel, in which case the curves may be fit assuming heterogeneous catalysis over a rough surface.

However, it seems that the error from the reaction mediated by the unsupported powders (5%) is smaller as compared with the one calculated for the same reaction mediated by the supported powders (13%). The non-catalyzed reaction, however,

shows the highest error (15%) because, under the condition imposed, clearly the sodium borohydride hydrolysis presents extreme difficulty to proceed.

Despite of the errors in the calculations of the activation energies, the simple Arrhenius model gives a rough idea about the energies which are involved in the heterogeneous catalysis of sodium borohydride.

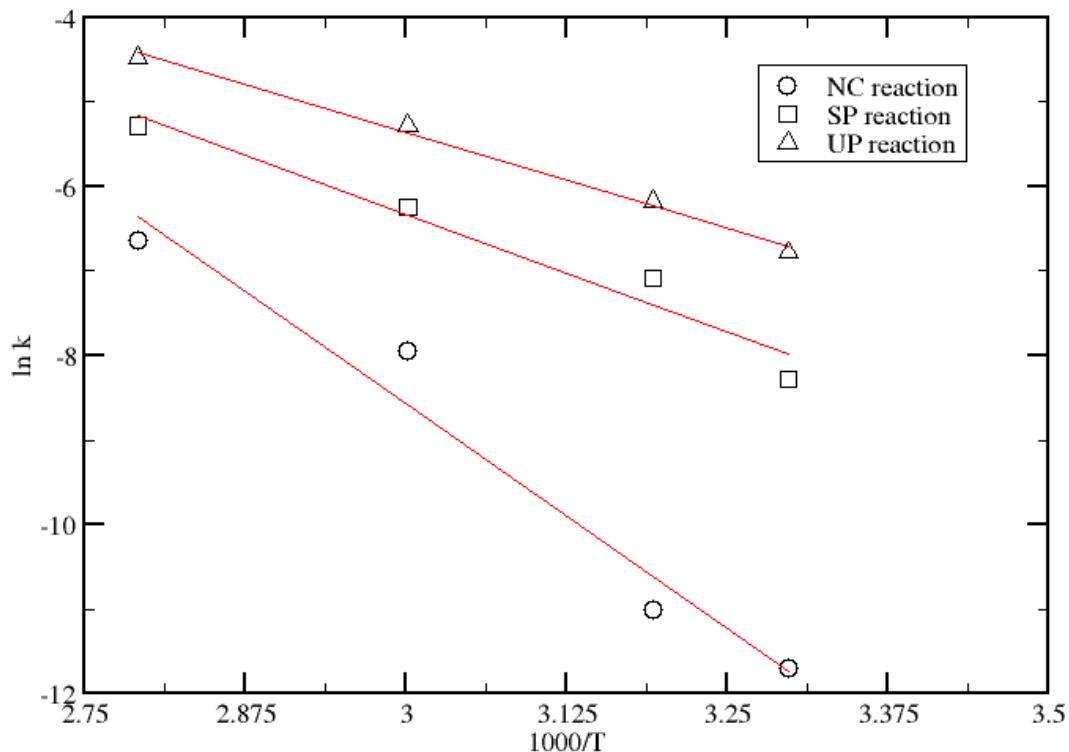


Figure 3-7. Arrhenius plots for the non-catalyzed (circles), for the unsupported powder (triangles), and for the supported powder reactions (squares).

A better model for the determination of activation energies is described by the Activated Complex Theory model applied to surface reactions.<sup>105</sup> This model works best for gase phase reactions which are catalyzed on metal surfaces. The simplest model described by



is valid for a gas-solid reaction. The Activated Complex Theory describes the kinetics on the basis of the partition functions for the reactants and the activated complex. This model, which is more complex, gives a clearer picture at each stage of the reaction. This is achieved using the partition function for each of the reactants and for the transition state. Therefore, for the use of this theory, is necessary to start from a model reaction. In literature, for this particular type of reaction, the bare non-catalyzed hydrolysis of sodium borohydride is reported.<sup>7,8,15-20,79</sup>

For a generic reaction:



with kinetic constants  $k_1$  for the equilibrium forward reaction,  $k_{-1}$  for the equilibrium reverse reaction and  $k_2$  for the decay of the transition state, the overall rate of reaction will be given by:

$$\frac{\partial[\text{products}]}{\partial t} = k_2[AB]^\ddagger = k_2 \frac{k_1}{k_{-1}+k_2} [A][B] \approx k_2 \frac{k_1}{k_{-1}} [A][B]^\ddagger \quad (3-8)$$

Since the ratio  $k_1/k_{-1}$  is equal to the equilibrium constant, and the equilibrium constant can be written in terms of the partition functions of reactants and the transition state, the rate of the reaction becomes:

$$\frac{\partial[\text{products}]}{\partial t} = k_2 \frac{q^\ddagger}{q_A q_B} e^{\frac{-\epsilon^*}{kT}} [A][B] \quad (3-9)$$

The Activated Complex Theory can also be applied to heterogeneous catalysis. However, the partition functions for species on the surface of the catalyst needs to be given per unit surface area instead of unit volume. The equation for the gaseous-solid catalyzed reaction constants then becomes:

$$k = \frac{KT}{h} \frac{q^\ddagger'}{q_g q_s} e^{\frac{-\epsilon^*}{kT}} \quad (3-10)$$

In this equation, only  $q_g$ , which is the partition function of the gas, is given per unit volume of gas. The other partition functions are given per unit surface area. This model is effective in describing the thermal behavior of the kinetic constants. However, this model, in order to work properly, needs a well-known mechanism of the reaction. According to Retnamma, Novais, and Rangel,<sup>20</sup> several mechanisms based on different models have been proposed. However, no agreement on the reaction mechanism has been established to date. Furthermore, all the reactions are based on the basic hydrolysis of sodium borohydride, which is very well known.<sup>20</sup> Therefore, a rigorous calculation of the activation energies needs an improved model of catalyzed (or promoted) hydrolysis by nickel borides. In literature it is implied that nickel borides are assumed to be catalyst. However there is not a definite proof of this assumption. In fact, the determination of an unambiguously accepted reaction mechanism responding to well-defined rate law is still missing. Many authors have used several kinetic laws to fit experimental data: it seems that, in dependence of the model chosen, there is always good agreement between the fitting equation and experimental data.<sup>20</sup> However, this ambiguous result implies that the kinetic constants values will be strongly dependent from the rate law and the model used to calculate them. A chemical analysis of the products of reaction is very important in that the main products may not be  $\text{NaBO}_2$  and  $\text{H}_2$ .

The reactions we tested seem to show significant improvement over the non-catalyzed reaction of hydrolysis of sodium borohydride. The apparent activation energies showed by the Arrhenius analysis for the catalyzed reactions are 40 and 50 kJ/mol lower, respectively for the supported and unsupported nickel borides, and the

relative change between catalyzed reactions in activation energies between the supported nickel borides versus the non-supported nickel boride seems not to be very big (about 8 kJ/mol difference). However, it seems that the supported nickel boride breaks down in a slower pace than the unsupported, as the plots of surface area versus the hydrogen evolution cycles show. In fact the activity of the non-supported nickel boride in the hydrogen evolution was lost after the first use, while the activity of the supported nickel borides was lost after 3 cycles. (3 times more use of the supported versus the unsupported nickel borides).

### **3.3 Identification of Reaction Products**

In order to identify the reaction products they first have to be precipitated from the solution. The following procedure was therefore implemented: 1) centrifugation at 14800 rpm for 5 minutes of the suspension after the reaction has completed; 2) solution pH was adjusted to between 8 and 9 using a few drops of concentrated HCl; 3) water was removed using a rotating evaporator leaving the solid salts as a microcrystalline white residue behind. This powder contained borates and NaCl as the main reaction products. However, the supernatant was not analyzed because of the tiny amount left after the reaction. In fact, BET results showed that, after few tries, an accurate result could not have been reached, since the powder left over from the reaction was so little that an accurate result could not be achieved. The dried powder was further characterized using FTIR spectroscopy, XRD diffraction patterns together with Rietveld refinement.

The FTIR of the powders revealed a well-defined set of vibrational bands for the reaction products with the unsupported and supported catalyst as shown in Figures 3-8 and 3-9.

There is a remarkable difference between the vibrations in the lower frequency region of the spectra between the products of the two reactions. They don't appear to be the same. This might be due to there being more than one possible borate compound produced.

In order to further investigate the difference in the two reaction products we performed XRD and Rietveld refinement.

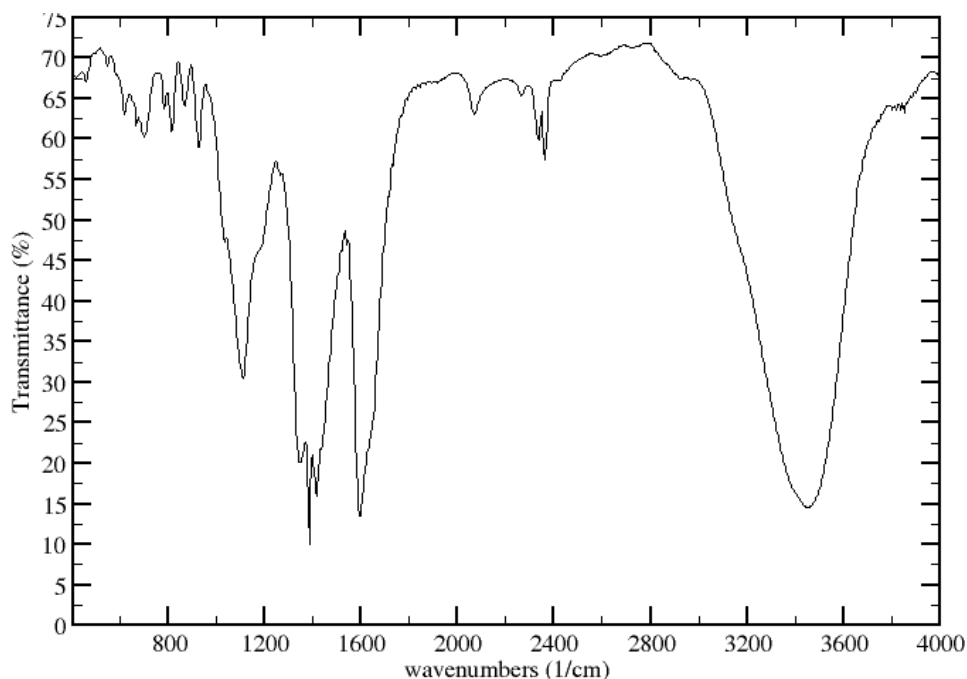


Figure 3-8. FTIR spectrum of the reaction products using the unsupported catalyst.

Figure 3-10 shows the XRD patterns of the reaction products. For comparison the pattern of commercial NaCl shown as well since it is one of the expected products.

These spectra, obtained from a Thermo Nicolet FT-IR spectrometer, courtesy of Dr. Christou, University of Florida, show several differences, which lead to different composition of the powder. However, the spectrum of the supported powders seem slightly more resolved than the one obtained from unsupported powders and showing also several vibrations in the range  $900\text{-}1300\text{ cm}^{-1}$ .

The patterns are again shown in  $d$ -spacing in order to directly show the observed distances between crystal planes.

For quantitative data and in an attempt to determine the composition of the products, we performed Rietveld refinement on the XRD patterns.

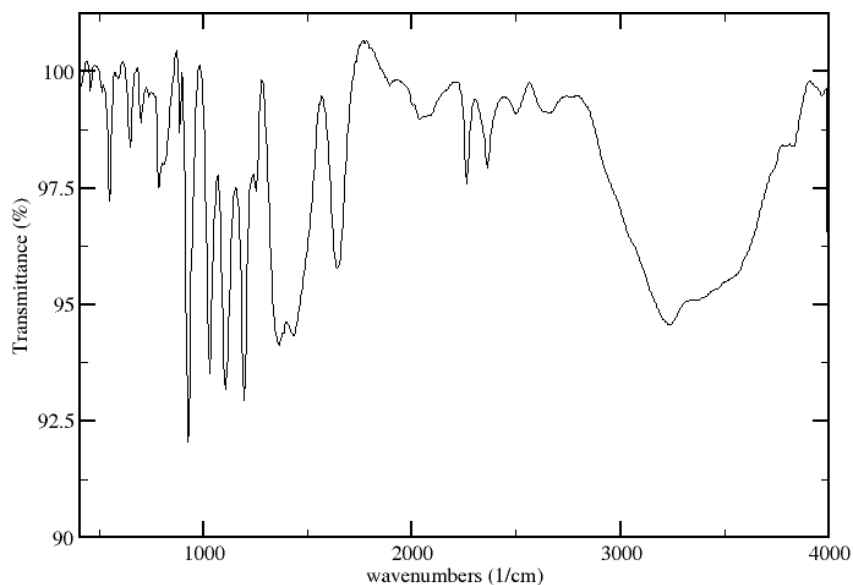


Figure 3-9. FTIR spectrum of the reaction products using the supported catalyst.

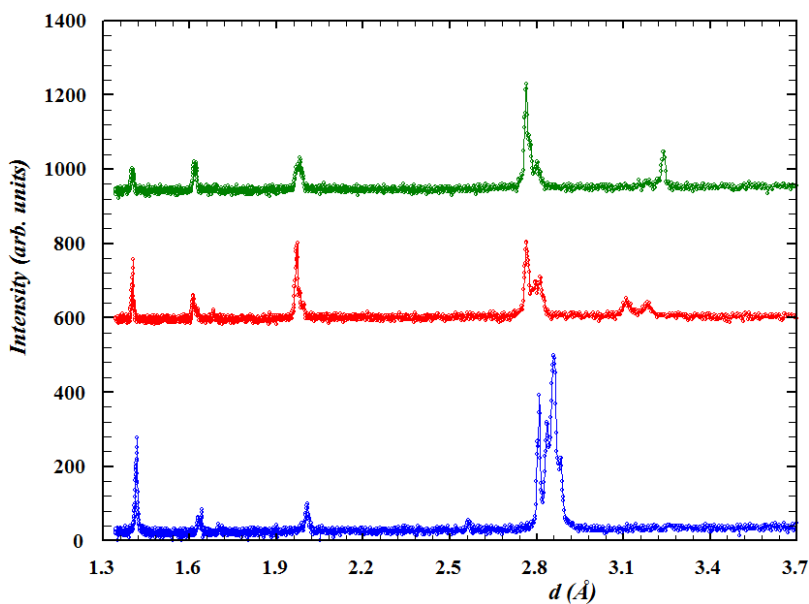


Figure 3-10. XRD patterns of the products from the catalyzed reactions. Blue: Crystalline NaCl. Red: Reaction products using the supported catalyst. Green: Reaction products using the unsupported catalyst.

The results are shown in Figures 3-13 and 3-14.

While the refinement was not perfect the results indicate that the relative compositions of the two powders are different. In fact, in the case of the reaction using the supported catalyst  $\text{NaBO}_2$  was the major boron containing crystalline compound. In the other case it was  $\text{Na}_3\text{BO}_3$ . The peaks in the residuals show that other unknown crystalline compounds are present, too.

In literature, kinetic data have been analyzed hypothesizing the reaction mechanisms (and products) of the hydrolysis of sodium borohydride alone. However, these data have been fitted using different kinetic laws.<sup>20</sup>

However, this clearly shows that the bare hydrolysis of sodium borohydride is a poor model for the analysis of kinetic data, for the determination of transition states and identification of reaction products.

In fact, the heterogeneity of the activation energies values calculated, which is strongly dependent from the rate law chosen in analyzing the data, proves the inconsistency of the model itself.

Furthermore, it is very difficult to establish a relationship between the activation energies for reactions catalyzed by nickel borides, or catalyzed by other catalysts and non-catalyzed reactions, since activation energies values are sometimes dependent from the concentration of the catalyst itself. In fact, to accurately calculate the activation energies of catalyzed reactions, sometimes, the concentration of the catalyst needs to be taken into account.<sup>10,20</sup>

A more complete elemental analysis of the “catalyst”, coupled with surface area analyses, before and after cycling the catalytic (promoting) material, need to be done.

Furthermore, these results prove undoubtedly that the initial model needs to be improved, determining the reaction products and, in parallel, proposing reaction mechanisms to hypothesize (and verify) transition state(s) of the “catalyzed” reactions, otherwise will be very difficult to accurately and univocally determine activation energies for this process, and compare the values using different models or rate laws.

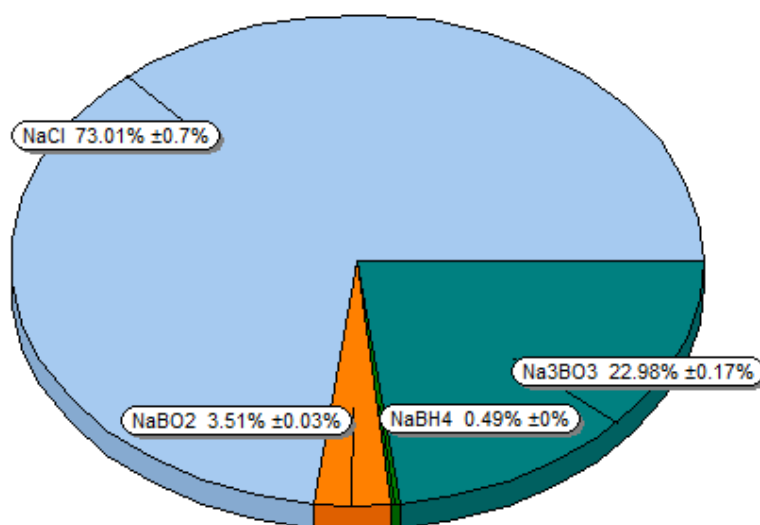


Figure 3-11. Predicted composition of the reaction products from the reaction conducted with unsupported catalyst. Results are given in wt-%.

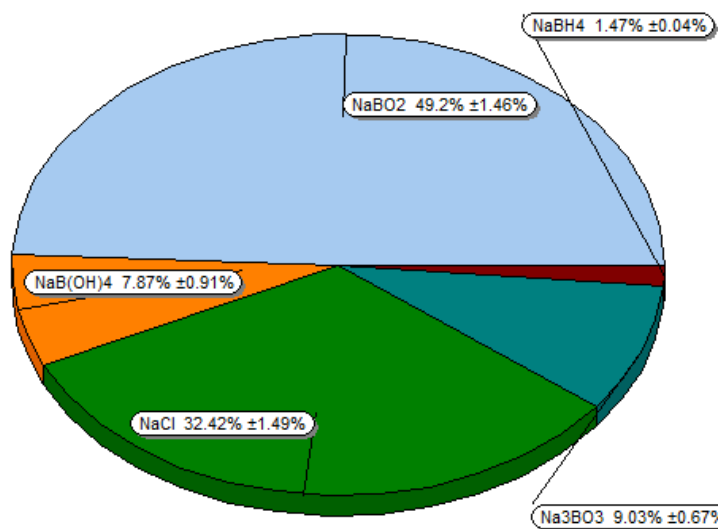


Figure 3-12. Predicted composition of the reaction products from the reaction conducted with supported catalyst. Results are given in wt-%.

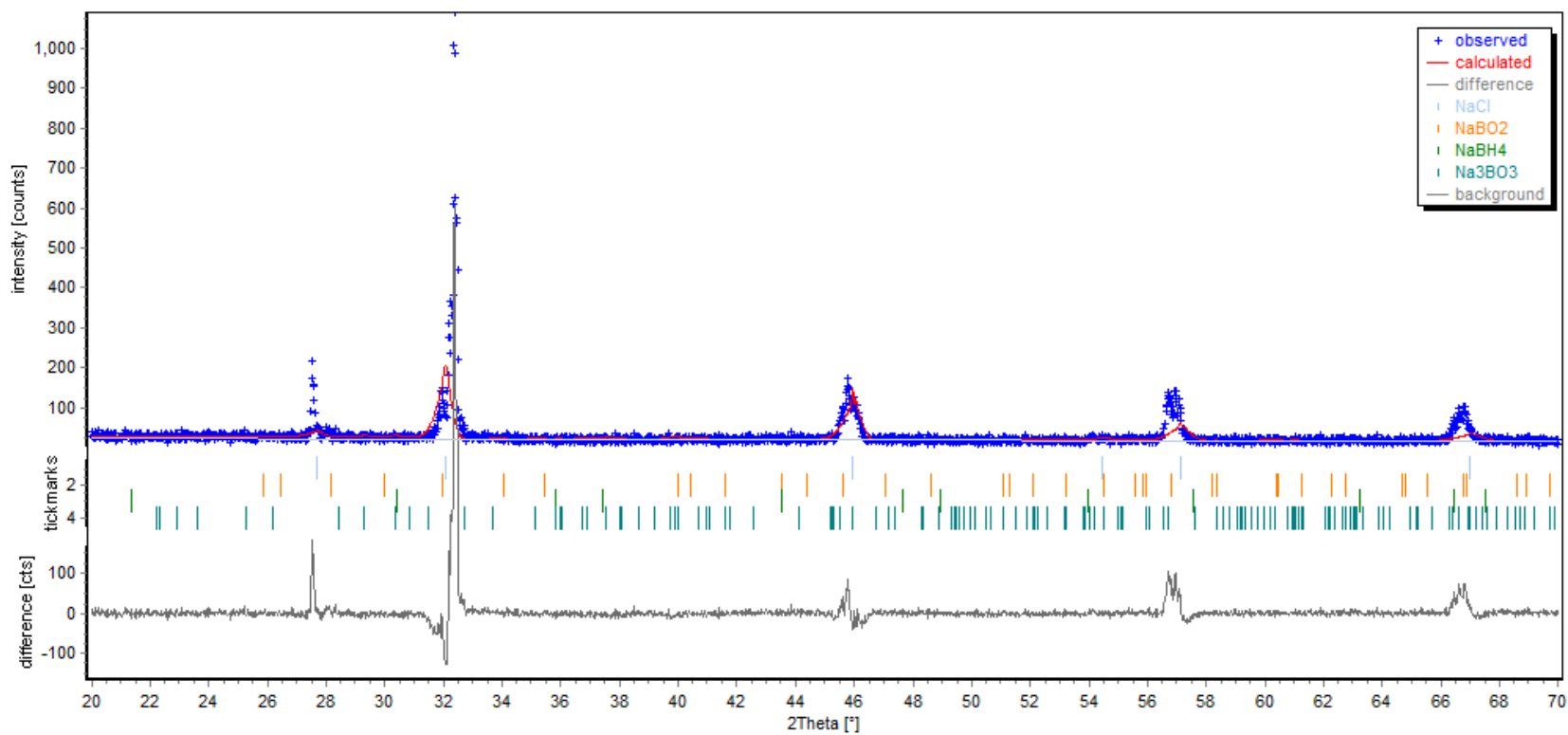


Figure 3-13. Rietveld refinement of the products of the reaction performed with unsupported catalyst.

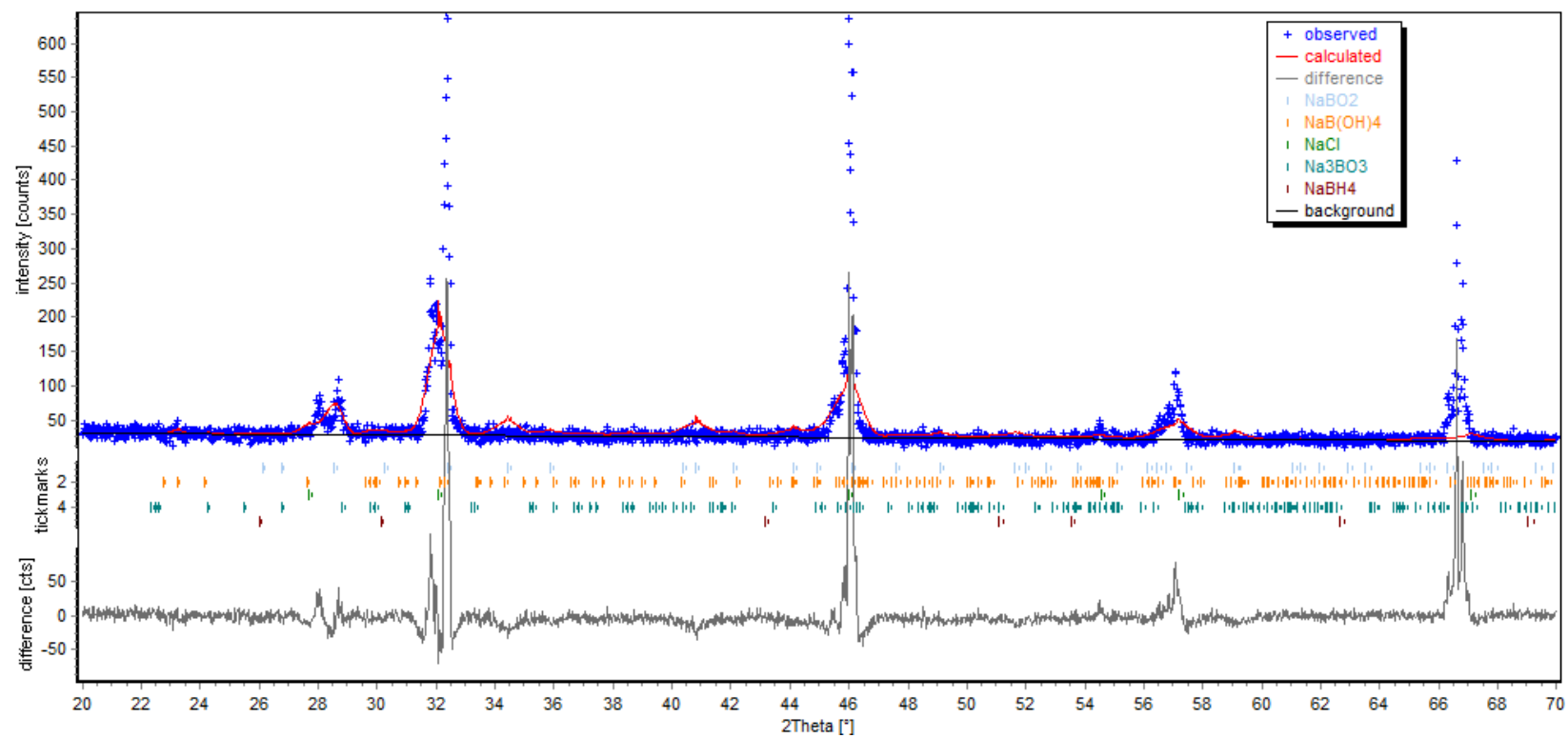


Figure 3-14. Rietveld refinement of the powders from the reaction performed with the supported catalyst.

### 3.4 Discussion of the Results

Hydrolysis of highly alkaline sodium borohydride mediated by  $\text{NiB}_x$  is fast and almost quantitative. In fact, we have obtained high yields of hydrogen evolution from aqueous solutions of sodium borohydride within 20 minutes. The calculated yields showed 95% at 303 K for unsupported promoting material and 80 % at 303 K for supported promoting material hydrogen evolution (estimated under the assumption that hydrogen behaves as an ideal gas). The non-catalyzed reaction did not show any hydrogen evolution at room temperature and only small yields at higher  $T$  (see Table 3-1). Activation energies were in the range of  $42 \pm 5$  kJ/mol for the  $\text{NiB}_x$ -mediated reaction with unsupported catalyst and  $50 \pm 10$  kJ/mol with supported catalyst. The uncatalyzed reaction showed the widest range of energies for its activation energy from 76 to 100 kJ/mol.

Although the apparent activation energies were calculated on a single – point basis, the experiment reached the goal of prove that the nickel borides which have been synthesized this way are not really catalytic, but rather promoters of hydrogen evolution.

Experimental kinetic data of the reactions of hydrolysis of sodium borohydride solutions in highly alkaline media, mediated by supported and non-supported  $\text{NiB}_2$ , showed almost 90% yield of hydrogen evolution for the unsupported powder and almost 80% yield for the supported powder, as compared to 5% from non-mediated reactions. The mediated reaction kinetics were all fast and all the hydrogen was collected within 20 minutes from the beginning of the reaction. Activation energies are strongly affected by the relatively small scale of temperatures experimentally used, however these experiments gave us a rough idea of the comparative amounts of energy for the mediated and non-mediated reactions.

In fact, it appears that NiB<sub>x</sub> promotes the reaction rather than catalyzing it: the steep drop in surface area after cycling the catalyst through subsequent reactions demonstrated that it either gets poisoned very quickly under our conditions or it actually participates in the reaction. After 1 cycle, the unsupported material was hardly evolving any hydrogen reaching a maximum yield of about 30%. The supported catalyst lasted somewhat longer, but after 3 cycles its yield of hydrogen evolution had decayed to 42%.

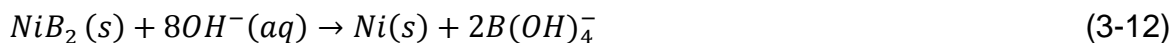
As mentioned before, the literature implies that the only product formed after the reaction is NaBO<sub>2</sub> which is not correct, and a more thorough analysis of the reaction products was missing.<sup>6,10,15-20</sup> In our experiments using XRD and IR we find proof that the both the supported and un-supported catalyst yield reaction products with somewhat different compositions.

NaBO<sub>2</sub> appears to be the main product for the reaction mediated by the supported material. In the case of the unsupported material only a poor fit to the XRD patterns was obtained when NaCl, NaBH<sub>4</sub> (which should be left-over reactant), NaBO<sub>2</sub> and Na<sub>3</sub>BO<sub>3</sub> were considered. Clearly, other possible compounds need to be considered as well and should be done in future work coupled with elemental analysis. In the reaction with the supported catalyst non-negligible quantities of NaB(OH)<sub>4</sub> were formed which are clearly absent in the refinement of the reaction products with unsupported catalyst.

One possibility for obtaining Na<sub>3</sub>BO<sub>3</sub> is through the formation of hydrated NaBO<sub>2</sub> which can further react with the excess NaOH through the following scheme:



For the formation of NaB(OH)<sub>4</sub>, it is possible that some boron from the catalyst reacted with the excess of sodium hydroxide, according to:



Where elemental boron is oxidized to B(III).

However, it has been difficult to determine a complete reaction mechanism because intermediates of reactions have not been found yet, and therefore further studies need to take into account that the nickel borides may not be catalytically active but rather promoting for hydrogen evolution from hydrolysis of alkali solutions of sodium borohydride. Next studies need to focus on the mechanisms of action of nickel borides and identification of transition states. In fact, the model which is usually studied, the bare hydrolysis of sodium borohydride, is not accurate enough to determine activation energies. Values reported by different authors, due to the variety of rate laws used fit experimental data, are difficult to compare between them and with our results.<sup>20</sup> A more complex (and more reliable) model, therefore, must make use of a well-accepted rate law to describe the kinetic of heterogeneous catalyzed sodium borohydride hydrolyses and a mechanism of action. Up to now, the reaction mechanisms and rate law proposed are based on the basic hydrolysis of sodium borohydride.<sup>20</sup>

## CHAPTER 4 CONCLUSIONS AND FUTURE WORK

### 4.1 Conclusion and Remarks

Work in this thesis shows a new synthetic pathway to boron-rich nickel borides. The nickel borides could not be completely purified which hampered the determination of an exact stoichiometry. Based on elemental analysis the material should mainly contain  $\text{NiB}_2$ . However, higher stoichiometric boron content of  $\text{B:Ni} > 2$  cannot be excluded since metallic Ni was also found in these materials. It is also not possible to exclude the possibility of a heterogeneous mixture of nickel borides of different boron-rich stoichiometries. This work presents an important contribution to a vigorous and sometimes contradictory debate in the literature about the existence of  $\text{NiB}_2$ .<sup>46,47,53-56,59-65,77</sup> Microscopy revealed characteristic ridges on the surface of the grains of the material. The spacing between these ridges was found to be 65 Å. It is known that some metal borides, such as  $\text{MgB}_2$ , show extended lattice structures, which are composed of alternated domains of boron (elemental) and magnesium (see fig 2-9); and it is quite possible that these ridges give evidence for intercalated Ni and B layers. EDXS spectra confirmed high boron content in the samples.

The surface area of the catalyst decays rather fast for both the supported and unsupported catalyst suggesting that the number of catalytic sites per unit surface area changes over time and limits the utility of  $\text{NiB}_x$  to a promoter rather than a classical catalyst of hydrogen evolution. The rapid decay of the surface area might indicate the presence of side reactions that involve different types of boron oxides and hydroxides. Identification of the reaction products was performed and it was established that apart from  $\text{NaBO}_2$  other boron oxides were formed.  $\text{Na}_3\text{BO}_3$  (23 wt-%) was observed as the

main product in the reactions using unsupported catalyst, while for the supported catalyst  $\text{NaBO}_2$  (49.2 wt-%) was the main product. Non-negligible quantities of  $\text{NaB(OH)}_4$  (7.9 wt-%) were also observed in this case but was not found in the reaction products using unsupported nickel borides.

## 4.2 Outlook

In order to get better and more meaningful data, higher milling power (ball or planetary mills) connected with a vent to a device for hydrogen collection/analysis, (such as GC/MS) is needed. This will help to determine the composition and purity of the gas phase(s).

A crucial step in any synthetic route is purification. Unfortunately, it was not possible to come up with a solution for the  $\text{NiB}_x$  material in this contribution despite many attempts. A more rigorous way of excluding the various boron oxides from the catalyst is needed. The FTIR experiments would have to be repeated with higher concentrations of the material and higher purity matrices. XPS, on our samples did not directly detect  $\text{Ni}^0$ . Next experiments may take into account Ar sputtering with consequent XPS signals detection. Ar sputtering experiments will eliminate superficial layers of material, possibly eliminating the oxides of nickel and boron, using laminar argon flow; removal of the surface layers containing amorphous boron oxides may also help to enhance or decrease the anomalous boron peak at 182 eV and allow it to be better identified. Argon sputtering experiment, may also be useful in observing elemental  $\text{Ni}^0$  signals.<sup>106</sup> Once  $\text{Ni}^0$  signals have been detected, the peak positions of the relative elements needs to be compared with literature data.

Since there is no published  $\text{NiB}_2$  crystal structure theoretical models will have to be developed to predict its structure and serve as a basis for Rietveld refinement of the

experimental XRD patterns. This is especially urgent given that the predicted stoichiometry is B:Ni = 2. If one can find structural evidence of the presence of NiB<sub>2</sub> these theoretical models may be expanded to include spectroscopic data and even explain the observed kinetics and lead to a reasonable mechanism for the reaction. In fact, the fast surface degradation of the powders implies that part of the nickel boride is reacting, most probably with NaOH.

So far, the literature assumes that the simple hydrolysis reaction of sodium borohydride is all that there is. However, this may not be sufficient to model the nickel boride-catalyzed reactions, at least in the case of our NiB<sub>x</sub>.<sup>6-8,10,78</sup> The accurate modeling of this reaction is therefore a valid future goal which will give benefits to applying this reaction in hydrogen storage and fuel cell systems in a future hydrogen economy.

## APPENDIX MAGNETIC TECHNIQUES

Solid state NMR is a powerful technique that can give structural information on solids.<sup>107</sup> It is characterized by anisotropic, direction dependent interactions inside solids. These interactions affect the magnetic resonance conditions and are observed as splittings and broadening effects of nuclear resonance under study. High resolution can be achieved using a variety of techniques, of which the most popular is magic angle spinning (MAS).<sup>107</sup> This technique averages out the anisotropic spin-spin interactions using ultrafast sample rotation. The sample is placed inside a rotor which serves as the sample holder and is allowed to spin at frequencies between 1 and 70 kHz at the magic angle of  $\theta = 54.74^\circ$  with respect to the external magnetic field.<sup>107,108</sup> This method achieves the strong reduction or even elimination of the broadening effects hampering conventional solid state NMR and helps facilitate spectral analysis and assignment of NMR peaks.

Boron is found in natural abundance of two different isotopes,  $^{11}\text{B}$  ( $I = 3/2$ ) (81.2% isotopic abundance) and  $^{10}\text{B}$  ( $I = 3$ ) (18.8%), both with a non-zero nuclear spin. Both nuclei are quadrupolar which leads to additional broadening of their solid-state NMR spectra. The  $^{11}\text{B}$  nuclei are more sensitive than  $^{10}\text{B}$  since they are more abundant and show higher magnetic moment ( $3.47\mu_N$  for  $^{11}\text{B}$  and  $2.08\mu_N$  for  $^{10}\text{B}$ ) and also show smaller quadrupole moment (40.59 millibarn for  $^{11}\text{B}$  and 84.59 millibarn for  $^{10}\text{B}$ ), therefore are the ones that are usually studied.<sup>109</sup> Solid state NMR on metal borides received particular attention between the mid 1970s to the mid 1980s. Experiments were focused on their structural characterization. The studies of Panissod et al.<sup>110,111</sup> and Kuentzler and Lemius<sup>112</sup> focused on boron signals in nickel boride glasses and  $\text{Co}_{2-x}\text{M}_x\text{B}$  crystalline materials, respectively (where M stands for several foreign metals

used as dopants). These reports also tried to justify the magnetism of these alloys monitoring experimental NMR signals of the of  $\text{Co}_{2-x}\text{M}_x\text{B}$  alloys.<sup>112</sup>

Panissod et al. used quadrupolar interactions to obtain information on the local environment of boron in various nickel borides.<sup>110,111</sup> In their work the samples were composed of several metallic nickel-boron glasses, with higher content in nickel and variable mole percent of boron.  $^{11}\text{B}$  NMR spectra constantly change with the increasing mole fraction of boron. In order to structurally determine the local environment of boron in the glasses, the spectra were simulated, optimizing the following parameters: 1) the quadrupolar frequency  $\nu_Q$  (proportional to the electric field gradient, and results from non-cubic symmetries); 2) the asymmetry parameter  $\eta$  that characterize the deviations from cylindrical geometry, and 3)  $\sigma$  the root mean square half width of a Gaussian distribution<sup>2</sup> function for amorphous samples. Figure A-1 shows the experimental spectra of the metallic glasses of nickel borides at various mole fractions of boron.

Figure A-2 shows the spectra and the corresponding simulations of the cubic structures of nickel borides.

Calculations together with some solid-state NMR experiments were performed on our  $\text{NiB}_x$  samples and compared with literature data.<sup>45,110,111</sup>

Magnetic studies were performed using solid-state NMR, EPR, and SQUID measurements.

Here we present initial preliminary results which are not complete. In the future this line of work should be continued.

---

<sup>2</sup> Experimental NMR data were not simulated. The spectra were deconvoluted using three Gaussians. The MAS technique was used in the identification of boron peaks and determination of structural data.

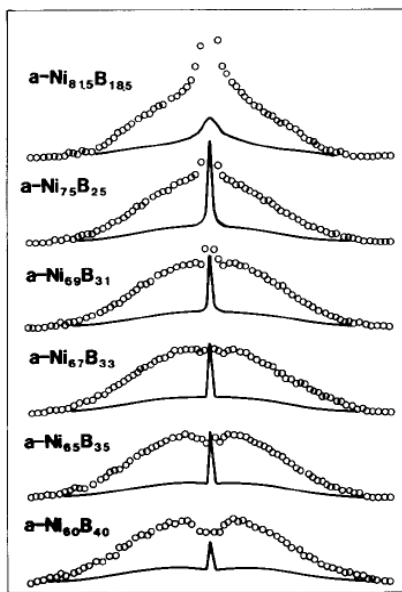


Figure A-1. Nickel boron metallic glasses, from Panissod *et al.*, 1983, *J. Magnetism and Mag. Mat.*, 31 – 34, 1523-1524. Reprinted by permission from Elsevier. Copyright Elsevier (1983).

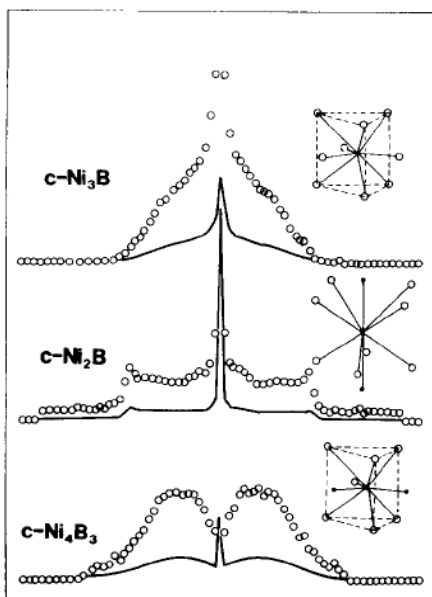


Figure A-2. Nickel boron metallic glasses with cubic symmetries NMR spectra. Reprinted by permission from Panissod, *et al.* *J. Magnetism and Mag. Mat.* 1983, 31, 1523. Copyright Elsevier (1983).

## A.1 NMR

We performed NMR on the  $^{11}\text{B}$  ( $I = 3/2$ ) nuclei in the powders in order to determine the environment of the boron nuclei and compare them with the literature and theoretical calculations using  $\text{NiB}_3$ .<sup>24,113-117</sup>

DFT calculations were performed to predict the NMR chemical shielding factors for the orthorhombic and monoclinic structures of  $\text{NiB}_3$ . This calculated isotropic shielding parameter ( $\sigma_{\text{iso}}$ ) is absolute and not related to a standard. In order to calculate the chemical shifts we therefore needed to calculate the chemical shielding constant of  $\alpha$ -phase in crystalline boron<sup>114</sup> and  $\text{NaBH}_4$ .

Values were determined for the tetragonal ( $P4_2/nmc$ ) and cubic ( $F\bar{4}3m$ ) structures of sodium borohydride. The calculated values for the boron with a hexagonal space group of  $R\bar{3}m$  were 89.52 and 91.95 ppm.

For the crystalline  $\alpha$ -phase of boron and  $\text{NaBH}_4$ , the  $\sigma_{\text{iso}}$  (B) values were 139.4 and 144.0 ppm, respectively. If we consider an average between the two calculated values of the  $\alpha$ -boron, we can obtain a calculated relative shielding constant for sodium borohydride. This average  $\delta_{\text{iso}}$  (isotropic chemical shift) for the  $\alpha$ -boron was 90.75 ppm. Therefore, the chemical shifts for the sodium borohydride structures were -48.6 and -53.3 ppm, respective to the calculated shielding. In the orthorhombic structure of  $\text{NiB}_3$ , there are two distinct sets of borons whose calculated isotropic shielding were 135.09 and 171.19 ppm, respectively, for the outermost and the inner chain. Figure A-3 shows the calculated isotropic shielding for the orthorhombic structure.

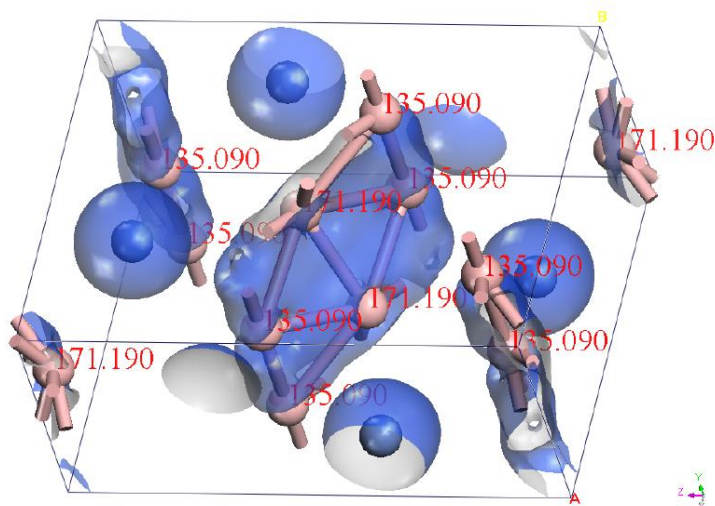


Figure A-3. Calculated isotropic shielding for the orthorhombic structure of  $\text{NiB}_3$ . These values, when referred to the calculated  $\alpha$ - boron presented chemical shifts of -44.4 and -80.4 ppm, respectively for the 135.090 and 171.190 ppm.

The optimized lowest energy structure for  $\text{NiB}_3$  was triclinic (see Paragraph 2.2). Since two of the angles differed from  $90^\circ$  only by fractions of a degree we used a monoclinic  $P_21/c$  system which was easier to calculate. This fixes these angles at exactly  $90.00^\circ$ .

Three different boron atoms can be distinguished in the latter structure by their symmetry. The inner boron atoms have a shielding constant of 77.25 ppm, while the lateral boron chains are more exposed to the magnetic field, and showed a shielding constant of 50.85 ppm and 18.43 ppm, respective to the calculated average shielding for boron atoms. Therefore, the chemical shifts are 13.49, 50.85, and 72.31 ppm. Figure A-4 shows the structure for the latter calculated NMR parameters.

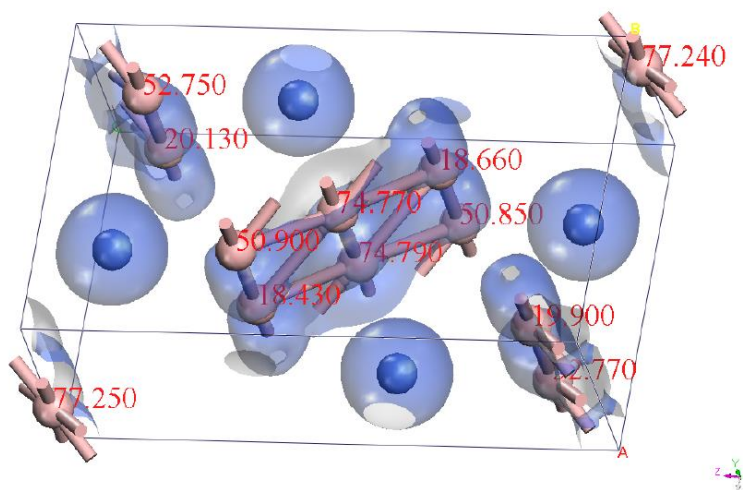


Figure A-4. Calculated isotropic shielding constants of the monoclinic structure of  $\text{NiB}_3$ .

Experimentally, we have obtained NMR and MAS spectra\* using a Bruker Advance 400 MHz spectrometer with a wide bore 9.4 T magnet (courtesy of Prof. Barò, UAB, Spain). The NMR showed a split signal that can be decomposed into three or more peaks. Figure A-5 shows the experimental NMR in which the lines have been fitted using three Gaussian functions.

Results show two peaks at 5.3 and -10.2 ppm and a broad one, centered at 0.3 ppm. This has to be compared with literature data: Portehault *et al.*<sup>45</sup> reports NMR spectra for  $\text{NbB}_2$ , amorphous boron, and  $\text{LiBO}_2$ . His findings are reproduced in Figure A-6.

Both the literature spectrum, as well as our own, shows a broad peak in addition to several narrow ones overlapping it.

---

\*Experiments were carried out at the Universidad Autonoma de Barcelona (Bella Terra, Spain) in collaboration with Dr. Sebastiano Garroni, former alumnus of professor M. A. Barò, and an international expert in  $^{11}\text{B}$  NMR

The broad signal was identified as B-B bonds since analogous broad signal was seen in amorphous boron.<sup>45</sup>

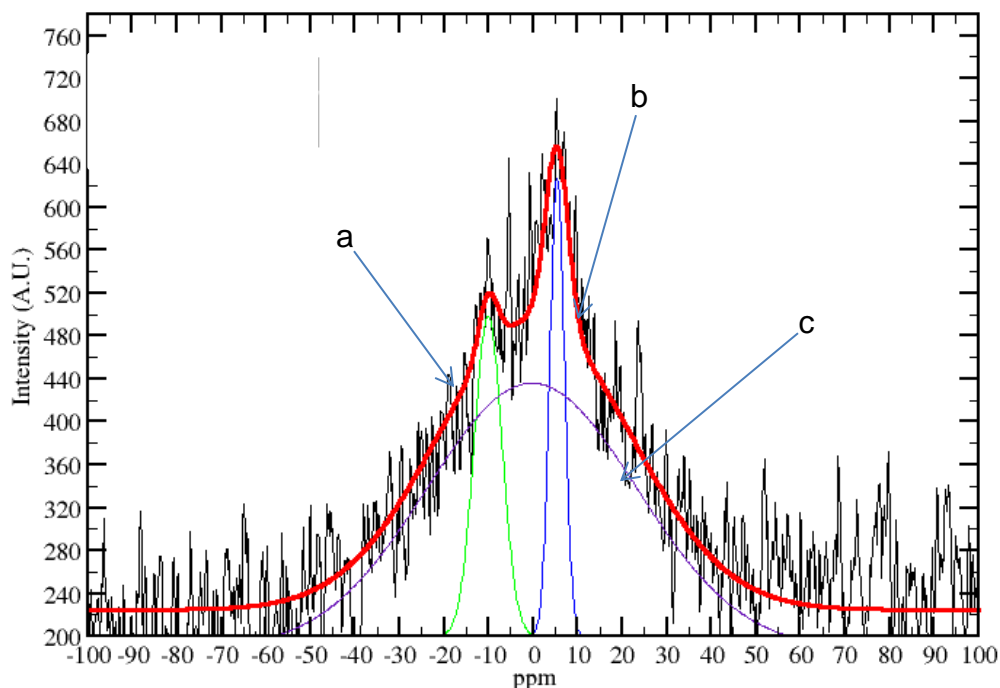


Figure A-5. Experimental NMR spectrum of hydrolyzed (room temperature)  $\text{NiB}_x$  (black) and simulation (red). The individual lines deriving from the deconvoluted fitting line are reported as well: a) line centered at -10.2 ppm; b) line centered at 5.3 ppm and c) line centered at -0.3 ppm.

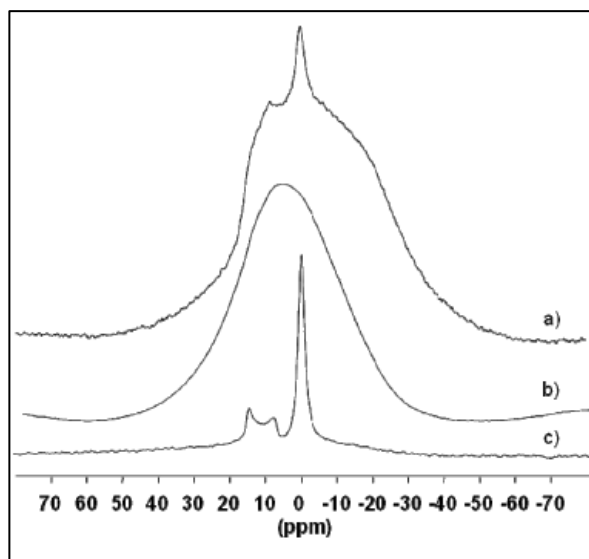


Figure A-6.  $^{11}\text{B}$  NMR spectra reprinted by permission from Portehault *et al.*:<sup>45</sup> a)  $\text{NbB}_2$ , b) amorphous boron, and c)  $\text{LiBO}_2$ .

However, it is difficult to arrive at a consistent structural hypothesis based on the NMR results alone. To further understand the boron signals in our samples, MAS-NMR experiments were performed.

The MAS spectra were acquired using a boron-free Bruker 4mm CPMAS probe (see footnote pag.148). The frequency used to tune the probe based on the Larmor frequency of boron was 128.33 MHz. The spectra were collected using the non-hydrolyzed powders and used a  $\text{BF}_3\text{-Au}$  complex as the standard.

The powders were packed in  $\text{ZrO}_2$  rotors in an Ar- filled glovebox and sealed with tight fitting Kel-F caps. Sample spinning was done using dry nitrogen gas. MAS spectra were collected at room temperature using rotation frequencies of 12 kHz, and the 1-D MAS spectra were acquired using a  $2.7 \mu\text{s}$  single  $\pi/2$  pulse (corresponding to a RF pulse of 92.6 kHz). The acquisition of the spectra was performed applying a strong proton decoupling sequence by using the two-pulse phase modulation (TPPM) scheme.

This sequence consists of a windowless train of two pulses of length  $\tau_p$  with opposite alternating phases ( $+\phi$  and  $-\phi$ ).<sup>118</sup>

Figure A-7 shows the pulse sequence for a general TPPM.

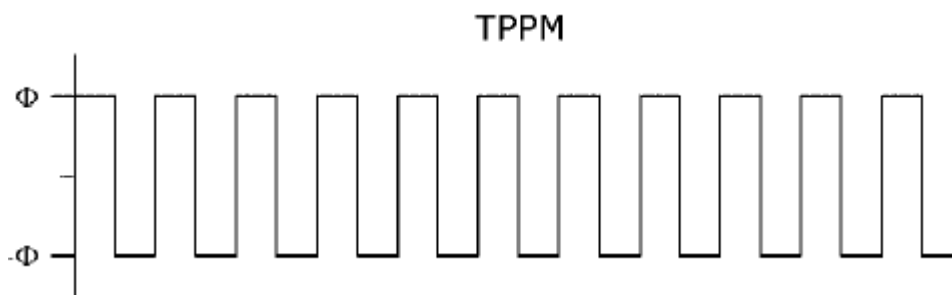


Figure A-7. The TPPM pulse sequence. Reprinted by permission from Vinod Chandran, C.; Madhu, P. K.; Kurur, N. C.; Brauniger, T. *Magn. Reson. Chem.* **2008**, *46*, 943. Copyright (2008) Elsevier

Recovery was set at 10 seconds. The spectra were acquired at 20°C.

The temperature was measured with a Bruker BCU temperature control unit.

Figure A-8 shows the  $^{11}\text{B}$   $^1\text{H}$  ( $I = 3/2$ ) NMR-MAS spectrum.

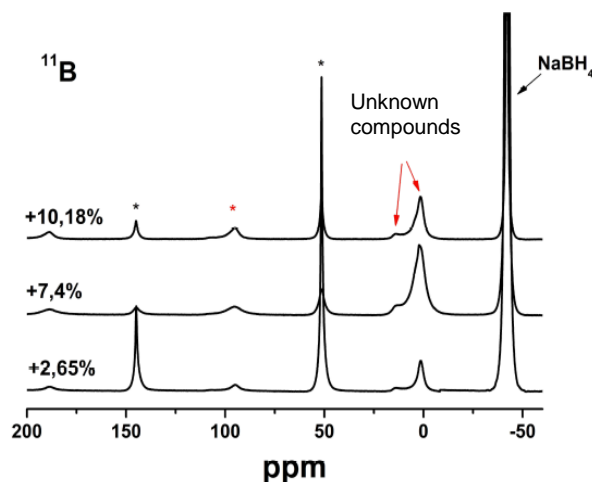


Figure A-8. NMR MAS spectrum of the non-hydrolyzed powders. The signals around zero ppm belong to unidentified compounds. The side bands at 100 and 200 ppm are attributed to the main  $\text{NaBH}_4$  peaks.

The sharp line at negative ppm values (-42.04 ppm), in Figure A-8, was attributed to boron in tetrahedral  $[\text{BH}_4^-]$  units in  $\text{NaBH}_4$  and show MAS satellites at about 50 and 150 and 190 ppm.<sup>24</sup> Two additional weaker and broader peaks were observed at +1.6 and +13.6 ppm. They could not be readily identified with a known compound and were labeled as “unknown compound.” Given the analysis in the preceding chapters they probably belong to either boron oxides and/or the  $\text{NiB}_x$ . Since we determined nickel boride stoichiometry as close to  $\text{NiB}_2$ , it is reasonable to exclude the  $\text{NiB}_3$  monoclinic phase from consideration. Calculations of a theoretical spectrum for  $\text{NiB}_2$  are under way and will be compared to the experimental spectra.

## A.2 EPR

EPR measurements were also performed on the powders. Temperature dependent spectra were collected using an X-band Bruker Elexsys E580 spectrometer,

using the instrumental following parameters: magnetic field range of  $7550 \pm 7500$  G, 4096 data points per spectrum, 20 dB power attenuation, 60 dB receiver gain, 20.48 ms time constant, and 81.92 ms sampling time. Spectra were acquired at temperatures from 5 K to room temperature (291 K). The results are summarized in Figure A-9.

The signals collected covered almost 7000 G (nearly half of the full width of the magnetic field intensity range of this instrument). Such broad signals are often a signature of ferromagnetic compounds. In this case they are probably due to the formation of nickel nanoparticles inside the powders which was also confirmed by XRD where reflections due to metallic Ni were observed. The line positions in the spectra are somewhat temperature dependent and the linewidths decrease with increasing temperatures. The broadest spectrum, taken at the lowest temperature, feels the initial application of the magnetic field, which aligns the spin domains in the ferromagnetic sample. However, after the first spectrum, the spin remains aligned, and therefore, subsequent spectra look very different from the first one because of the different orientation of the sample spin domains. Lefondeur et al.<sup>119</sup> demonstrated that the electronic  $g$ -factor and the EPR peak-to-peak linewidth in nickel nanoparticles is dependent on temperature, since the spin-spin and the spin-lattice relaxation times depend strongly from the temperature, according to the Curie- Weiss law, which describes the magnetic susceptibility in function of a ferromagnet under the application of an external magnetic field, above a certain critical temperature, called Curie temperature. The equation used to describe this behavior is the following:

$$\chi = \frac{C}{T - T_C} \quad \text{A-1}$$

Where  $C$  is a specific Curie constant which depends from the material studied and  $T_C$  is the Curie temperature expressed in K as the temperature.<sup>120</sup>

Nickel-rich nickel borides usually show diamagnetic or slightly paramagnetic properties.<sup>63,101,110,111</sup>

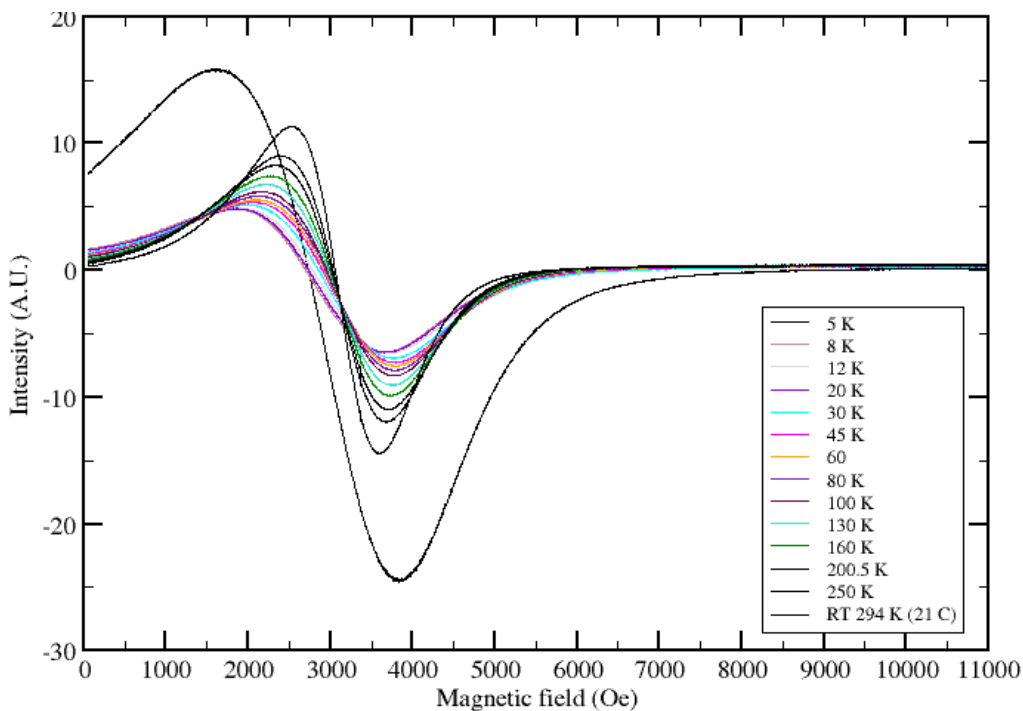


Figure A-9. Temperature dependent EPR spectra of the non-hydrolyzed powders.

### A.3 SQUID

In order to confirm the ferromagnetic behavior of the nickel borides, SQUID measurement were performed. Hysteresis curves were collected between 1.8 and 10 K. Figs A-10 summarizes the results from the SQUID measurements. Experimental data are then compared with the work from Legrand *et al.*,<sup>101</sup> whose data are presented in Figure A-11.

As can be seen in Figure A-10, the samples show only little ferromagnetic hysteresis and the maximum is reached at 1.8 K (lowest instrumental temperature) and almost disappears at 10 K. This result confirms the ferromagnetic nature at low

temperature and also suggests that the sample contains ferromagnetic particles, i.e., is not completely ferromagnetic.

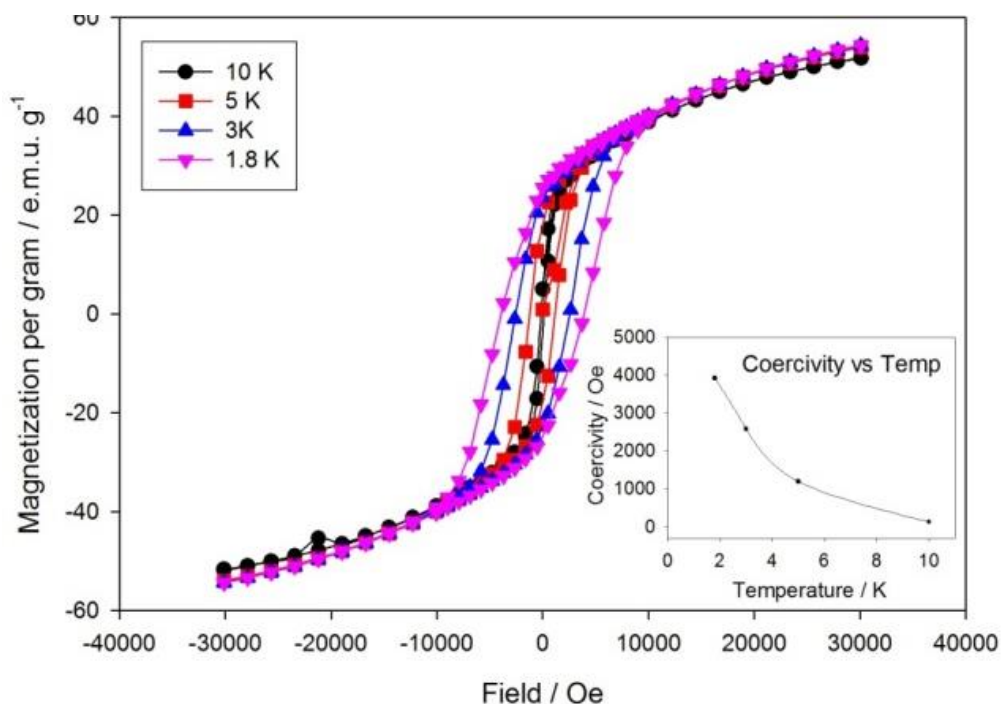


Figure A-10. Hysteresis cycles at temperatures between 1.8 and 10 K. The inset shows the coercivity curve.

In order to clarify if nickel nanoparticles are responsible for this behavior we compared our results with the work of Legrand et al.<sup>101</sup> There, nickel boride Ni<sub>3</sub>B nanoparticles had been synthesized and were characterized by XPS and magnetic measurements. SQUID measurements on samples stored in air showed a hysteresis at nearly 3 K. It disappeared when the nanoparticles were stored under nitrogen. According to Legrand et al.<sup>101</sup> this hysteretic behavior was attributed to the formation of Ni<sup>0</sup> clusters when the nanoparticles were stored under normal atmospheric conditions. Similarly, nickel nanoclusters may have formed in our samples because the samples were handled and stored/aged in air. Figure A-11 shows the hysteresis of the nickel nanoparticles observed by Legrand et al.<sup>101</sup>

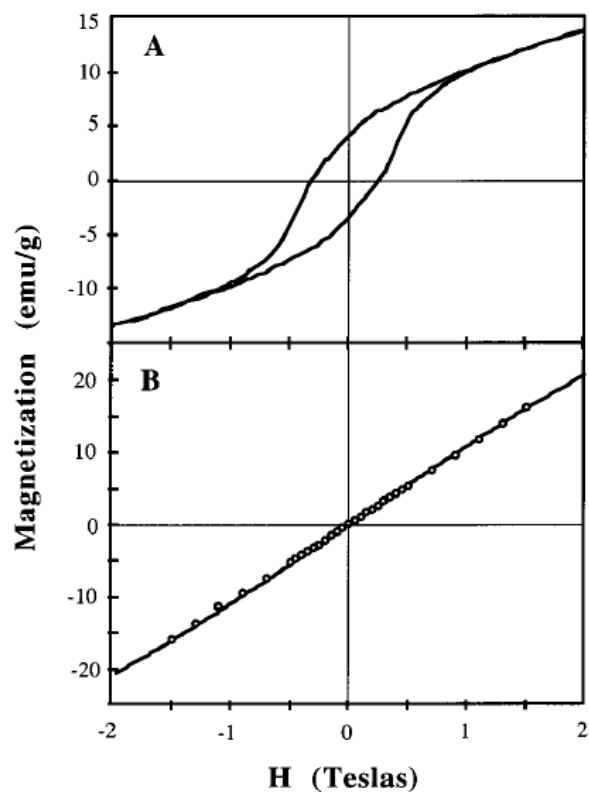


Figure A-11. Hysteresis of nanoparticles stored in open air (A) and under nitrogen (B). Reprinted by permission from Legrand, J.; Taleb, A.; Gota, S.; Guittet, M.-J.; Petit, C. *Langmuir* **2002**, *18*, 4131. Copyright (2002) American Chemical Society.

## LIST OF REFERENCES

- (1) Grochala, W.; Edwards, P. *Chem. Rev.* **2004**, *104*, 1283
- (2) D.O.E., Ed. [www.hydrogen.energy.gov](http://www.hydrogen.energy.gov), 2006.
- (3) U.S. Department of Energy - Energy Efficiency and Renewable Energy: [http://www1.eere.energy.gov/hydrogenandfuelcells/storage/hydrogen\\_storage.htm](http://www1.eere.energy.gov/hydrogenandfuelcells/storage/hydrogen_storage.htm), 2012.
- (4) Gosalawit-Utke, R.; Bellosta von Colbe, J. M.; Dornheim, M.; Jense, T. R.; Cerenius, Y.; C., B. M.; Peschke, M.; Bormann, R. *J. Phys. Chem. C* **2010**, *114*, 10921.
- (5) Bogdanovic, B.; Schwickardi, M. *J. Alloys and Compounds* **1997**, *253-254*, 1.
- (6) Hua, D.; Hanxi, Y.; Xinping, A.; Cha, C. *Intl J. of Hydrogen Energy* **2003**, *28*, 1095.
- (7) Liu, B. H.; Li, Z. P.; Suda, S. *J. All. Cpds.* **2006**, *415*, 288
- (8) Liu, B. H.; Li, Z. P. *J. Power Sources* **2009**, *187*, 527
- (9) Acosta, D.; Ramirez, N.; Erdmann, E.; Destefanis, H.; Gonzo, E. *Catalysis Today* **2008**, *133*, 49
- (10) Hung, A. J.; Tsai, S. F.; Hsu, Y. Y.; Ku, J. R.; Chen, Y. H.; Yu, C. C. *Intl J. of Hydrogen Energy* **2008**, *33*, 6205
- (11) Pistidda, C.; Garroni, S.; Bonatto Minella, C.; Dolci, F.; Jensen, T. R.; Nolis, P.; Bosenberg, U.; Cerenius, Y.; Lohstroh, W.; Fichtner, M.; Baro, M. D. *J. Phys. C: Solid State Phys.* **2010**, *114*, 21816
- (12) Pistidda, C.; Garroni, S.; Dolci, F.; Bardaji, E. G.; Khandelwal, A.; Nolis, P.; Dornheim, M.; Gosalawit, R.; Jensen, T.; Cerenius, Y.; Surinach, S.; Baro, M. D.; Lohstroh, W.; Fichtner, M. *J. All. Cpds.* **2010**, *508*, 212
- (13) Stock, A. *Hydrides of boron and silicon*; Cornell University Press: Ithaca, N.Y., 1933.
- (14) Schlesinger, H. I.; Brown, H. C.; Finholt, A. E.; Gilbreath, J. R.; Hoekstra, H. R.; Hyde, E. K. *J. Am. Chem. Soc.* **1953**, *75*, 215
- (15) Churikov, A. V.; Gamayunova I.M.; Zapsis, K. V.; Churikov, M. A.; Ivanischev, A. V. *Intl. J. Hydrogen Energy* **2012**, *37*, 335.

- (16) Sahin, O.; Dolas, H.; Kaya, M.; Sait Izgi, M.; Demir, H. *Intl. J. Energy Res.* **2010**, *34*, 557.
- (17) L., Y.; Matthews, M. A. *Intl. J. Hydrogen Energy* **2011**, *36*, 7416.
- (18) Demirci, U. B.; Akdim, O.; Andrieux, J.; Chamoun, R.; Miele, P. *Fuel Cells* **2010**, *3*, 335.
- (19) Akdim, O.; Demirci, U.; Muller, D.; Miele, P. *Intl. Journal of Hydrogen Energy* **2009**, *34*, 2631.
- (20) Retnamma, R.; Novais, A. Q.; Rangel, C. M. *Intl. J. Hydrogen Energy* **2011**, *36*, 9772.
- (21) Varin, R. A.; Czujko, T.; Wronski, Z. S. *Nanomaterials for Solid State Hydrogen Storage*; Springer, 2008.
- (22) Schlesinger, H. C.; Brown, H. R. *J. Am. Chem. Soc.* **1940**, *62*, 3429
- (23) Goerrig, D. In *Verfahren zur Herstellung von Boranaten* Germany, 1958; Vol. GE 1 077644.
- (24) Garroni, S.; Milanese, C.; Pottmaier, D.; Mulas, G.; Nolis, P.; Girella, A.; Caputo, R.; Olid, D.; Teixdor, F.; Baricco, M.; Marini, A.; Surinach, S.; Baro, M. D. *J. Phys. C: Solid State Phys.* **2011**, *115*, 16664.
- (25) Hwang, S.-J.; Bowman, R. C.; Reiter, J. W.; Rijssenbeek; Soloveichik, G. L.; Zhao, J.-C.; Kabbour, H.; Ahn, C. C. *J. Phys. C: Solid State Phys.* **2009**, *112*, 3164.
- (26) Wu, C.; Wu, F.; Bai, Y.; Yi, B.; Zhang, H. *Mater. Lett.* **2005**, *59*, 1748.
- (27) Davis, R. E.; Bromels, E.; Kibby, C. L. *JACS* **1962**, *84*, 885.
- (28) Davis, R. E.; Kibby, C. L.; Swain, C. G. *JACS communication to the editor* **1960**, *82*, 5950.
- (29) Yu L.; Matthews, M. A. *Intl. J. Hydrogen Energy* **2011**, *36*, 7416.
- (30) Fan, W.; Li, W.; Ma, X.; Tao, X.; Li, X.; Yao, Y.; Xie, X.; Zhang, Z. *J. Org. Chem.* **2011**, *76*, 9444
- (31) Kasparian, A. J.; Savarin, C.; Allegeier, A. M.; Walker, S. D. *J. Org. Chem.* **2011**, *2011*, 9841
- (32) Acosta, D.; Martinez, J.; Carrera, C.; Erdmann, E.; E., G.; Destefanis, H. *L.A.A.R.* **2006**, *36*, 317.

- (33) Brown, C. A. *J. Org. Chem.* **1970**, 35, 1900.
- (34) Buisson, P.; Paul, R.; Joseph, N. *Ind. & Eng. Chem.* **1952**, 44, 1006
- (35) Collins, D. J.; Smith, A. D.; Davis, B. H. *Ind. Eng. Chem. Prod. Dev.* **1982**, 21, 279
- (36) Ganem, B.; Osby, J. O. *Chem. Rev.* **1986**, 86, 763
- (37) Liaw, B. J.; Chiang, S. J.; Tsai, C. H.; Chen, Y. Z. *Appl. Catal. A: Gen.* **2005**, 284, 239
- (38) Skrabalak, S. E.; Suslick, K. S. *Chem. Mater.* **2006**, 18, 3103.
- (39) Wang, M.; Li, H.; Wu, Y.; Zhang, J. *Mat. Lett.* **2003**, 57, 2954
- (40) Wang, M.; Li, H.; Wu, Y.; Zhang, J. *J. Catalysis* **2003**, 214, 15
- (41) Wong, S. T.; Lee, J. F.; Chen, J. M.; Mou, C. Y. *J. Mol. Cat. A.: Chemical* **2001**, 165, 159
- (42) Jeon, E.; Cho, Y. W. *J. All. Cpds.* **2006**, 422, 273.
- (43) Srnivasan, S.; Escobar, D.; Goswami, Y. Y.; Stefanakos, E. *Intl J. of Hydrogen Energy* **2008**, 33, 2268
- (44) Srnivasan, S.; Escobar, D.; Jurczyk, M.; Goswami, Y. Y.; Stefanakos, E. *J. All. Cpds.* **2008**, 462, 294.
- (45) Portehault, D.; Devi, S.; Beaunier, P.; Gervais, C.; Giordano, C.; Sanchez, C.; Antonietti, M. *Angew. Chem. Intl. Ed.* **2011**, 50, 3262
- (46) Howe, J. L. *Inorganic Chemistry Review* **1908**, 618
- (47) Howe, J. L. *Inorganic Chemistry Review* **1909**, 1284
- (48) Finch, C. B.; Cavin, O. B.; Becker, P. F. *J. Cryst. Growth* **1984**, 67, 556
- (49) Kapfemberger, C.; Hofmann, K.; Albert, B. *Solid St. Sci* **2003**, 5, 925
- (50) Okamoto, Y.; Nitta, Y.; Imanaka, T. *Faraday Trans. 1* **1979**, 75, 2027
- (51) Rundqvist, S. *Acta Chemica Scandinavica* **1959**, 13, 1193
- (52) Rundqvist, S.; Pramatus, S. *Acta Chemica Scandinavica* **1967**, 21, 191

- (53) Sobolev, A. S.; Fedorov, T. F. *Inorg. Mat.* **1967**, 3, 643.
- (54) Sobolev, A. S.; Fedorov, T. F. *Inorg. Mater.* **1967**, 3, 723.
- (55) Portnoi, K. I. *Transl. from Dokl. Akad. Nauk SSSR* **1966**, 169, 1104
- (56) Portnoi, K. I.; Romashov, V. M.; Chubarov, V. M.; Levinskaya, M. K.; Salibekov, S. E. *Transl. from Poroshkovaya Metallurgiya* **1966**, 2, 15
- (57) Decker, B. F.; S., K. J. *Acta Cryst.* **1960**, 13.
- (58) Rakovich E.; Sviridov, V.; Gaevskaya, T. *Inorg. Mater.* **2000**, 576
- (59) Ajao, J. *J. Mat. Sci.* **1988**, 23, 1112.
- (60) Battezzati, L.; Antonione, C.; Baricco, M. *J. All. Cpds.* **1997**, 247, 164.
- (61) Kaufman, L. *J. Thermochem.* **1984**, 8, 25
- (62) Kolomytsev, P. T. *Izv. Akad. Nauk. SSSR, Otd. Tekh. Nauk. Metall. Topl.* **1960**, 83
- (63) Kostetskiy, I. I.; L'vov, S. N. *Fiz. Metal. Metalloved. (English translation)* **1972**, 33, 773
- (64) Romashov, V. M.; Timofeeva, N. I.; Frolova, K. I.; Romanovich, I. V. *Poroshkovaya Metallurgiya (Eng. Transl.)* **1970**, 9, 80
- (65) Smirnyagina, N. N.; Sizov, I. G.; Semenov, A. P. *Inorg. Mater.* **2002**, 38, 39
- (66) Andersson, L. H.; Kiessling, R. *Acta Chemica Scandinavica* **1950**, 4, 160
- (67) Kiessling, R. *Acta Chemica Scandinavica* **1950**, 4, 209
- (68) Corrias, A.; Ennas, G.; Marongiu, G.; Musinu, A.; Paschina, G.; Zedda, D. *Mat. Sci. and Eng.:A* **1995**, 204, 211
- (69) Nazarian - Samani, M.; Reza Kamali, A.; Mobarra, R.; Nazarian - Samani, M. *Mat. Lett.* **2010**, 64, 309
- (70) Kolmogorov, A.; Curtarolo, S. *Phys. Rev. B.* **2006**, 74, 1.
- (71) Lassoued, S.; Gautier, R.; Boutarfaia, A.; Halet, J. F. *Organomet. Chem* **2010**, 695, 987

- (72) Mansour, A. *Phys. Rev. B.* **1997**, 55.
- (73) Mohn, P.; Pettifor, D. G. *J. Phys. C: Solid State Phys.* **1988**, 21, 2829
- (74) Witusiewicz, V. T. *Thermochimica Acta* **1995**, 264, 41
- 267 (75) Molvinger, K.; Lopez, M.; Court, J. *J. Mol. Cat. A.: Chemical* **1999**, 150,
- 2263 (76) Molvinger, K.; Lopez, M.; Court, J. *Tetrahedron: Asymmetry* **2000**, 11,
- (77) Molvinger, K.; Lopez, M.; Court, J.; Chavant, P. Y. *Appl. Catal. A: Gen.* **2001**, 231, 91
- (78) Chen, Y. Z.; Chen, Y. C. *Appl. Catal. A: Gen.* **1994**, 115, 45
- (79) Pinto, A. M. F. R.; Falcao, D. S.; Silva, R. A.; Rangel, C. M. *Intl. J. Hydrogen Energy* **2006**, 31, 1341.
- (80) Schreifels, J. A.; Maybury, P. C.; Swartz, W. E. *J. Catalysis* **1980**, 65, 195.
- (81) Caputo, R.; Guzzetta, F.; Angerhofer, A. *J. Inorg. Chem.* **2010**, 49, 8756
- (82) Bradley, A.; Taylor, A. *Phylos. Mag.* **1937**, serie 7, 1049
- (83) Saniz, R.; Ye, L. H.; Shihidou, T.; Freeman, A. *Phys. Rev. B.* **2006**, 74.
- (84) Sato, S.; Kleppa, O. *Metall. Trans. B.* **1982**, 13B, 251.
- (85) Roman, P.; Gutierrez-Zorrilla, J. M. *J. Chem. Ed.*, **1985**, 62, 167.
- (86) Klančnik, G.; Medved, J.; Mrvar, P. *J. Materials and Geoenvironment* **2010**, 57, 127.
- (87) Badeshia, H. K. D. H. In *University of Cambridge, Material Science and Metallurgy*.
- (88) Andes Hess, B., Jr.; Schaad, L.; Carsky, P.; Zahradnik, R. *Chem. Rev.* **1986**, 86, 709.
- (89) Harvey, K. B.; McQuacker, N. R. *Can. J. Chem.* **1971**, 49, 3272.
- (90) Filinchuk, Y.; Hagemann, H. *European J. Inorg. Chem.* **2008**, 3127.

- (91) Sundar, C. S.; Bharathi, A.; Premila, M.; Sairam, T. N.; Kalavathi, S.; Reddy, G. L. N.; Sastry, V. S.; Hariharan, Y.; Radhakrishnan, T. S.; Material Science Division, Indira Gandhi Centre for Atomic Research: Kalpakkam, India, 2001, p 1.
- (92) Akimitsu, J. In *Symposium on Transition Metal Oxide* 2001.
- (93) Nagamatsu, J.; Nakagawa, N.; Muranaka, T.; Zenitani, Y. 2001.
- (94) Goriletsky, V. I.; Mitichkin, A. I.; Belenko, L. E.; Rebrova, T. P. *Semiconductors, Physics, Quantum electronics and Optoelectronics* **2001**, 4, 139.
- (95) West, A. *Solid State Chemistry*; John Wiley and Sons: Norwich, 1984.
- (96) Rietveld, H. M. *J. Appl. Cryst.* **1969**, 2, 65.
- (97) Birkenstock, J.; Fischer, R.; Messner, T. *Ber. DMG, Beih. z. Eur J. Mineral.* **2003**, 15.
- (98) McCusker, L. B.; Von Dreele, R. B.; Cox, D. E.; Louer, D.; Scardi, P. *J. Appl. Cryst.* **1999**, 32, 36
- (99) Blum, P. *J. Phys. Radium* **1952**, 13, 430.
- (100) Hill, R. J.; Howard, C. J. *J. Appl. Cryst.* **1987**, 20, 464.
- (101) Legrand, J.; Taleb, A.; Gota, S.; Guittet, M.-J.; Petit, C. *Langmuir* **2002**, 18, 4131
- (102) Birajdar, B.; Peranio, N.; Eibl, O. *Microsc. Microan.* **2007**, 13, 290
- (103) Vendrine, J. C.; Hollinger, G.; Duc, T. M. *J. Phys. Chem.* **1978**, 82, 1515.
- (104) Brunhauer, S.; Emmett, P. H.; Teller, E. *J. Am. Chem. Soc.* **1938**, 60, 309.
- (105) Houston, P. L. In *Chemical Kinetics and Reaction Dynamics*; McGraw-Hill: New York, 2001, p 181.
- (106) Barr, T. L. *J. Phys. Chem.* **1978**, 82, 1801.
- (107) Schurko, R. [http://mutuslab.cs.uwindsor.ca/schurko/ssnmr\\_schurko.pdf](http://mutuslab.cs.uwindsor.ca/schurko/ssnmr_schurko.pdf), 2009.
- (108) Hennel, J.; Klinowski, J. *Topics in Current Chemistry* **2005**, 246, 1.
- (109) Hoffman, R.; Ozery, Y. <http://chem.ch.huji.ac.il/nmr/techniques/1d/row2/b.html>, 2011-02-24; Vol. 2012.

- (110) Panissod, P. *Journal De Physique (Eng. Trans.)* **1985**, C8, 241
- (111) Panissod, P.; Bakonyi, I.; Hasegawa, R. *J. Magnetism and Mag. Mat.* **1983**, 31, 1523
- (112) Lemius, B.; Kuentzler, R. *Solid St. Comm.* **1975**, 16, 639
- (113) Caputo, R.; Tekin, A. *J. Solid St. Chem.* **2011**, 185, 1622
- (114) Caputo, R.; Zuttel, A. *Mol. Phys.* **2009**, 107, 1831
- (115) Lundstroem, T.; Tergenius, L.; Higashi, I. *Z. Kristallogr.* **1984**, 167, 235.
- (116) Pickard, C.; Mauri, F. *Phys. Rev. B.* **2001**, 63.
- (117) Yates, J.; Pickard, C.; Mauri, F. *Phys. Rev. B.* **2007**, 76.
- (118) Vinod Chandran, C.; Madhu, P. K.; Kurur, N. C.; Brauniger, T. *Magn. Reson. Chem.* **2008**, 46, 943.
- (119) Lefondeur, S.; Monteverdi, S.; Molina, S.; Bettahar, M. M.; Fort, Y.; Zhilinskaya, E. A.; Aboukais, A.; Lelaurain, M. *J. Mat. Sci* **2001**, 36.
- (120) Dec, J.; Kleeman, W. *Solid St. Comm.* **1998**, 106, 695.

## BIOGRAPHICAL SKETCH

The author, FG, was born in Palermo, Italy. He enrolled in the Department of Chemistry at the Università degli Studi di Palermo in 1998 and graduated with a B.Sc. in Inorganic Chemistry in 2005. In 2006 he moved to Gainesville to complete his Master of Science work in the Department of Chemistry at the University of Florida, under the supervision of Dr. Alexander Angerhofer.